NEUROTRANSMITTER PROFILING WITH HIGH AND ULTRA-HIGH FIELD

MAGNETIC RESONANCE SPECTROSCOPY:

OPTIMIZATION FOR CLINICAL AND TRANSLATIONAL STUDIES IN

SCHIZOPHRENIA.

Antonio Napolitano

Thesis submitted to the University of Nottingham

for the degree of Doctor of Philosophy

December 2010

Contents

Summary

Growing interest in the research community has been shown in clinical neuroscience to assess neurotransmitter profiling both in healthy and diseased subjects. A large body of research in this field focuses on schizophrenia to characterise its glutamatergic level according to the most recent hypothesis of NMDA (N-Methyl-D-aspartic acid) receptors hypofunction.

Magnetic Resonance Spectroscopy (MRS) is able to detect some of the most common neurotransmitters but a number of issues, such as low signal to noise ratio (SNR), spectra overlapping and line broadening prevents MRS from being clinically relevant for neuropsychiatry.

Four important aims were considered relevant for this work.

Firstly, we aimed to compare the reliability of conventional and timing-optimized sequences for the detection and measurement of most of the visible metabolites and, in particular, for glutamate (Glu), glutamine (Gln) and gamma-aminobutyric acid (GABA) to assess the best available sequence for a study in schizophrenia.

Secondly, we also intended to investigate whether glutamatergic activity might predict the oscillatory activity and how this link might survive or not in schizophrenia.

Thirdly, we wanted to study whether the well known animal model of schizophrenia, the rearing in isolation model, exacerbates the effect of ketamine and determines more profound changes on neurotransmitter profile in rats.

Fourthly, a further goal focuses on the improved data acquisition and on the data processing to reliably resolve GABA and to be able to quantify a wider range of metabolites.

To address those points five studies were performed.

The first work (Chapter 3) describes a study of reproducibility on sequences which have been reported in the literature to be capable to detect Glu and Gln. The study was performed on 14 healthy subjects by scanning them twice and repositioning between the two scans. The absolute percentage difference was then computed to assess the accuracy per sequence and metabolite. A good compromise was found in PRESS sequence (TE=80 ms) which was exploited subsequently for the following study on schizophrenic patients (Chapter 4). Twenty-seven early stage schizophrenic patients and twenty-three aged-matched controls were recruited to undergo a protocol including, in two separate sessions, MRS and electroencephalography (EEG). Anterior Cingulate Cortex Glu was found to predict the induced theta activity in healthy controls but not in patients. Furthermore, the NAA values have also been found to be reduced in schizophrenia and linked to N100, an Event Related Potential (ERP) which is well known to be decreased in schizophrenia.

Following on from the findings of the study on the early stage of schizophrenia,

further investigations were undertaken to study the psychotic state occurring in the disease via a functional MRS, where 25mg/kg of ketamine (NMDA antagonist) injection was administered to two groups of rats. The two groups were group-housed and reared in isolation. This work was able to show increase of prefrontal Gln levels in both groups but showed a selective GABA decrease only in isolated rats. It would have been very interesting to be able to detect GABA changes in the study at 3T but the used protocol did not allow its accurate quantification.

Simulations and reliability tests (Chapter 6)were then utilized to optimize a standard sequence to obtain an accurate and reliable GABA concentration. The optimized sequence reproduces the quantification with 12% of accuracy.

The preliminary results of the last study (Chapter 7) give an evidence of the potential of combined use of Monte Carlo, Levenberg-Marquardt and NNLS methods embedded in a novel fitting approach for two-dimensional spectra.

The three appendices at the end of this work illustrate the details of some of the algorithms and softwares used throughout the studies.

Part I

Introduction to NMR and MRS

1

Nuclear Magnetic Resonance

Nuclear Magnetic Resonance (NMR) is one of the methods used to investigate matter and it has been extensively described in numerous texts (*Levitt* [2001]). This chapter outlines the main principles of the NMR theory.

1.1 NMR basic principles

The atom contains electrons, negatively charged, and a nucleus that includes protons, positively charged and neutrons that have no charge. The nucleus has three fundamental properties: mass, electronic charge and spin. The spinning motion of nuclei in the matter is the basis of NMR principles. In particular, nuclei with spin angular momentum can interact with a magnetic field: the resonant angular frequency, also called Larmor frequency ω_L, is given by the following equation

$$\omega_L = -\gamma B_0$$
(1.1)

Isotope	Nuclear Spin	$2\pi\gamma$ (MHz/T)	Natural Abundance (%)
1H	1/2	267.52	99.9
13C	1/2	67.28	1.1
14N	1	19.34	99.6
23Na	3/2	70.81	100
19F	1/2	251.81	100
31P	1/2	108.39	100

Table 1.1: Properties of common nuclei used for magnetic resonance (*Levitt* [2001]).

where γ is the gyromagnetic ratio, which is a unique constant for each nuclear isotope. The numerical values for the gyromagnetic ratios of the most common atoms used in NMR are given in table 1.1 together with other properties.

A nucleus is called MR active when either the atomic number or mass number is odd. In this case, the nucleus can align to an external magnetic field because of its magnetic moment. This alignment is specific for each nucleus, thus giving a specific NMR sensitivity. The gyromagnetic ratio determines the proportionality between the spin angular momentum and the magnetic moment according to the following

(1.2)
$$\hat{\mu} = \gamma \hat{S}$$

where $\hat{\mu}$ and $\hat{S}$ are quantum mechanical operators. The magnetic energy E_{mag} of the interactions between the particle and an external magnetic field is the scalar product of the particle's magnetic moment $\vec{\mu}$ and the external magnetic field $\vec{B}$

$$(1.3) \qquad\qquad E_{mag} = -\vec{\mu} \cdot \vec{B}$$

thus meaning that the lower state energy is for parallel vectors. Hydrogen nuclei are the most common and abundant in biological matter and since no other nuclei were used for this thesis, 1H NMR is the main subject of the following sections.

1.2 Spin and energy levels

The hydrogen atom consists of an electron and a single proton. As all the nuclei with unpaired nucleons, it has a net nuclear angular momentum, **p**, that is quantised and is given by

$$(1.4) \qquad\qquad \mathbf{p} = \hbar\sqrt{I(I+1)}$$

where $\hbar$ is the Planck constant (6.262×10^{34} J s). The z-component of the angular momentum are given by
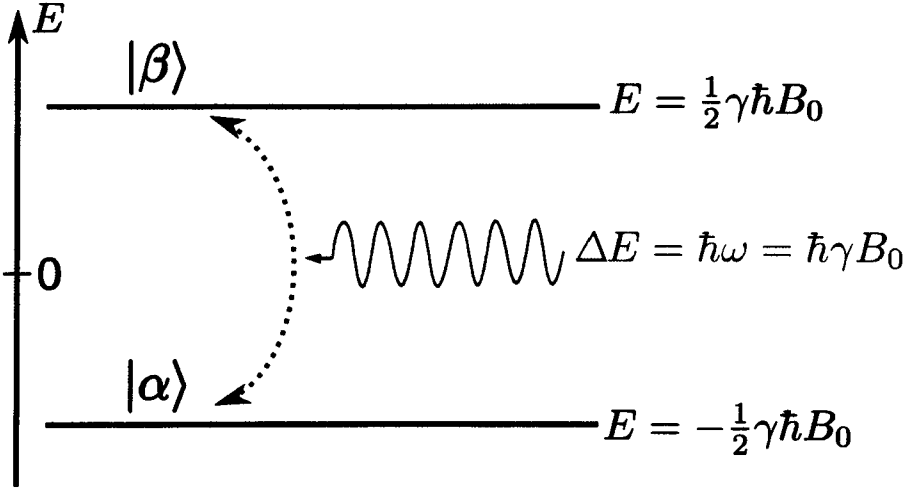
Figure 1.1: Energy level diagram of the hydrogen nucleus (spin 1/2) in a magnetic field. Transitions between the two states are possible when a radiofrequency wave with energy equal to the energy level splitting Δ E is applied.

$$p_z = \hbar m_z \tag{1.5}$$

where m_z can have values -I, -I+1, -I+2, ..., I-2, I-1, I. For the case of hydrogen m_z can be 1/2 and -1/2 since its spin quantum number is 1/2. These values determine the number of degenerate energy states that the system has in the absence of an external magnetic field. The separation between the two allowed energy states, given by $\Delta E = \hbar \gamma B_z$, is known as Zeeman splitting. Spectroscopy involves the application of an electromagnetic field to introduce transitions between the two spin states, figure 1.1.

1.3 Bulk magnetisation

Real systems consist of many individual spins and the observed macroscopic quantities reflect the average response from the sample. The bulk magnetisation is the superposition of the multiple magnetic moments in a sample exposed to an external magnetic field. Boltzmann statistics is used when describing the population of the states for an ensemble of noninteracting spins. In particular, it gives the distribution of the spins in the two energy states described earlier as the following

(1.6)
$$\frac{N_\beta}{N_\alpha} = e^{-\frac{\Delta E}{kT}} = e^{-\frac{\hbar \gamma B_0}{kT}}$$

where k is the Boltzmann constant (1.38×10^{-23} J/K) and T is the temperature. Since the Zeeman energy is small compared to thermal energy at normal room temperature i.e. $k_B T \gg \hbar \gamma B_z$, the difference in population between the two states can be approximated to:

(1.7)
$$N_\alpha - N_\beta \approx \frac{N \hbar \gamma B_z}{2 k_B T}$$

where N is the total number of spins in the system. Equation 1.7 clearly shows the difference which for a macroscopic sample containing one million nuclear spins at 37°C and in magnetic fields of 7 T and of 3T is only 2.3 spins (corresponding to 0.0023%) and 1 spin (corresponding to 0.00098%) respectively.

This means that the z-component of the magnetisation, m_z, is defined by the thermal equilibrium of the system and it depends on the temperature and on the strength of the external magnetic field B_0.

Since decreasing the temperature of the sample is not feasible in clinical applications, increasing the magnetic field strength seems to be the best option to increase the NMR signal.

1.4   Bloch equations and Relaxation

The behaviour of the expectation value of the bulk magnetization **M** can be described in terms of classical equations, and in particular:

$$(1.8) \qquad \frac{d\mathbf{M(t)}}{dt} = \gamma(\mathbf{M(t)} \times \mathbf{B(t)})$$

Since no net x and y component of $\mathbf{M(t)}$ is present at thermal equilibrium, no NMR signal can be detected. From equation 1.8 it follows that M_z can be perturbed by a second magnetic field perpendicular to M_z. This field is rotating at the Larmor frequency in the Radiofrequency (RF) range of the electromagnetic spectrum, it is often referred to as a RF magnetic field. The magnetic component of a RF field that is linearly polarized along the x axis in the laboratory frame can be written as:

$$(1.9) \qquad \mathbf{B}_1(t) = \mathbf{B}_1^{max}(t) \cos \omega t \hat{x}$$

The equation 1.9 in presence of this new field $\mathbf{B}_1(t)$ can be written as:

$$(1.10) \qquad \frac{dM_x}{dt} = \gamma M_y B_0$$

$$(1.11) \qquad \frac{dM_y}{dt} = \gamma (M_z B_{1x} - M_x B_0)$$

$$(1.12) \qquad \frac{dM_z}{dt} = - \gamma M_y B_{1x}$$

From these equations of motion it can again be found that application of an electromagnetic pulse, applied at the Larmor frequency, will cause the magnetization (originally aligned along the z-axis) to be tipped into the transverse plane through an angle given by $\theta = \gamma B_1 T$ (where T is the duration of the pulse).

After the magnetization is tipped into the transversal plane an important phenomenon occurs, the relaxation. That is the process of return to thermal equilibrium after a perturbation. Components of the magnetization $\mathbf{M}$ (i.e. M_x, M_y and M_z) return to thermal equilibrium in an exponential manner. The components perpendicular (i.e. M_x and M_y) and parallel (i.e. M_z) to B0 relax with different time constants.

1.4.1 Longitudinal T_1 relaxation

Relaxation in the z-axis is called longitudinal, spin-lattice or T_1 relaxation and it is described by the Bloch equation

$$(1.13) \qquad \frac{dM_z}{dt} = \frac{(M_0 - M_z)}{T_1}$$

where M_0 is the longitudinal magnetisation at equilibrium and T_1 is the longitudinal relaxation time. T_1 is specific for different kinds of matter and depends on the magnetic field strength: the higher the magnetic field the longer the T_1. It is possible to calculate the Bloch equation for two particular pulses: a 180° inversion pulse and a 90° readout pulse. In the first case, the magnetisation is completely inverted which means that $M_z(0) = -M_0$. One can then write the equation as

$$(1.14) \qquad M_z(t) = M_0(1 - 2e^{-t/T_1})$$

For the case of a 90° readout pulse the equation becomes

$$(1.15) \qquad M_z(t) = M_0(1 - M_0e^{-t/T_1})$$

which is usually called saturation recovery curve. The two curve are represented in figure 1.2

1.4.2   Transverse T_2 relaxation

The previous section presented the relaxation due to the dipole-dipole interactions at the Larmor frequency. Another relaxation phenomenon, due to the short range spin-spin interactions, is called transverse or T_2 relaxation. As for T_1, the T_2 constant also depends on the magnetic field strength. In analogy with the previous case it is possible to write
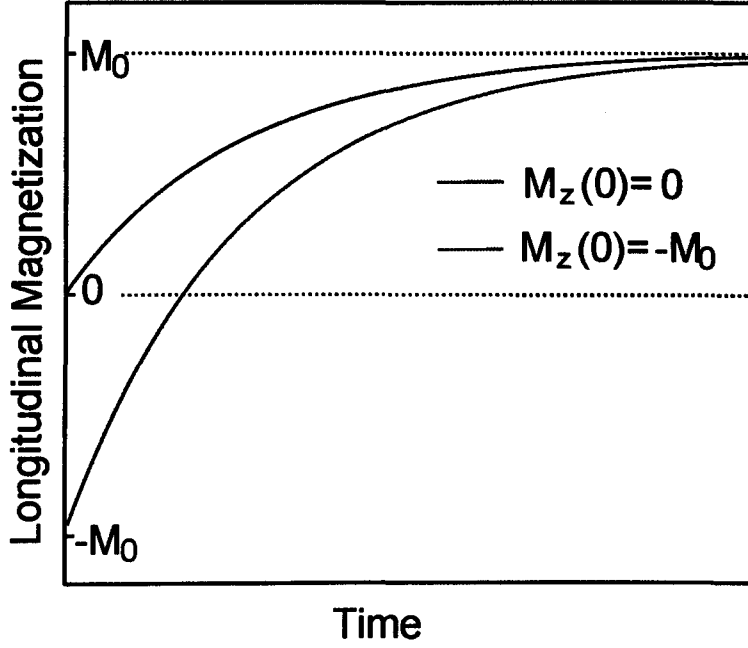
Figure 1.2: Illustration of the function of time for inversion recovery (red solid line) and saturation recovery (blue solid line).

the Bloch equation describing the behaviour of the magnetisation in the transverse plane as follows

$$(1.16) \qquad \frac{dM_{x,y}}{dt} = -\frac{(M_{x,y})}{T_2}$$

where T_2 is the transverse relaxation time. The T_2 constant is always smaller than T_1 and it tends to be shorter when the molecules where the spins are in are more rigid and less free, while in molecules as water it tends to be longer because they are more mobile. Following the application of the RF pulse, these dipole-dipole interactions cause an exchange of energy and a consequent loss of coherence of the transverse magnetisation.

The decay of the amplitude of the transverse magnetisation follows an exponential decay as described by the following equation

$$(1.17) \qquad M_{x,y}(t) = M_0(e^{-t/T_2})$$

This signal decay is known as Free Induction Decay (FID) and it is a key concept when considering the signal "echoes".

At this point it is important to consider that in real systems, the NMR signal decays faster than just described. This further decay is due to the B_0 field inhomogeneities, which can be described by the constant T_2'. The total relaxation time is then the following

$$(1.18) \qquad \frac{1}{T_2^*} = \frac{1}{T_2} + \frac{1}{T_2'}$$

where T_2^* results always shorter than T_2. Figure 1.3 illustrates the FID decay considering the T_2^* effect.

In general, including the relaxation effect into the equation 1.9 the Bloch equation can be deducted:

$$(1.19) \qquad \frac{d\mathbf{M(t)}}{dt} = \gamma(\mathbf{M(t)} \times \mathbf{B(t)}) - \left(\frac{M_x}{T_2}\right)\hat{x} - \left(\frac{M_y}{T_2}\right)\hat{y} - \left(\frac{(M_0 - M_z)}{T_1}\right)\hat{z}$$
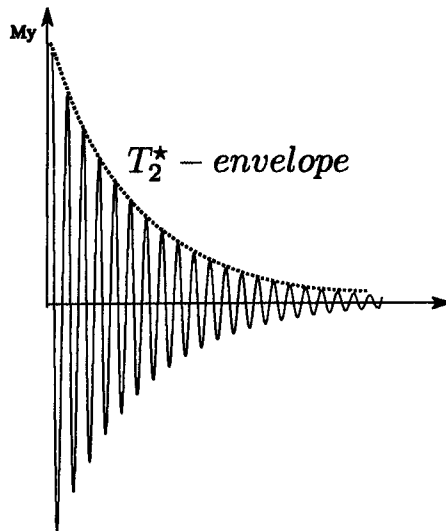
Figure 1.3: Illustration of the FID decay (blue line) over time showing the T_2* effect (red line).

2

Magnetic Resonance Spectroscopy

Magnetic Resonance Spectroscopy (MRS) has been widely studied and described since its discovery. This chapter gives an overview of the basic principles and the methods which are extensively reported elsewhere (*R. A. De Graaf* [2007], *Bernstein et al.* [2004]).

2.1 Quantum description of NMR

The energies and the wavefunctions of atoms and molecules can be obtained by solving the following Schroedinger equation

$$\hat{\mathcal{H}}\Psi = E\Psi$$

(2.1)

Nuclear spin states can be described with an analogous expression but $\hat{\mathcal{H}}$ and Ψ are very different. Instead of differential operators ∇^2 and position operator functions, the hamiltonian $\mathcal{H}$ contains spin angular momentum terms $\hbar\hat{\mathcal{I}}_x$, $\hbar\hat{\mathcal{I}}_y$, $\hbar\hat{\mathcal{I}}_z$. It may be shown

that the three angular momentum operators obey the commutation relationship, thus having

$$(2.2) \qquad\qquad [\hat{\mathcal{I}}_i, \hat{\mathcal{I}}_j] = i\epsilon_{ijk}\hat{\mathcal{I}}_k,$$

and each of them also commutes with the operator

$$(2.3) \qquad\qquad \hat{\mathcal{I}}^2 = \hat{\mathcal{I}}_x^2 + \hat{\mathcal{I}}_y^2 + \hat{\mathcal{I}}_z^2,$$

In order to describe the quantum state of a system it is useful to introduce the ket notation in the Hilbert space, which is considered discrete and finite-dimensional for convenience. Every ket is associated to a possible state of the system and has a corresponding bra $|n\rangle$ and they obey tho the following orthonormalization condition

$$(2.4) \qquad\qquad \langle m \mid n \rangle = \delta_{mn}$$

It possible to choose as a state ket, one set of normal autofunctions of $\hat{\mathcal{I}}^2$ and $\hat{\mathcal{I}}_z$ which we may indicate as $|I, m\rangle$ and we can define the shift operators $\hat{\mathcal{I}}_+$ and $\hat{\mathcal{I}}_-$ as

(2.5)
$$\hat{\mathcal{I}}_+ = \hat{\mathcal{I}}_x + i\hat{\mathcal{I}}_y,$$

(2.6)
$$\hat{\mathcal{I}}_- = \hat{\mathcal{I}}_x - i\hat{\mathcal{I}}_y.$$

The shift operators obey the cyclic commutation relationship 2.2, therefore we can describe the result of applying such operators to the set of autofunctions $|I, m\rangle$ as

(2.7)
$$\hat{\mathcal{I}}^2|I, m\rangle = [I(I + 1)]^{1/2}|Im\rangle,$$

(2.8)
$$\hat{\mathcal{I}}_z|I, m\rangle = m|I, m\rangle,$$

(2.9)
$$\hat{\mathcal{I}}_+|I, m\rangle = [I(I + 1) - m(m + 1)]^{1/2}|I, m + 1\rangle,$$

(2.10)
$$\hat{\mathcal{I}}_-|I, m\rangle = [I(I + 1) - m(m - 1)]^{1/2}|I, m - 1\rangle,$$

2.1.1 Zeeman hamiltonian

The spin hamiltonian $\hat{\mathcal{H}}$ for the interaction of each spin with the static magnetic field $\mathbf{B}_0$ is given by

$$(2.11) \qquad \hat{\mathcal{H}} = -\sum_{j=1}^{N} \gamma_j \hbar \mathbf{B}_0 \cdot \hat{\mathbf{I}}_j$$

Considering only the longitudinal contribution of the static magnetic field and $\hbar = 1$, equation 2.11 can be simplified as

$$(2.12) \qquad \hat{\mathcal{H}} = -\sum_{j=1}^{N} \omega_{0j} \hat{I}_{zj} \quad \text{with } \omega_{0j} = \gamma_j B_0$$

This is called nuclear Zeeman interaction. The result of applying the operator $\hat{\mathcal{H}}$ on $|I, m\rangle$ gives the sum of the energies of the spins as

$$(2.13) \qquad E = \sum_{j=1}^{N} \omega_{0j}$$

2.1.2 Chemical Shift

The resonance frequency of a nucleus doesn't depend only on the gyromagnetic ratio γ and the external magnetic field B_0 but also on its chemical environment. This phe-

nomenon, called chemical shift, is caused by the shielding of the electrons that surround the nucleus: in fact, electrons in the molecules cause small changes in the magnetic field experienced by the nuclei, so nuclei in different chemical environments experience slightly different fields. In particular, the electrons reduce the magnetic field that is sensed by a nucleus because they orbit the nuclei, so to have an associated magnetic moment that opposes the applied B_0. In order to describe the chemical shift phenomenon it is possible to write the equation for the effective magnetic field at the nucleus as

$$(2.14) \qquad\qquad B(\sigma) = B_0(1 - \sigma)$$

where σ is the chemical shift shielding constant for the nucleus which is a dimensionless number usually expressed in parts per million (ppm). Under fully relaxed conditions the ratios of the signals at different frequencies in the spectrum indicates the relative number of protons associated with that particular environment.

The Zeeman hamiltonian including the chemical shift for each nuclei is then given by:

$$(2.15) \qquad \hat{\mathcal{H}}(\bar{\sigma}) = -\sum_{j=1}^{N} \omega_{0j}(\sigma_j)\hat{I}_{zj} \;\; \text{with} \;\; \omega_{0j}(\sigma_j) = \gamma_j B(\sigma_j)$$

The chemical shift of a nucleus is usually measured relative to the shift of a 'reference'

peak in ppm calculated by:

$$(2.16) \qquad \delta(ppm) = \frac{(\nu_{ref}) - (\nu)}{\nu_{trans}} \times 10^6$$

In this equation ν_{ref} is the frequency of the reference peak, ν is the measured frequency and ν_{trans} is the transmitter frequency of the spectrometer. The reference compound should be chemically inert and its chemical shift should be independent of external variables such as temperature or ionic strength. It should also have a strong singlet resonance peak separated from the others. Tetramethylsilane (TMS) is usually used as reference compound for 1H and 13C NMR. However, TMS is not present in *in vivo* systems, therefore it cannot be used as an internal reference. For *in vivo* applications, internal references are the methyl resonance of N-acetyl aspartate (2.01 ppm) for 1H MRS of the brain and the phosphocreatine resonance (0.00 ppm) for 31P MRS of brain and muscle.

2.1.3 Dipole-Dipole Coupling

Dipole-dipole interaction involves the interaction between two spins, each of which generates a magnetic field with direction dependent on the orientation of the spin. Dipole-dipole coupling is dependent on the direct interaction of the nuclear spins with each and can occur between different nuclear spins within a molecule, or between spins in adjacent molecules. For two nuclear spins (j and k), the hamiltonian describing this interaction is given by:

(2.17)
$$\hat{\mathcal{H}}^{dd}_{(j.k)} = b_{jk}\left(3(\mathbf{I_j}\cdot\mathbf{e_{jk}})(\mathbf{I_k}\cdot\mathbf{e_{jk}}) - \mathbf{I_j}\cdot\mathbf{I_k}\right)$$

where b_{jk} is the dipole-dipole coupling constant given by

(2.18)
$$b_{jk} = -\frac{\mu_0}{4\pi}\frac{\gamma_j\gamma_k\hbar}{r_{jk}^3},$$

$\mathbf{e_{jk}}$ is a unit vector in the direction along a line joining the two nuclei centres and r_{jk} is the distance between the two spins.

Even though dipolar interactions are the main mechanism for relaxation in liquids, the dipole-dipole coupling term averages to zero over time because of the rapid molecular tumbling and therefore the dipole-dipole terms are not included in the hamiltonian.

2.1.4   J-Coupling

J-coupling is an NMR phenomenon in which protons in adjacent groups of the same molecule interact with one another and split the resonance frequency into doublet, triplet, quadruplet and so forth. This interaction between the nuclei in a molecule is via the bonding electrons. For an isotropic liquid we discriminate between the homonuclear or heteronuclear cases.

The Hamiltonian for the homonuclear, i.e. nuclei of the same species, (e.g $^1H -^1 H$)

case is given by:

$$(2.19) \qquad\qquad \hat{\mathcal{H}}_{jk} = 2\pi J_{(jk)} \mathbf{I}_{(j)} \cdot \mathbf{I}_{(k)}$$

where $J_{(jk)}$ the j-coupling tensor, a 3×3 real matrix. It depends on molecular orientation. In isotropic liquid it reduces to a number which is called scalar coupling.

The value of $J_{(jk)}$ depends on the effect that the spin orientation has on the energy and is generally positive, in which case the energy is increased if the spins are parallel and decreased if they are anti-parallel.

If we consider two nuclei (j and k) with a covalent bond ($J_{(jk)} > 0$), there can be four different possible spin-orientations, with the most likely, i.e. with lower energy, being the one in which the spins are anti-parallel. The transitions from parallel to anti-parallel and from anti-parallel to parallel have slightly different energies, therefore the resonance peak is split into two peaks of equal intensity as each transition has the same probability to happen. The splitting of the peak due to spin k is also split into two equal components in the same way.

2.2 Radiofrequency Pulses and Gradients

2.2.1 RF Pulses

As we have already stated, in order to observe nuclear magnetization, the precessional motion needs to be detected. However, at thermal equilibrium, the spins have no phase

coherence in the transverse plane and the net longitudinal magnetization is a static vector. Nuclear magnetization can only be observed by rotating the net longitudinal magnetization towards or onto the transverse plane. This can be accomplished by a second magnetic field in the transverse plane oscillating in the RF (MHz) range, the radiofrequency pulses: $B_1(\omega)$. They are the primary tools used to perform the desired spin manipulations like excitation, inversion and refocusing. Short, intense, constant-amplitude RF pulses (i.e. square RF pulses) are often used to achieve uniform excitation of the spins across a given frequency range. However, many *in vivo* NMR experiments require more sophisticated RF pulses.

Square RF Pulses

When the amplitude of the RF pulse $|\gamma B_1| \gg |\Delta\Omega|$ (where $\Delta\Omega = \omega - \omega_0$, respectively the difference between the irradiating field B_1 and the Larmor frequency), the effects off-resonance can be neglected and the nutation angle θ is

$$(2.20) \qquad\qquad \theta = \gamma B_1 T$$

where T is the pulse length. However, the off-resonance effects cannot be always ignored since it is possible that the spectra width is similar to the strength of RF field. In this situation the magnetization will not rotate about B_1, but about tilted effective field B_e

(figure 2.1) the amplitude and tilting angle ψ of which are given by

$$(2.21) \qquad\qquad B_e = \sqrt{B_1^2 + (\frac{\Delta\Omega}{\gamma})^2}$$

$$(2.22) \qquad\qquad \psi = arctan(\frac{\Delta\Omega}{\gamma B_1})$$

The equation 2.20 should therefore, in the case of non-negligible off-resonance, be modified to:

$$(2.23) \qquad\qquad \theta = \gamma B_e T$$

As you can see in the figure 2.1, the rotation axis is B_e. In this case, the actual rotation becomes more complex that a rotation about the $B_1\widehat{x}'$ and it involves sequential rotations about different axis. Such rotations around arbitrary axis are easily described by rotations about the principal axis x', y', z'. The general procedure to determine the rotated magnetization is as follows:

- Performing transformations which align rotation axis B_e with one of coordinate axis (i.e. x') ($R_y(\psi)$)

- Performing rotation about the new axis ($R_x(\theta)$)

- Performing the rotation to bring back the axis ($R_z(-\phi)$)
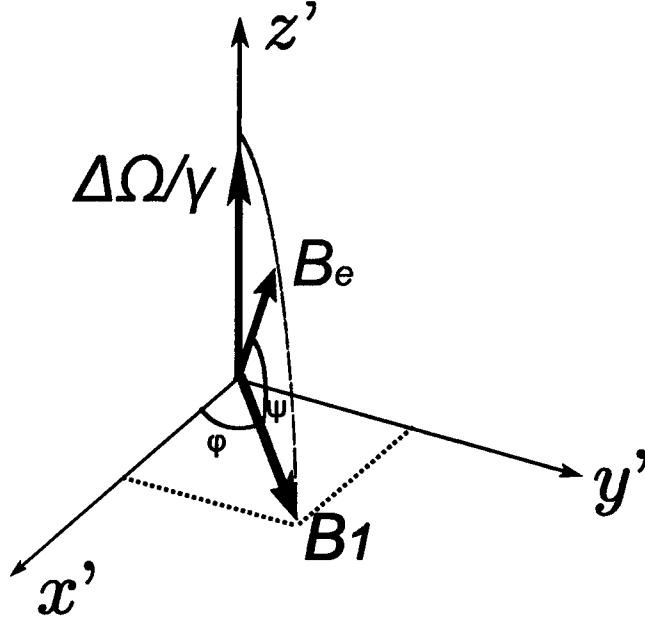
Figure 2.1: In general the magnetization precedes about the B_e which is the vectorial sum of the two magnetic fields present during the spin excitation.

Following these points we can describe the rotations like:

$$(2.24) \qquad R(\theta, \psi) = R_y(-\psi) R_x(\theta) R_y(\psi)$$

Besides the rotation matrix for RF pulse with a phase ϕ relative to the x' axis is obtained with an additional rotation about z'

$$(2.25) \qquad R(\theta, \psi, \phi) = R_z(\phi) R(\theta, \psi) R_z(-\phi)$$

where the rotation matrices are

$$R_x(\alpha) = \begin{bmatrix} 1 & 0 & 0 \\ 0 & \cos\alpha & -\sin\alpha \\ 0 & \sin\alpha & \cos\alpha \end{bmatrix}$$

$$R_y(\beta) = \begin{bmatrix} \cos\beta & 0 & \sin\beta \\ 0 & 1 & 0 \\ -\sin\beta & 0 & \cos\beta \end{bmatrix}$$

$$R_z(\gamma) = \begin{bmatrix} \cos\gamma & -\sin\gamma & 0 \\ \sin\gamma & \cos\gamma & 0 \\ 0 & 0 & 1 \end{bmatrix}$$

and the product of the three matrices as 2.24 is given by

$$R(\theta,\psi) = \begin{bmatrix} \cos^2\psi + \cos\theta\sin^2\psi & \sin\psi\sin\theta & \sin\psi\cos\psi(1-\cos\theta) \\ -\sin\psi\sin\theta & \cos\theta & \cos\psi\sin\theta \\ \sin\psi\cos\psi(1-\cos\theta) & -\cos\psi\sin\theta & \sin^2\psi + \cos\theta\cos^2\psi \end{bmatrix}$$

Considering the thermal equilibrium magnetization along the z' axis such that $\mathbf{M(0)}$ = $M_0\,z'$ and calculating $\mathbf{M(t)} = R(\theta,\psi)\,\mathbf{M(0)}$ we can obtain the magnetization components after the pulse:

$$(2.26) \qquad M_x = M_0 \frac{\gamma B_1 \Delta\Omega}{\gamma^2 B_1^2 + \Delta\Omega^2} \{1 - cos[(\gamma^2 B_1^2 + \Delta\Omega^2)^{\frac{1}{2}} T]\}$$

$$(2.27) \qquad M_y = M_0 \frac{\gamma B_1}{(\gamma^2 B_1^2 + \Delta\Omega^2)^{\frac{1}{2}}} sin[(\gamma^2 B_1^2 + \Delta\Omega^2)^{\frac{1}{2}} T]$$

$$(2.28) \qquad M_z = \frac{M_0}{\gamma^2 B_1^2 + \Delta\Omega^2} \{\Delta\Omega^2 + \gamma^2 B_1^2 cos[(\gamma^2 B_1^2 + \Delta\Omega^2)^{\frac{1}{2}} T]\}$$

The figures 2.2(a), 2.2(b) and 2.3 show the effect of off-resonance frequencies on the magnetization profiles. In the case of 180° pulse M_z is inverted only for values of $\Delta\Omega/\gamma B_1$ approximately close to zero.
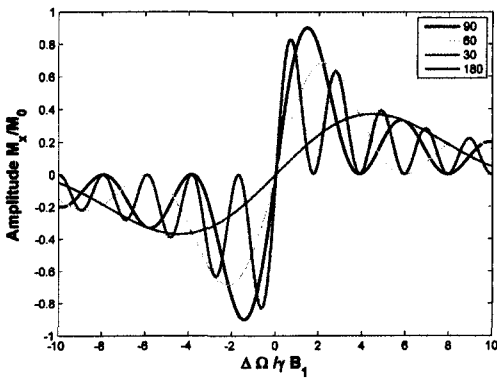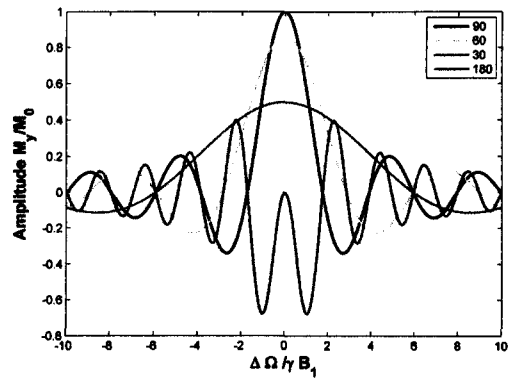
(a) M_x (b) M_y

Figure 2.2: Off-resonance frequency dependence of the M_x and M_y components to different angles square RF pulses.
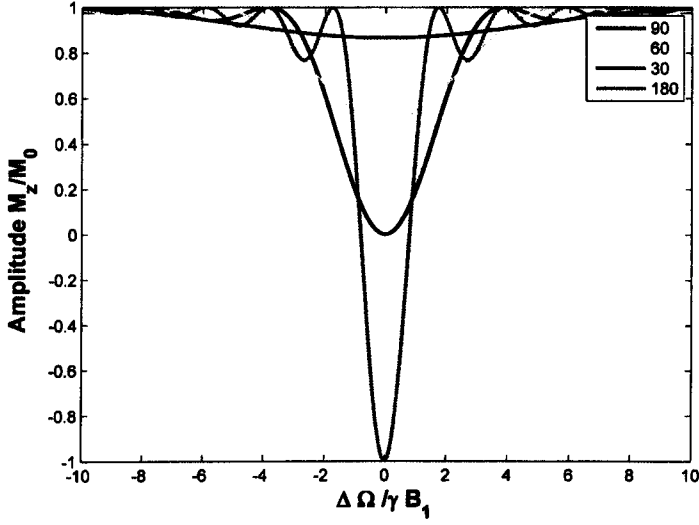
Figure 2.3: Off-resonance frequency dependence of the M_z component to different angles square RF pulses.

Fourier transformation is commonly used in NMR to calculate the frequency profile of the RF pulses. For a squared pulse of length T, M_x and M_y can be calculated by Fourier transformation. In general we can simply calculate that by:

(2.29)

$$\widehat{\mathcal{B}}(\Delta\Omega) = \int_{-\infty}^{+\infty} \mathcal{B}(t) \, e^{-i\Delta\Omega t} \, dt = \int_{-\infty}^{+\infty} \mathcal{B}(H(t) - H(t - T)) \, e^{-i\Delta\Omega t} \, dt = \int_{0}^{T} \mathcal{B} \, e^{-i\Delta\Omega t} \, dt$$

where H is the Heaviside step function to describe the rectangular function.

The real and imaginary components will give the transverse magnetization profile for both the components:

(2.30)
$$M_x = M_0 \frac{1 - cos(\Delta\Omega \cdot T)}{\Delta\Omega \cdot T}$$

$$(2.31) \qquad M_y = M_0 \frac{sin(\Delta\Omega \cdot T)}{\Delta\Omega \cdot T}$$

From the comparison with the equations 2.26 and 2.27, it is evident that the Fourier Transformation does not reproduce exactly the frequency profile. The reason relies upon the linearity of the Fourier transformation: in fact, signal excitation on NMR is far away from being linear and that causes the observed discrepancies when the nutation angle is not small enough.

In general, hard pulses are very infrequently used. Also, most of the times implementing a hard pulse can be a problem because of poor fidelity with which RF amplifiers can reproduce the waveform discontinuities. However, they are conceptually important to approximate the computation of shaped pulses by segmenting the pulse in parts small enough such that the RF amplitude is considered constant.

Selective Pulses: sinc pulses

For many applications selective excitation is required. In fact the sinc-like excitation profile of an hard pulse might significantly excite spins off-resonance. This leads to the concept of RF pulses which have a well-defined selective frequency profile and hence able to select a certain range of frequencies. From the Fourier transformation theory a rectangular shape profile in the frequency domain has a sinc function shape as Fourier transformation in the time domain. Sinc pulses have been widely used for selective exci-

tation, saturation, and refocusing. Since this pulse would need infinite duration (due to the asymptotic decay of the sinc function), it is normally truncated at zero-crossings. In general a sinc pulse consists of several adjacent lobes of alternating polarity (see figure 2.4). The central lobe has the highest amplitude and is also twice as wide as every other lobe. The amplitude of the lobes progressively decreases on either side of the central lobe, as their polarity alternates. In particular, a sinc-shaped RF pulse of duration T is given by:

$$
(2.32) \qquad \mathbf{B}_1(t) = \begin{cases} A \, \tau_0 \, \dfrac{\sin\left(\frac{\pi t}{\tau_0}\right)}{\pi t}, & -N_L \tau_0 \leq t \leq N_R \tau_0 \\[2mm] 0, & \text{elsewhere} \end{cases}
$$

where A is the peak RF amplitude occurring at t = 0, τ_0 represents one-half the width of the central lobe (which is equal to the full width of each side lobe), and N_L and N_R are the number of zero-crossings in the sinc pulse to the left and right of the central peak, respectively. If NL = NR, the sinc pulse is symmetric. The bandwidth of the sinc pulse can be approximated by:

$$
(2.33) \qquad \Delta\omega \approx \frac{1}{\tau_0}
$$

Naturally, truncating the sinc pulse caused small oscillations in a 30° sinc pulse frequency profile. On the other hand, a non negligible deviation from the ideal behavior occurs for a 180° pulse. However, adding more lobes can solve the wrinkle problem to the frequency profile but it may increase the pulse duration thus leading to prolong the minimum TE

and TR in the sequences.

<div align="center">

(a) One-lobe   (b) Three-lobe   (c) Seven-lobe

</div>
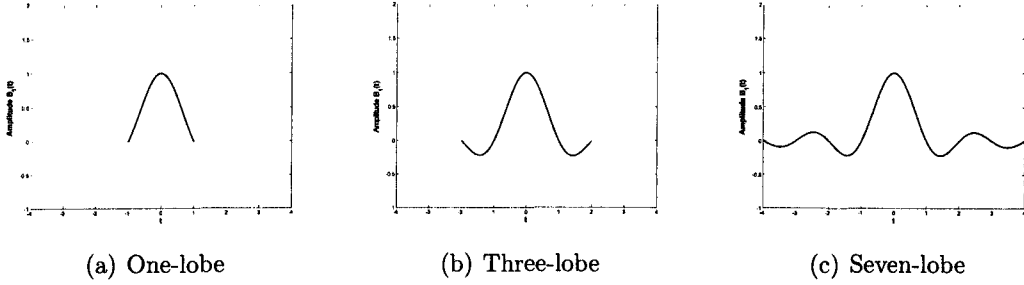
Figure 2.4: Sinc pulse displayed for one-lobe, three-lobe and seven-lobe truncation.

2.2.2 Gradients

Magnetic field gradients are fundamental to MR imaging and spectroscopy because they are responsible for the spatial encoding of the NMR signal along the three orthogonal directions (x,y,z). Gradients are also used to minimize image artifacts and reduce the amount of unwanted signal. A magnetic field gradient is produced from a current flowing in loops of coils placed just inside the magnet bore. A gradient vector $\vec{G}$ can be expressed as follows:

$$(2.34) \qquad \vec{G} = \frac{\partial B_z}{\partial x}\hat{x} + \frac{\partial B_z}{\partial y}\hat{y} + \frac{\partial B_z}{\partial z}\hat{z} \equiv G_x\hat{x} + G_y\hat{y} + G_z\hat{z}$$

where $\hat{x}$, $\hat{y}$ and $\hat{z}$ are the unit vectors of the coordinate system and G_x, G_y and G_z are the three orthogonal components of gradient vector $\vec{G}$. Therefore, the gradient's magnetic field depends on both the distance from the centre of the magnet and the

gradient's strength. Equation 2.34 also shows that although gradients are orthogonal to each other, each gradient produces a magnetic field in the z direction given by

$$(2.35) \qquad \vec{B} = (B_0 + G_x x + G_y y + G_z z)\hat{z}$$

At the centre of the gradient set known as the "isocentre", where all three axes cross each other, the effect of any gradient diminishes. Gradient amplitudes are typically expressed in milliteslas per meter (mT/m) and depend on the amount of electric current flowing in the gradient windings as well as the gradient coil size. The direction of the gradient is determined by the sign of the electric current. Typical values for whole-body gradient systems are $\sim$ 10-50 mT/m (80 mT/m for Philips platform in enhanced mode). Furthermore, slew rate is defined as the rate at which the gradient's amplitude changes between zero and its maximum required value and back down. The usual values on currently used 3T scanners are 150-200 mT/m/ms. A gradient lobe is defined as a single gradient pulse shape that starts and ends with zero amplitude. The three basic functions that the gradients perform (frequency encoding, phase encoding and slice selection) often require more than one gradient lobe.

The area A of a gradient lobe when plotted versus time is typically determined by the spectroscopic parameters such as voxel size and pulse bandwidth. The shortest duration gradient lobe is normally used to minimize parameters such as TE and TM. Figure 2.5 shows two common gradient lobe shapes, a triangle and a trapezoid. Gradient pulses in
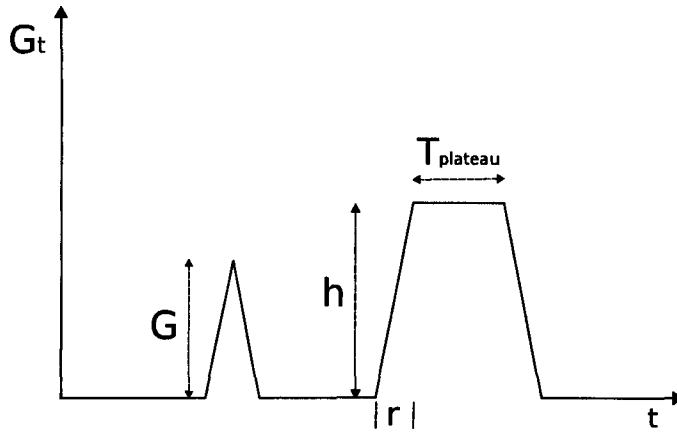
Figure 2.5: Examples of two common gradient lobe shapes, a triangle (left) and a trapezoidal (right). The amplitude of the plateau of the trapezoid is h, the ramp of the trapezoid is r.

conventional pulse sequences are generally designed to be trapezoidal in shape, consisting of sloping rise followed by flat plateau and sloping fall.

The plateau duration $T_{plateau}$ can be calculated as

$$(2.36) \qquad T_{plateau} = \frac{|A|}{h} - r$$

where h is the amplitude of the plateau of the trapezoid and r is the ramp time. Therefore the duration of the entire trapezoidal lobe is

$$(2.37) \qquad T = T_{plateau} + 2r = \frac{|A|}{h} + r$$

The triangle lobe shape is used when the desired gradient area is less hr because it

is the most time-efficient.

In the case of adjacent lobes of the same polarity, some triangle and trapezoidal lobes can be combined, or *bridged*, to improve the time efficiency.

There is a variety of gradient waveforms used to correct or prevent image artifacts:

- **Slice-selection gradient**: slice-selection gradient is a gradient used to achieve the desired spatial localization. The slice-selection gradient (the name comes essentially from imaging) is typically a constant gradient that is played concurrently with the selective RF pulse (see figure 2.6). In the case that the RF pulse performs excitation, then a slice rephasing gradient lobe usually follows the slice-selection gradient. As already said, the selective RF pulse has sinc waveform and its RF bandwidth (expressed in hertz) gives the range of frequencies contained in the RF pulse. The slice-selection gradient translates the band of frequencies into the desired band of locations, corresponding to one of the slices defining the voxel.

- **Slice-refocusing or-rephasing gradients**: an effect of phase dispersion of transverse magnetization can be observed across the excited slice when a slice-selection gradient and a RF selective pulse are contemporarily played. The exact nature of the dispersion is determined by the shape of the RF excitation pulse. The transverse magnetization, for instance, would be linearly phase modulated across the slice if a linear phase RF excitation pulse is used (figure 2.7). To overcome this problem, a slice-refocusing or rephasing lobe is associated with the slice-selection gradient of an excitation pulse. The lobe of this type of gradients has opposite polarity compared to the slice-selection gradient and is indeed used to compensate for
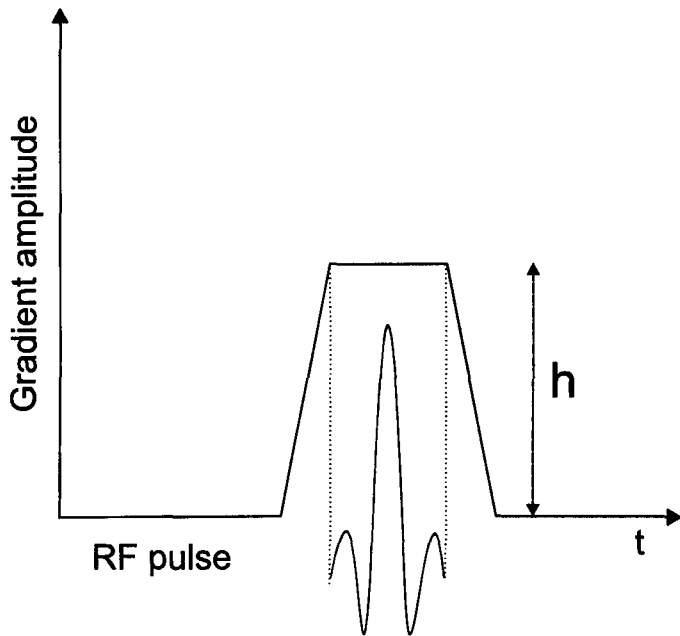
Figure 2.6: Slice selective gradient and RF selective pulse (sinc) concurrently played for slice selection.

the phase dispersion deriving from the slice-selection gradient. This dramatically reduces the signal loss due to the phase dispersion in the voxel. Using the isodelay[1] of an excitation RF pulse function Δt_{iso} to calculate the optimal area of rephasing gradient lobe (see figure 2.8). The optimal area of the slice-refocusing gradient lobe is then:

$$(2.38) \qquad A = \frac{hr}{2} + h\Delta t_{iso}$$

where h represents the gradient amplitude and r indicates the ramp .

- **Crusher gradients**: crusher gradients (figure 2.9) are used to eliminate the FIDs

---

[1]The isodelay of an RF excitation pulse is approximately equal to the time from the peak to the end of the RF excitation pulse.
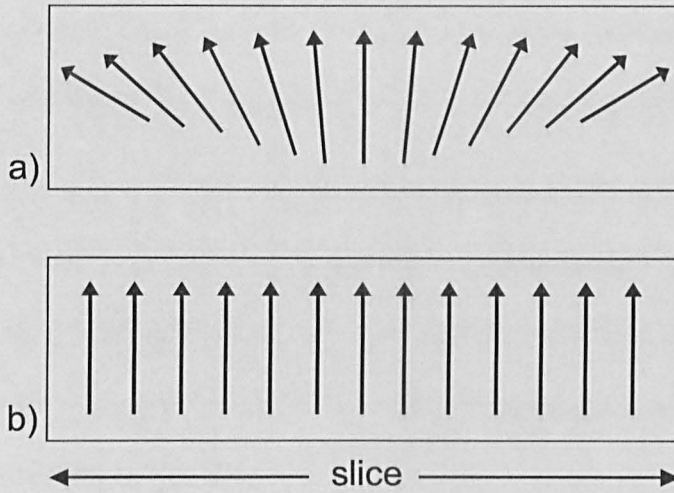
Figure 2.7: After the selective RF pulse is played on one axis on the transversal plane, the transverse magnetization at different spatial locations will generally not lie exactly along its perpendicular axis in the rotating frame because of precession caused by the slice selection gradient.
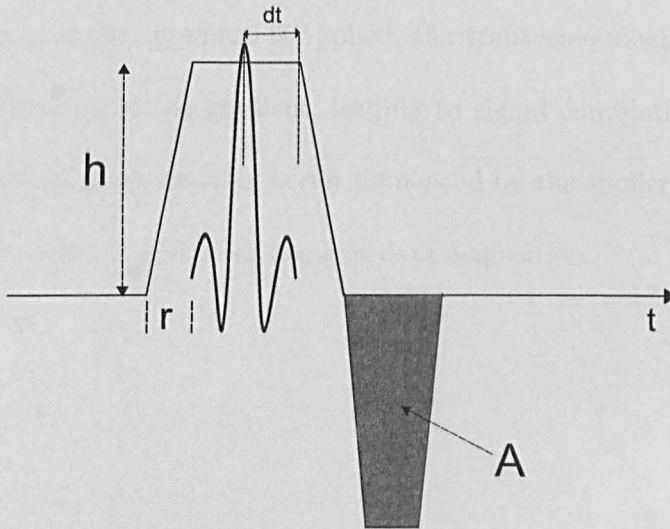
Figure 2.8: Slice selective gradient followed by a rephasing gradient lobe with optimal area computed from the isodelay of the RF selective pulse.

that result from nonideal refocusing pulses by manipulating the phase of the signals. A crusher gradient consist of two lobes with the same polarity, one immediately before the refocusing pulse and the second one immediately after.

Crusher gradients are extensively used in pulse sequences where at least one re-focusing RF pulse is present. For example, in multiple spin-echo pulse sequences, stimulated echoes are crushed out by varying the amplitude of the crusher gradient throughout the echo train so that the acquired signal has a pure T2 exponential decay as a function of the TE.

- **Spoiler gradients**: spoiler gradients (figure 2.10) are designed to eliminate spuri-ous signal due to residual transverse magnetisation at the end of a pulse sequence. If not eliminated, this signal can lead to image artifacts. Therefore, spoiler gradients are usually applied at the end of a pulse sequence or at the end of a preparatory RF pulse. When a spoiler gradient is applied, the transverse magnetisation dephases along the direction of the gradient, leading to signal cancelation within a voxel. The longitudinal magnetisation is not influenced by the spoiler gradient and thus is preserved to give signal in subsequent data acquisition.
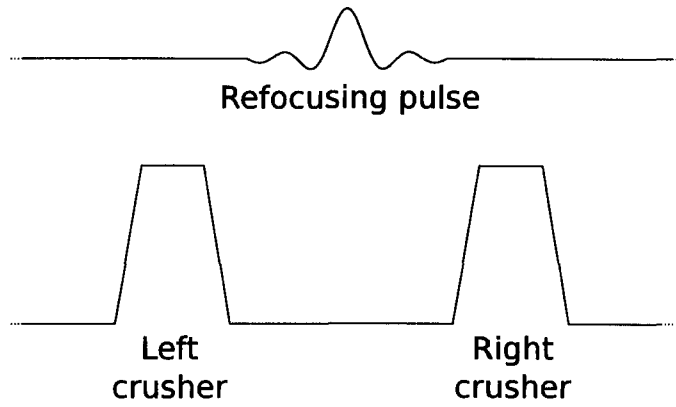
Figure 2.9: Examples of a crusher gradient pair at both sides of a refocusing pulse.
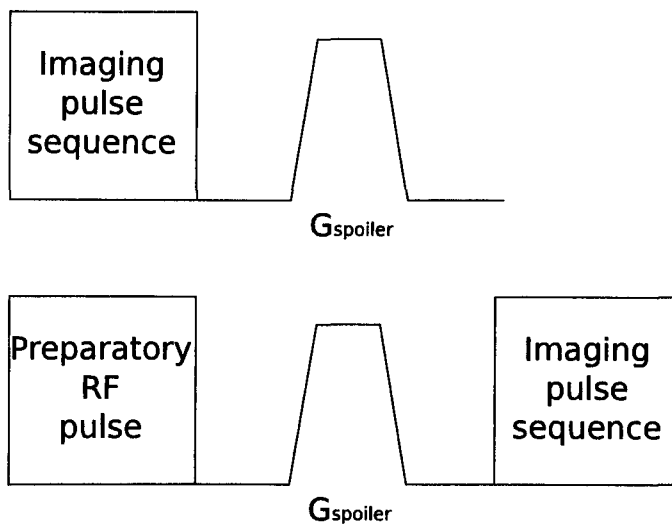
Figure 2.10: Examples of spoiler gradients, applied at the end of a pulse sequence (top) or after a preparatory RF pulse (bottom).

2.3   Single Volume Localization

For *in vivo* MRS it is generally required to restrict signal detection to a well-defined region of interest (ROI). Nevertheless, spatial localization is also used to remove unwanted signals from outside the ROI, like extracranial lipids in MRS applications of the brain. Localization methods based on magnetic field gradients rely on the selection of a spatially selective slice by the application of a frequency-selective RF pulse in presence of a magnetic field gradient.

2.3.1   Point Resolved Spectroscopy (PRESS)

Consider the PRESS sequence of figure 2.11. PRESS consists of a 90° excitation pulse and two $180°$ refocusing pulses. The first $180°$ pulse is played at time $T_{E_1}/2$ after the excitation pulse. A spin echo then is formed at time T_{E_1}. The second $180°$ pulse refocuses this spin echo during a second delay T_{E_2}, such that the final spin echo is formed at time $TE = T_{E_1} + T_{E_2}$. The three RF pulses are frequency selective and are played in combination with magnetic field gradients thus leading PRESS to be capable of three-dimensional localization of a cubic voxel. The three slice selective pulses in combination with the gradients are applied perpendicular to each other so that only spins in the VOI are excited to produce a signal. Signal outside this volume is either not excited or not refocused, leading to rapid dephasing of signal by TE crusher magnetic field gradients. Slice profiles for selective $180°$ pulses tend to be worse than than $90°$ pulses. This results in worse voxel shape and localisation compared with some other techniques (e.g STEAM).

180° pulses also require a larger power output than 90° pulses.

The PRESS sequence becomes increasingly dependent on T_2 as the time between the first and second pulse is increased. This makes PRESS less suitable for detection of signals with short T_2.
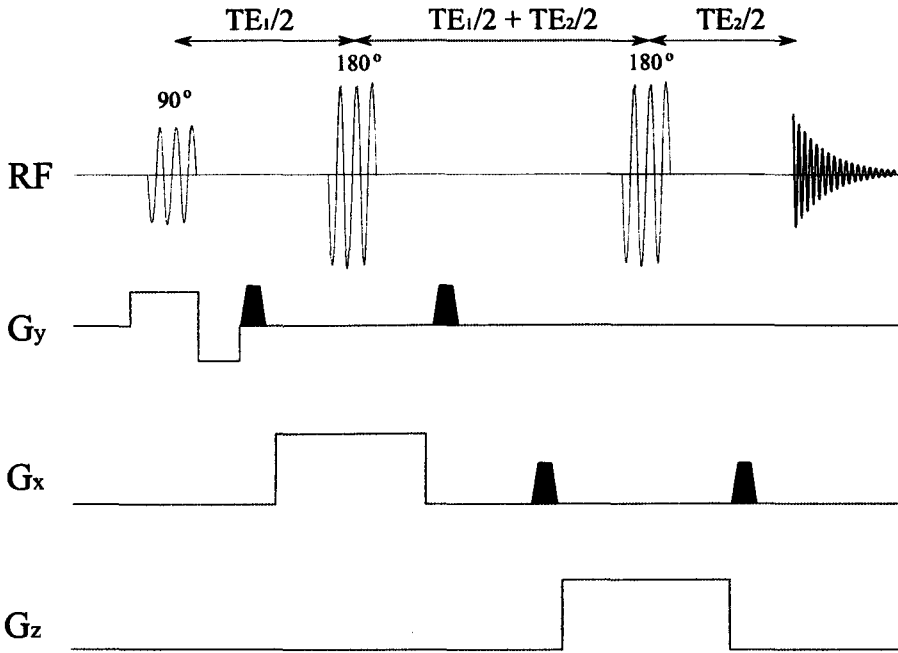
Figure 2.11: The PRESS sequence: the block coloured markers (blu)indicates the crushers gradients whereas the continuous line indicates the selection gradients.

J PRESS

In the localized spectroscopy, in order to resolve the scalar coupling fine structure as well as the chemical shifts of the spectra, a PRESS sequence is adapted to acquire a 2D spectrum. The J-PRESS consists of several PRESS sequences where the echo time is increased at each step. The final result is then several spectra at different TEs. Commonly, the coupling structure is more visible in the frequency domain so that the TE is consid-

ered as a new fictitious temporal variable and a new further Fourier transformation is performed along that variable. Similarly to the line-broadening for 1D spectra due to T_2^* effect, a line broadening is visible along the fictitious variable. In this case, the linewidths are governed only by T_2 effects if diffusion effects are neglected. Due to the signal loss related to T_2 relaxation, the value of the max echo time is limited. The use of this new degree of freedom permits to spreading out the resonances which would be overlapped otherwise thus reaching a better identification of each metabolite.

2.3.2   Stimulated Echo Acquisition Mode Spectroscopy (STEAM)

Like PRESS, STEAM is a localization technique to perform a spectroscopy acquisition from a volume in a single acquisition. The essential difference is that STEAM utilizes three slice-selective 90° pulses and localization is achieved on a spatially selective stimulated echo, rather than on a spin echo as in PRESS. Before describing the STEAM localization technique it is informative to consider the basic pulse sequence (without magnetic field gradients). As Hahn described *Hahn EL* [1950], any pair of RF pulses, of any flip angle, can form a Hahn or partial echo, and each echo can be further refocused by a subsequent RF pulse. The Hahn echoes are smaller in magnitude than spin echoes and have a T_2 dependence. This pulse sequence generate eight echoes and three FIDs.

Figure 2.12 shows on the top the signals which the sequence can generate. S123 is the signal occurring at position 2TM (TM=mixing time) and is due to refocusing by pulses 2 and 3 of magnetization excited by pulse 1. STE is the stimulated echo and occurs at $TE + TM$. In the spectroscopy experiments, the STE is the signal of interest, while the
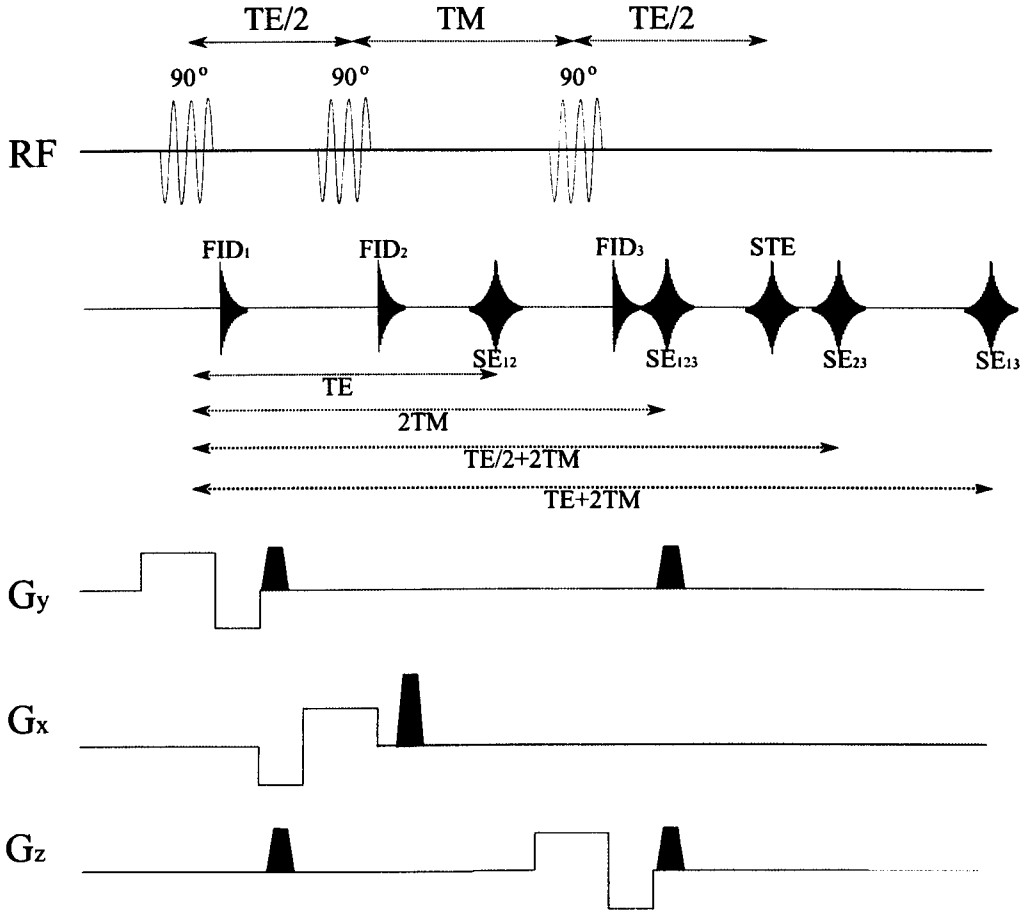
Figure 2.12: The STEAM sequence with slice selective gradients.

S123 is the signal with similar coherence pathway as it is in PRESS.

As it can be seen in figure 2.13, the first 90_y° pulse in combination with its respective gradient rotates all the spins into the transverse plane (A). During a time of $\frac{TE}{2}$ after the first pulse, the magnetization dephases for the effect of TE crusher gradient and B_0 inhomogeneities (B). Following that a second pulse (90_x°) is applied perpendicular to the first, which rotates this magnetisation into the xz plane (C). During time TM, the mixing time, between the second and third pulses 50% of this magnetisation (i.e. all transverse component) is dephased by the TM crasher gradient and only a net coherent longitudinal
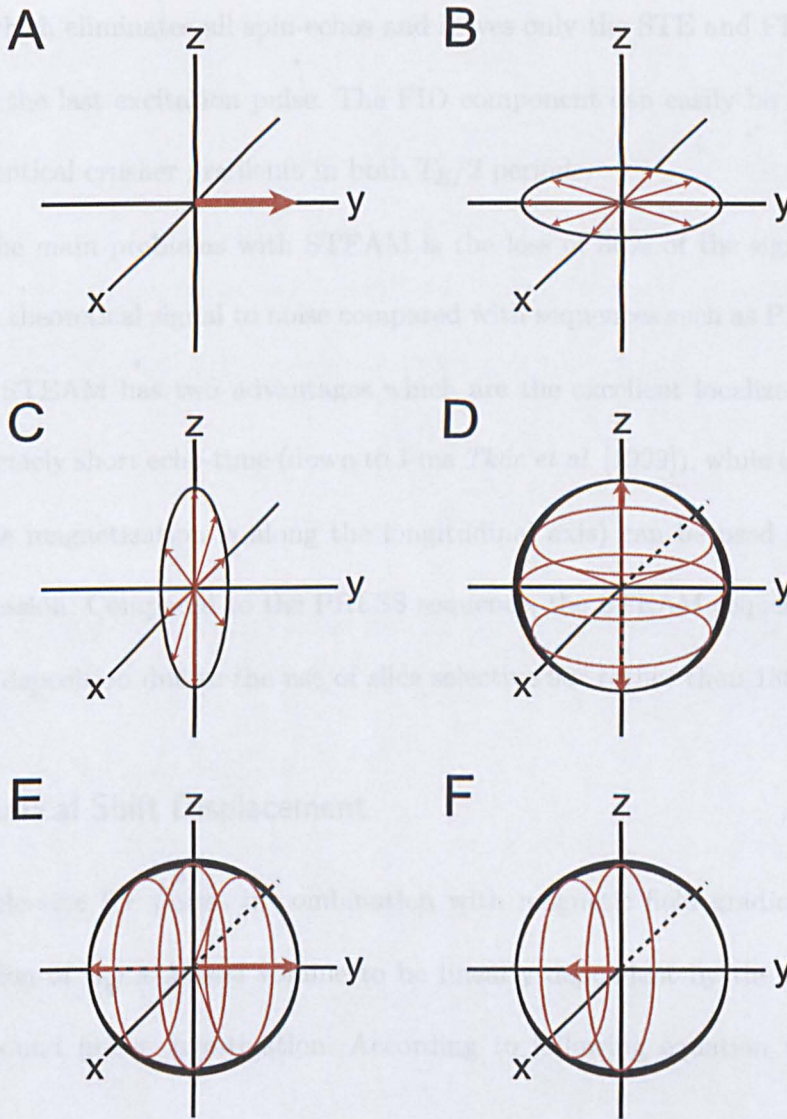
Figure 2.13: Stimulated echo formation in a STEAM sequence. See text for details.

component remains (D). Dephasing the magnetisation means it will not contribute to the

'stimulated echo'. The third 90° pulse rotates the remaining magnetisation back into the

xy plane (E) where a second, matched TE crasher gradient refocuses at time $TE + TM$

to give the stimulated echo (F). In order not to have spurious signals in STE such signals

have to be eliminated. This indeed can be achieved by placing a crusher gradient in the

T_M period which eliminates all spin-echos and leaves only the STE and FID component arising from the last excitation pulse. The FID component can easily be eliminated by including identical crusher gradients in both $T_E/2$ periods.

One of the main problems with STEAM is the loss of 50% of the signal leading to only half the theoretical signal to noise compared with sequences such as PRESS. On the other hand, STEAM has two advantages which are the excellent localization accuracy and the extremely short echo-time (down to 1 ms *Tkác et al.* [1999]), while the TM period (in which the magnetization is along the longitudinal axis) can be used for additional water suppression. Compared to the PRESS sequence, the STEAM sequence has also a lower power deposition due to the use of slice selective 90° rather than 180° pulses.

2.3.3   Chemical Shift Displacement

Frequency selective RF pulses in combination with magnetic field gradients cause the spatial position of the localized volume to be linearly dependent by the chemical shift of the compound under investigation. According to following equation the frequency depends on:

$$ (2.39) \qquad\qquad \omega(\mathbf{r}) = \omega(0) + \gamma \mathbf{r} \cdot \mathbf{G} $$

and in a single direction it becomes:

$$ (2.40) \qquad\qquad \omega(x) = \omega(0) + \gamma x G_x $$

Then, the position x is given:

$$(2.41) \qquad x = \frac{\omega(x) - \omega(0)}{\gamma G_x}$$

Two different compounds having two different Larmor frequencies will have a relative displacement Δx between their localized volumes given by:

$$(2.42) \qquad \Delta x = \frac{\Delta \omega}{\gamma G_x} = \frac{\Delta \omega}{\Delta \omega_{max}} V_x$$

where $\Delta \omega$ represents the difference in Larmor frequencies and where the gradient strength γG_x to select a given voxel size V_x in the x direction is proportional to the spectral bandwidth of the RF pulse $\Delta \omega_{max}$.

An example of a strong effect at 3T is for water and lipids. The difference in Larmor frequency between water and lipids at 3T equals 3.7 ppm (469 Hz). By considering the bandwidth (1354 Hz) of the two 180° refocusing pulses in the PRESS sequence present in the 3T Philips Achieva and a $3 \times 3 \times 3$ cm^3 volume, the displacement between the water and lipid resonances is around 1 cm in each direction selected by the 180° pulses. This could result in misinterpretations of absolute concentrations when tissue, B_0 or B_1 heterogeneity plays an important role.

Furthermore, positioning the voxel in areas close to the skull could lead a severe spectral lipid contamination. This is completely independent from the accuracy of the localization of water as well as metabolites close to the water and can determine an erroneous absolute metabolite quantification. Importantly, non-coupled spins system such as

lipids and water do not present either any signal loss or time-dependent signal modulations. That indeed is the case of homonuclear spin systems which have j-coupling within the same metabolites and resonate at different frequencies.

Consider a homonuclear scalar-coupled A_nX (n=1, 2, 3) spin system. In the case of n spin half-nuclei, the NMR spectrum will consist of an A doublet of relative intensity n and an X (n+1) multiplet of relative intensity one. Since similar conclusions can be reached about the X multiplet behaviour, we focus only on the A doublet. Figure 2.14 A shows the two dimensions of the voxel selected by the two 180° refocusing pulses for spin A. Because of the chemical shift artifact, the voxel for the X spins is shifted in all three dimensions by the amount given in Eq. 2.42 . This has the consequence that not all X nuclei within the A voxel experience the two 180° pulses.

In particular, evolution in the voxel is not homogeneous across the two directions. In all four subvoxels both pulses refocus the X nuclei transverse magnetization. In subvoxel 1, both pulses also refocus the transverse component for A nuclei. At the same time, only the first RF pulse refocuses the transverse component of A nuclei in subvoxel 2, whereas the second RF pulse has no effect on that due to the chemical shift effect in that direction. In subvoxel 3, the first RF pulse has no effect on the transverse component of A nuclei due to the chemical shift effect in that direction, whereas the second RF pulse refocuses its magnetization. Finally, in subvoxel 4 none of the RF pulses affect A nuclei. Therefore, in the presence of chemical shift displacement, the modulation pattern substantially deviates from the ideal co-sinusoidal modulation. Especially for echo times between 1/J and 3/J the signal intensity is substantially reduced to zero when compared
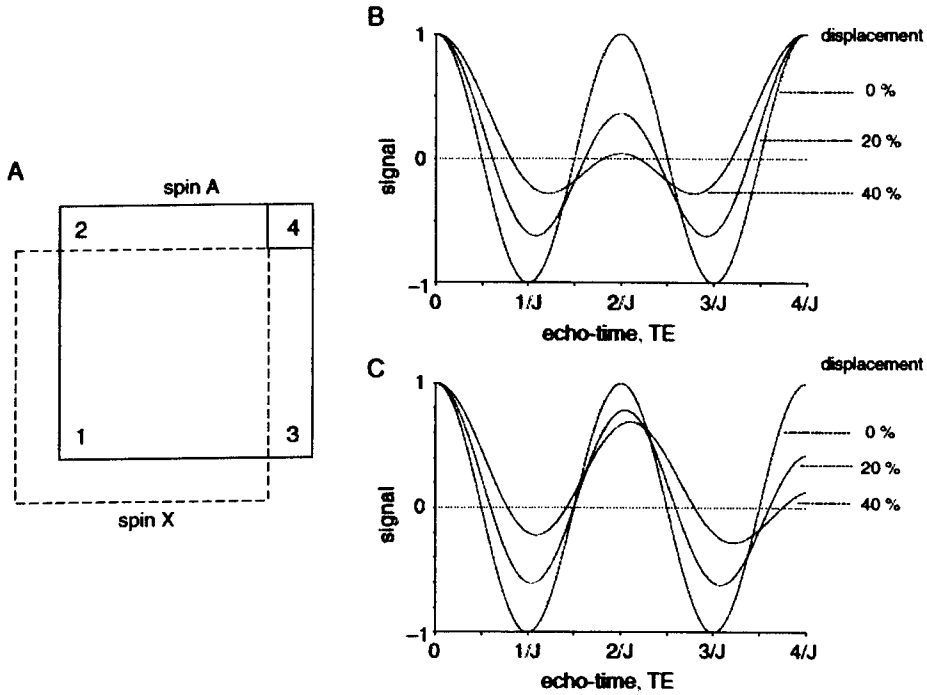
Figure 2.14: from *Graaf and Rothman* [2001]. Effect of PRESS localization on the J-evolution of coupled spins. (A) Displacements of the two-dimensional volumes for spin A (solid line) and for spin X (dotted line) as selected by the two 180° pulses. (B) J-evolution of the A spins in an AX_n n=1, 2, 3 spin system as a function of the echo time T_E ($T_{E_1} = T_{E_2}$). The curves represent voxel displacements of 0 ideal, 20, and 40% of the nominal volume. (C) J-evolution for A_nX spin systems during an asymmetric PRESS sequence ($T_{E_1} = 4T_{E_2}$) with voxel displacements of 0, 20, and 40% of the nominal volume.

to the ideal situation (see figure 2.14 B).

Asymmetrical PRESS sequences with ($T_{E_2}=4T_{E_1}$ present even more complicated signal modulations (figure2.14 C) . From Fig. 2.14 it is evident that an enormous underestimation of the real concentration results if the chemical shift displacement effect is not taken into account.

In order to either minimize or eliminate the unwanted modulations, Yablonskiy *et al* (*Yablonskiy et al.* [1998]) provided a very straightforward solution based on the increase

9

in the RF bandwidth. The chemical shift displacement artifacts gets more severe at higher magnetic fields and the artifact can only be minimized by increasing the magnetic field gradient strength, which (for a constant voxel size) corresponds to an increase in spectral bandwidth of the RF pulse. Unfortunately this option has only limited applicability because the required RF power increases with decreasing pulse length. An increase in RF power implies in turn an increased specific absorption rate (SAR)[2]. On the majority of the human systems one would typically encounter the SAR limitation well before any gradient strength limitations.

2.4 Spectra quantification

2.4.1 Fitting algorithms for spectra quantification

In the last two decades, several *in vivo* NMR signal processing methods for spectra quantification were developed and a substantial improvement for the estimation of metabolic concentrations was made. The new advanced techniques of fitting and the availability of more powerful computers have inspired the creation of new softwares which are much more complex than simple integrations used early on.

Very popular fitting algorithms include the jMRUI package (*Naressi et al.* [2001]), which has got as tools the VARPRO and AMARES (*Vanhamme et al.* [1997]) programs,

---

[2]The SAR keeps into account the electric component of the RF which is dissipated as heat in the conducting material. The specific absorption rate is typically expressed in units of watts per kilogram. The deposited power P during a RF pulse of length T is proportional to the square of the irradiating RF field according to :

$$P \propto \omega^2 \int_0^T B_1^2(t)dt$$

(2.43)
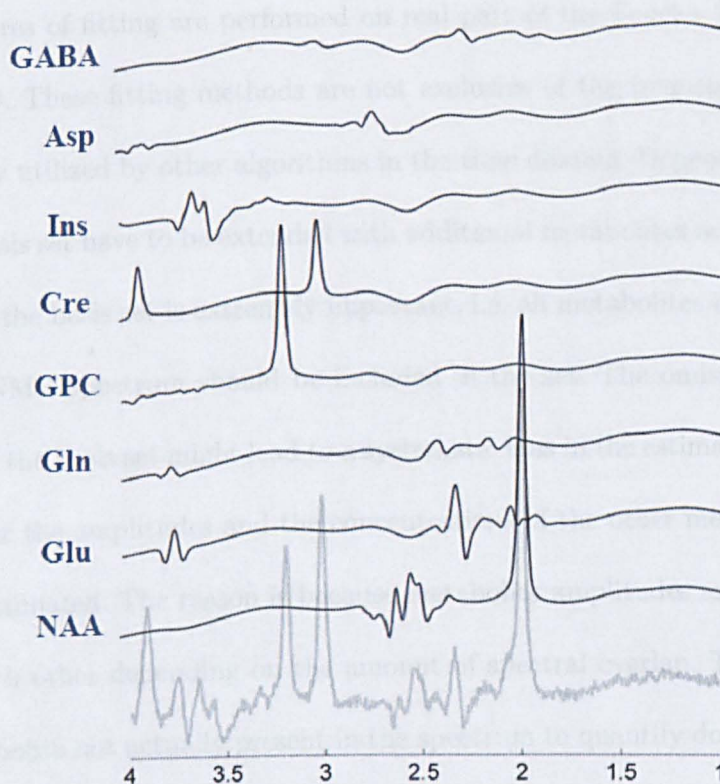
Figure 2.15: Fit of point-resolved spatially localized ^1H MR spectrum TE=80 ms at 3T performed by using LCModel.

LCModel (*Provencher* [1993, 2001]) and others (*Slotboom et al.* [1998] *Wilson et al.* [2010]).

The total NMR signal can be considered as linear combination of the NMR signals from the pure or isolated compounds. This forms the basis for so called linear combination (LC) modeling algorithms (**LCModel**) as it was firstly described by de Graaf and Bovee and successfully embedded in a popular program by Provencher through the LCModel program. With LC modeling algorithms the measured NMR spectrum (typically H) is approximated as a linear combination of metabolite NMR spectra, which commonly referred to as a basis set. The algorithm works only in the frequency domain. This mean

that all procedures of fitting are performed on real part of the Fourier Transformation (FT) of the FID. These fitting methods are not exclusive of the frequency domain but are also similarly utilized by other algorithms in the time domain. Depending on the application, the basis set have to be extended with additional metabolites as necessary. The completeness of the basis set is extremely important, i.e. all metabolites that are present in the *in vivo* NMR spectrum should be included in the set. The omission of a single metabolite from the basis set might lead to a systematic bias in the estimated parameters and in particular the amplitudes and the concentrations of the other metabolites might be under/overestimated. The reason is because metabolite amplitudes are typically correlated with each other depending on the amount of spectral overlap. The inclusion of 'basis set' metabolite not actually present in the spectrum to quantify does typically not generate error or bias because the amplitude of any nonexistent metabolite can simply be set to zero. However, a larger amount of metabolites implies longer calculation times and a slower convergence.

In principle, all LC modeling algorithms work by varying amplitudes, frequencies, line widths and phases of the metabolite basis set such that the modeled spectrum matches the *in vivo* NMR spectrum as close as possible. The usual procedure relies upon least-squares function minimization. The algorithm adds also both soft constraints on the fitting parameters and regularizors in order to achieve faster convergence and to avoid to reach local minima. In addition, short echo-time ^1H NMR spectra are typically characterized also by a significant macromolecular baseline. In order to achieve a meaningful spectral fitting result and also to extract useful information from the components

contributing to the baseline, the macromolecular and lipidic resonances have to be taken into account. The baseline is computed with a cubic spline polynomial function but this introduces a large number of further fitting parameters that are not based on biophysical parameters. Therefore, it is possible to overcome these issues by measuring the contribution to the spectra baseline and by including that into the fitting. The baseline component can indeed be selectively detected, By using the fact that T_1 and T_2 relaxation times of macromolecules and lipids are significantly shorter compared to those of metabolites. Besides, it can be seen that the residual background or baseline signal is very small and can be simply approximated with a low-order polynomial function. A small residue between the fitted and measured NMR spectra does not guarantee a good fitting accuracy whereas a large residue is surely a indicative of a poor spectral fit and hence of a not reliable estimation. This explains the reason why it is important to find a measure for the error of estimated parameters, and in particular for the concentrations, in order to assess the accuracy of the fit.

2.4.2   Cramér Rao Lower Bound (CRLB) for fitting error estimation

In order to have a quantitative confidence of the estimated parameters, it is essential to be able to associate an error to them. That permits either to keep or reject the parameter estimate. One of the main problems of the quantification is that the concentration is obtained from one spectrum only and the standard deviation cannot be calculated with usual statistical tests. So, for a given noise level the lowest possible estimator-independent errors are given by the so-called Cramér-Rao lower bounds (CRLBs) (*Cavassila et al.*

[2001], *Cavassila et al.* [2000]). For a proper evaluation of the CRLBs the experimental data must be fitted with an exactly known model function. The used model functions are only partially corresponding to the real data and as such the calculated CRLBs are only approximate. This is especially true and problematic for data which lacks of a specific model function, such as macromolecular resonances in short echo-time $_1H$ NMR spectra. The CRLBs are independent from the fitting algorithm so that they equally well apply to the time and frequency-domains.

In mathematical terms, supposing that the noiseless data can be exactly modeled by the complex-valued either time or frequency domain model function $\widehat{x}_n$, n = 0,..., N-1, the experimental data x_n can be written as:

$$(2.44) \qquad\qquad x_n = \widehat{x}_n + b_n$$

where b_n is Gaussian-distributed noise. Evaluation of the CRLBs requires the operation of inversion of the Fisher information matrix $\mathbf{F}$ which can be expressed as

$$(2.45) \qquad\qquad \mathbf{F} = \frac{1}{\sigma^2}\Re\left(\mathbf{P}^T\mathbf{D}^H\mathbf{DP}\right)$$

where

$$(2.46) \quad \mathbf{D}_{nl} = \left(\frac{\partial x_n}{\partial p_l}\right) \qquad for \qquad n = 0, 1, , N-1 \qquad and \qquad l = 1, 2, \ldots, N_p.$$

The size of **F** is equal to the number of free real parameters to be estimated. The matrix **P** is the prior knowledge matrix. The superscript H indicates Hermitian conjugation, $\Re$ stands for real part and σ is the standard deviation of the real and imaginary part of the noise. The vector $\mathbf{p} = (p_1, p_2, \ldots, p_{N_p})^T$ represents the N_p real model parameters. To compute the matrix **D** the calculation of the derivatives of the functions x_n with respect to the parameters p_l using their true values has to be performed. Incorporation of prior knowledge and hence the interrelation among the parameters themselves in turn reduces the number of free parameters and consequently the size of the information matrix **F**. For instance, if we assume a linear relations between model parameters, such as $p_l = a p_m$ and $p_l = p_m + b$, in which a and b are real constants, we can write the prior knowledge matrix **P** as the matrix of partial derivatives:

$$\mathbf{P}_{mn} = \left(\frac{\partial p_l}{\partial p'_m} \right) \qquad for \qquad l = 0, 1, \ldots, N_p \qquad and \qquad m = 1, 2, \ldots, L.$$

$p' = (p'_1, p'_2, \ldots, p'_{N_p})^T$ corresponds to the L unconstrained parameters p_l to be estimated. When $L = N_p$, **P** is exactly the identity matrix. The relation between CRLBs and the standard deviations of the estimated parameters p_l is given by the Cramér-Rao inequality

$$(2.47) \qquad \sigma_{p_l} \geq CRLB_{p_l} = \sqrt{\mathbf{F}_{ll}^{-1}}$$

In the particular case of computation of CRLBs of concentrations, c_n, the computation becomes much easier for the presence of linear parameters. In this case, if the model is

described by $c_n \hat{x}_n(p_l)$ where now the p_l are only the non-linear parameters, the $\mathbf{D}$ matrix simply becomes:

$$(2.48) \qquad \mathbf{D} = [\hat{x}_1, \hat{x}_1, \ldots, \hat{x}_n]$$

whereas the Fisher information matrix $\mathbf{F}$ is computed by the linear algebraic product:

$$(2.49) \qquad \mathbf{F} = \frac{1}{\sigma^2} \Re \left(\mathbf{D}^H \mathbf{D} \right)$$

It is generally accepted that metabolite concentrations with CRLB < 20 % are measured with sufficient precision whereas metabolites exceeding 20% should be considered with caution. However, a small CRLB is not a guarantee for an accurate metabolite concentration since an incorrect or incomplete metabolite basis set might also lead to bias the results despite the very low CRLBs. As it can be noticed from the Fisher matrix in equation 2.45 and from expression of the matrix $\mathbf{D}$, the CRLBs increase both with increasing noise level, and with increased spectral overlap.

An estimate of this overlap in an NMR spectrum can be calculated through the so-called parameter correlation matrix that delineates the correlation ρ_{mn} between parameters p_m and p_n according to:

$$\rho_{mn} = \frac{\sqrt{\mathbf{F}_{mn}^{-1}}}{\sqrt{\mathbf{F}_{mm}^{-1}} \sqrt{\mathbf{F}_{nn}^{-1}}}$$

This matrix highlights that, in the presence of noise, strongly correlated concentrations, like those obtained for creatine and phosphocreatine, might lead to erroneous quantification. In those cases, and more specifically when the correlation are larger than 0.5, it is more meaningful to report the values associated to the combined pool, e.g. total creatine, which is typically more reliable and accurate.

2.5 Two Water Suppression Techniques: Frequency selective excitation and VAPOR

The main problem encountered during *in vivo* 1H MRS studies is that the water signal is 10.000 times as abundant as the metabolite concentrations. The large water signal may then distort the baseline and vibration-induced sidebands of the water obscure the metabolite resonance. Therefore, the water signal needs to be suppressed.

The methods of water suppression rely upon differences in magnetic properties between the water molecules and the other metabolites. Thus, differences in chemical shift, scalar coupling, T_1 and T_2 relaxation, diffusion and exchange can also be exploited.

No complete explanation of all techniques for water suppression will be provided but rather the methods utilized throughout this work will be described: frequency selective excitation and VAPOR.

2.6 Frequency selective excitation method

This approach consists of a selective RF pulse which excites the water magnetization onto the transverse plane followed straight after by a magnetic field gradient which dephases all the coherences. The sequence was originally suggested with the name CHESS (CHEmical Shift Selective) (*Haase et al.* [1985]). CHESS is able to leave the metabolite resonances unperturbed and for this reason it can be added at the beginning of any pulse sequences. The delay between CHESS sequence and the first excitation pulse need to be as short as possible to reduce the signal recovery due to T_1. CHESS efficiency strongly depends on the RF pulse performance in selectively exciting the all water magnetization. Hence, the homogeneity of B_0 and B_1 is a key point and a single CHESS element would be sufficient for an accurate water suppression. In practice, the homogeneity is not ideal and several CHESS elements (two to six elements) must be sequentially placed to improve the suppression. Then a series of CHESS elements uniform the suppression to a large range of frequency thus making the suppression less sensitive to frequency offsets caused by B_0 magnetic field inhomogeneity. Furthermore, the performance depends also on the nutation angle and the suppression is perfectly reached only at 90°. In particular, if the relaxation is not taken into account, the residual longitudinal magnetization M(0) after n CHESS elements is a function of the nutation angle $M_z(\theta) = M_0 \cos^n(\theta)$.

Therefore six CHESS elements would lead the residual magnetization along the z axis to be less than 0.035 % for nutation angles, $75^o \leq \theta \leq 105^o$, providing sufficient water suppression with a tolerance to the magnetic field inhomogeneity of 30 % around the nominal nutation angle of 90°.

Some methods have investigated the possibility to create more T_1 and B_0 insensitive CHESS-based water suppression methods by optimizing the inter-pulse delay and the nutation angles of the different CHESS elements (*Ogg et al.* [1994]).

2.7   VAPOR method

The VAPOR method uses optimised frequency-selective perturbations interleaved by optimal T_1 recovery delays to make the suppression insensitive to T_1 and B_0 inhomogeneity. The VAPOR method is reported in figure 2.16. It consists of seven CHESS suppression and seven T_1 recoveries. For a nutation angle β of 95°, the longitudinal magnetization prior to nonselective excitation ends up very close to zero despite the presence of T_1 relaxation. Even when the nutation angle is not corrected calibrated (see different angles on figure 2.16), the magnetization reaches values close to zero due to the optimized pulse and delay combination.
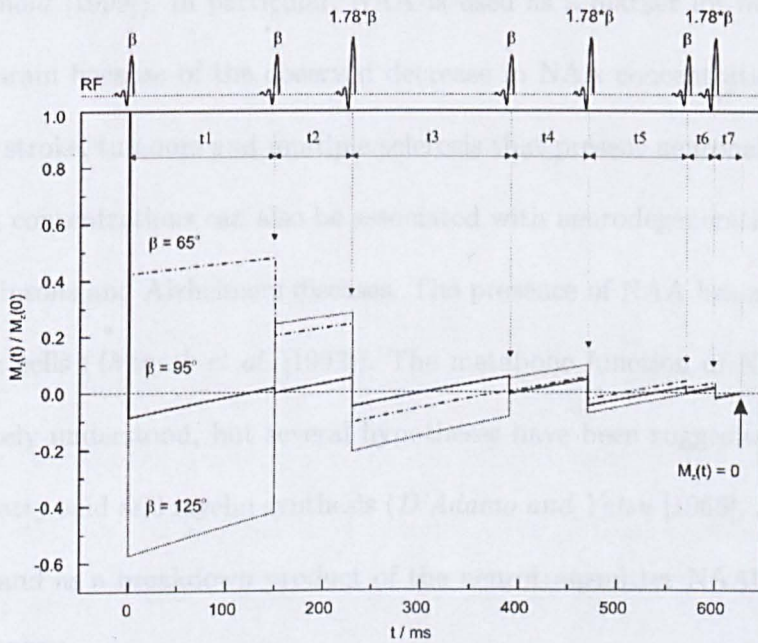
Figure 2.16: From *Tkáč et al.* [1999]. Seven CHESS water suppression scheme (VAPOR) with optimized flip angles and timing.

2.8 Proton MRS in the human brain

The proton nucleus is the most sensitive nucleus for NMR with a high natural abundance ($>$99.9 %) and intrinsic NMR sensitivity (high gyromagnetic ratio). Since nearly all metabolites contain protons, in vivo 1H NMR is used to study the human brain *in vivo* for the detection of a number of important metabolites, such as the ones reported below. An example of a rat brain proton MR spectrum is reported in figure 2.18.

N-Acetyl Aspartate (NAA) NAA is an amino acid present in the brain in relative high concentrations. Being such an abundant metabolite, and having a very high single peak, NAA has been extensively studied *in vivo* especially for the psychiatric and neurologic clinical applications (*Birken and Oldendorf* [1989], *Rudkin*

and Arnold [1999]). In particular, NAA is used as a marker for neuronal density in the brain because of the observed decrease in NAA concentration in disorders such as stroke, tumours and multiple sclerosis that present neuronal loss. Decrease in NAA concentrations can also be associated with neurodegenerative disease such as Parkinsons and Alzheimers diseases. The presence of NAA has also been found in other cells (*Urenjak et al.* [1992]). The metabolic function of NAA is still not completely understood, but several hypotheses have been suggested regarding its role in fatty acid and myelin synthesis (*D'Adamo and Yatsu* [1966], *D'Adamo et al.* [1968]) and as a breakdown product of the neurotransmitter NAAG (*Blakely and Coyle* [1988]).

Glutamate (Glu) and Glutamine (Gln) Glu is the most abundant amino acid in the brain and is the main excitatory neurotransmitter. Its concentration ranges between 6 and 12.5 mM with significant differences between gray and white matter. Glu is present mostly in glutamatergic neurons and also in GABAergic neurons and astroglia.

Gln is an amino acid synthesised from Glu by Gln synthethase in the astroglia and it is broken down to Glu by phosphate-activated glutaminase in neurons. The Glu-Gln neurotransmitter cycle is presented in figure 2.17 Understanding the Glu and Gln role in metabolism is crucial to investigate neurotransmitter activity. Unfortunately, in proton spectroscopy their peak overlap thus leading to the need of high and ultra-high magnetic field strengths. For this reason, it is sometimes useful to give the combined concentration of Glu and Gln, given as Glx (Glu+Gln).

γ-**Aminobutyric Acid (GABA)** GABA is the main inhibitory neurotransmitter, present in the brain with concentrations of about 1 mM, and is linked with the metabolism of Gln and Glu. Changes in GABA concentrations in the brain are associated with neurological and psychiatric disorders. As for the Glu and Gln, at low magnetic fields, there are strong coupling effects.

Choline (Cho) In proton MRS, Cho shows a peak at about 3.2 ppm which is the sum of three different contributes: free choline, Glycerophosphorylcholine (GPC) and Phosphorylcholine (PC). The term "total choline" (tCho) is often used to refer to this peak. The interpretation of the changes in the tCho peak observed with MRS *in vivo* is therefore complicated by the multiple contributions from different metabolites. However, the concentrations of Cho has been found to be varying in some pathologies such as stroke, tumours and neurodegenerative disorders.

Creatine and Phosphocreatine (Cre, PCre) Cr and PCr are present in the brain, blood and muscle and are normally absorbed by the body from food in the diet. The peak from Cr+PCr is very high (after NAA peak) and stable being relatively constant in healthy and diseased brain. Therefore it is often use d as a reference for proton MRS *in vivo*. However, some changes in Cr and PCr concentrations have been reported in some illnesses such as stroke and tumours.

Others Other metabolites that can be studied with proton MRS include Aspartate (Asp), Acetate (Ace), Lactate (Lac), Myo-inositol and Scyllo-inositol.

Table 2.1 reports the typical ranges of metabolic concentration measured in the human

brain with 1H MRS.
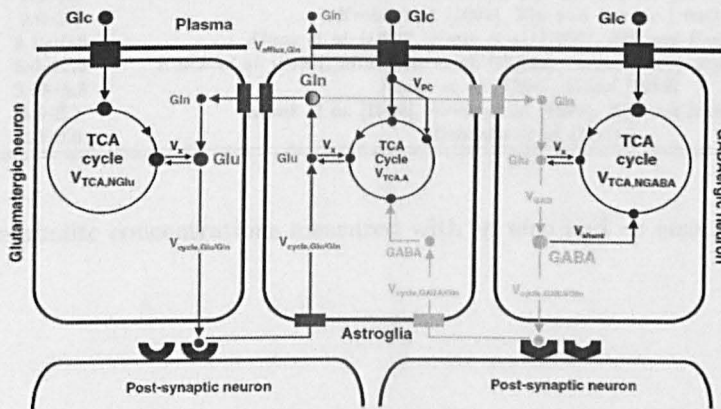
Figure 2.17: From *Graaf and Rothman* [2001]. Four-compartment metabolic model comprising the blood/plasma, glutamatergic neurons, GABAergic neurons and astroglia. Glucose enters the brain with the aid of glucose transporter in the bloodÜbrain barrier. In the glycolytic pathway, glucose is broken down into two pyruvate molecules which enter the tricarboxylic acid (TCA) cycle. One of the TCA cycle intermediates, 2-oxoglutarate (2OG), is in rapid exchange with a large glutamate pool that can be observed with NMR. The TCA cycle flux can be obtained from the glutamate turnover and is denoted VTCA. Due to compartmental localization of specific enzymes, the fate of glutamate differs in each of the three cellular compartments. In glutamatergic neurons, glutamate acts as an excitatory neurotransmitter and is released into the synaptic cleft in response to an action potential. Following interaction with post-synaptic receptors, the glutamate is taken up by the astroglia and converted to glutamine. Glutamine is ultimately transported back to the glutamatergic neuron, where it is converted to glutamate, thereby completing the so-called glutamate-glutamine neurotransmitter cycle. The flux through this cycle, Vcycle,Glu/Gln, can be obtained by following the glutamine turnover. In the GABAergic neuron, the glutamate is first converted to GABA which is the primary inhibitory neurotransmitter. Similar to the glutamatergic neuron, a GABA-glutamine neurotransmitter cycle exists between GABAergic neurons and astroglia. A metabolic pathway specific to astroglia is the carboxylation of pyruvate catalyzed by the astroglia-specific enzyme pyruvate carboxylase (PC). Note that the letter size roughly corresponds to the metabolic pool size of the corresponding metabolite (e.g. a large glutamine pool resides in astroglia).

Metabolite	Concentration (mM)	References
NAA	7.9–16.6	*Klunk et al.* [1996], *Kreis et al.* [1997]
GABA	1.3–1.9	*Klunk et al.* [1996], *Zijl and Barker* [1997]
Cho (total)	0.9–2.5	*Kreis et al.* [1997], *Zijl and Barker* [1997]
Cre (total)	5.1–10.6	*Klunk et al.* [1996], *Kreis et al.* [1997], *Zijl and Barker* [1997]
Glu	6.0–12.5	*Klunk et al.* [1996], *Michaelis et al.* [1993b], *Siegel* [1989], *Zijl and Barker* [1997]
Gln	3.05–5.8	*Klunk et al.* [1996], *Siegel* [1989]
Myo-inositol	3.8–8.1	*Klunk et al.* [1996], *Kreis et al.* [1997], *Zijl and Barker* [1997]
Scyllo-inositol	0.3–0.6	*Michaelis et al.* [1993a]

Table 2.1: Metabolite concentrations measured with *in vivo* and *ex vivo* 1H MRS in the human brain.
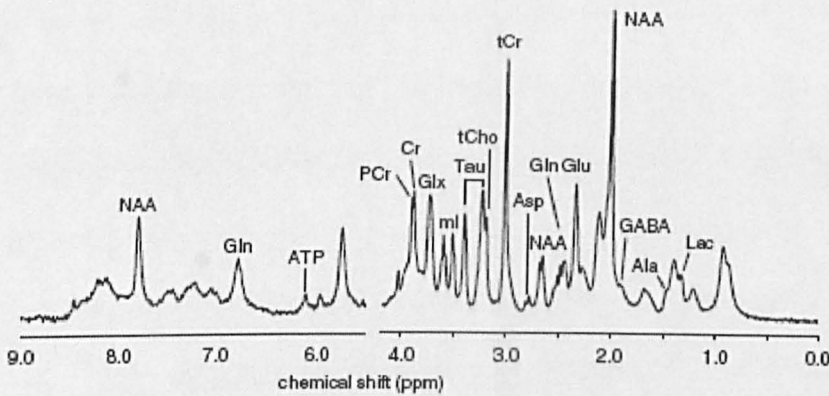
Figure 2.18: From *R. A. De Graaf* [2007]. Proton NMR spectrum obtained from rat brain in vivo at 11.75 T (TR/TE = 4000/12 ms).

Part II

MRS applications in Schizophrenia

3

Reproducibility of neurotransmitter pool estimates

using optimised MRS protocols on a clinical scanner

operating at 3.0 Tesla

3.1 Introduction

Several 1H-MRS acquisition schemes have been proposed and a special interest was dedicated to implement editing sequences and to optimize timing parameters either to accurately resolve overlapped metabolites or to quantify metabolites otherwise obscured by highly concentrated compounds. In fact, some studies showed how particular TE values are optimal to suppress some overlapping peaks and to simplify the quantification of metabolites of interest. More refined techniques tried to optimize the TE_1 and TE_2 ($TE/2 = TE_1 + TE_2$) since different j-coupling modulation occurs by varying the two terms and keeping the echo time fixed as it has been showed for citrate (*Gambarota et al.* [2005]).

Furthermore, even if j-editing methods were proved to be able to provide a reliable quantification, there is still lack of studies demonstrating a real improvement in reliabil-

ity over standard 1H-MRS for the *in vivo* measurement of Glu, Gln, GABA, and other metabolites. Secondly, difficulties of implementation reduce their use for clinical purposes. This study aims to compare the reliability of conventional and timing-optimized sequences for the detection and measurement of most of the visible metabolites and, in particular, for Glu, Gln and GABA. The reliability is assessed by computing two parameters: test-retest reproducibility coefficients of variation (CV) that provide an estimate of measurement stability and CRLB values (Cramer Rao Lower Bound) for the fitting quality estimate. The test-retest goal is also to determine the best sequence capable of detecting and robustly quantifying both neurotransmitters, such as Glu and GABA, and a metabolite which is biochemically linked to them, Gln. A particular interest is given in testing whether the sequences are able to quantify and then to provide concentrations for a wide range of metabolites.

3.2 Methods

The study was approved by the local Medical School Ethics committee and 14 healthy volunteers were recruited. All volunteers gave written informed consent. The MRI protocol consisted of a structural imaging MPRAGE and 7 spectroscopy sequences:

- PRESS TE=80ms (**P80**)(*Schubert et al.* [2004]);

- PRESS TE=40ms (**P40**)(*Mullins et al.* [2008]);

- PRESS TE_1=30ms, TE_2=85ms (**P115**)(*Snyder J* [2009]);

- PRESS TE_1=90ms, TE_2=18ms (**P108**)(*"ISMRM abstract:" 4283* [2009]);

- STEAM sequence TE=14ms, TM=8ms (**S14(128)**), 128 averages;

- STEAM sequence TE=14ms, TM=8ms (**S14(256)**), 256 averages;

- STEAM TE=72ms, TM=8ms (**S72**)(*Yang et al.* [2008]).

A 3T Philips Achieva scanner (software release 2.5.3) equipped with 8 channel sense coil was used and each subject underwent two different sessions separated by 10 minutes. In order to shorten the acquisition on each subject a single spectrum per sequence was acquired. In order to reproduce the variability due to subject repositioning, subjects were taken out the scanner between the sessions. A 25x25x25 mm^3 voxel was positioned in the prefrontal cortex (see figure 3.1) and the same values of TR=3000ms and of NA=128 were set up for all sequences. Due to smaller SNR compared to PRESS, which has total acquisition time of 6 minutes, one of the STEAM sequences (**S14(256)**) was acquired with 256 averages in order to exclude any possible SNR-dependent bias. All spectra were analyzed with LCModel and every basis-dataset was simulated with Spinevolution software version 3.3.3 (*Veshtort and Griffin* [2006]). The test-retest reproducibility was defined by coefficients of variation (CV): they were expressed as the absolute difference in concentration between scan 1 and scan 2 divided by their average concentration for each metabolite. For each metabolite, the computed CVs per sequence were statistically tested to check whether the differences in the CVs' mean values among sequences were also statistically significant. The T-test was performed by using the Matlab statistic toolbox.
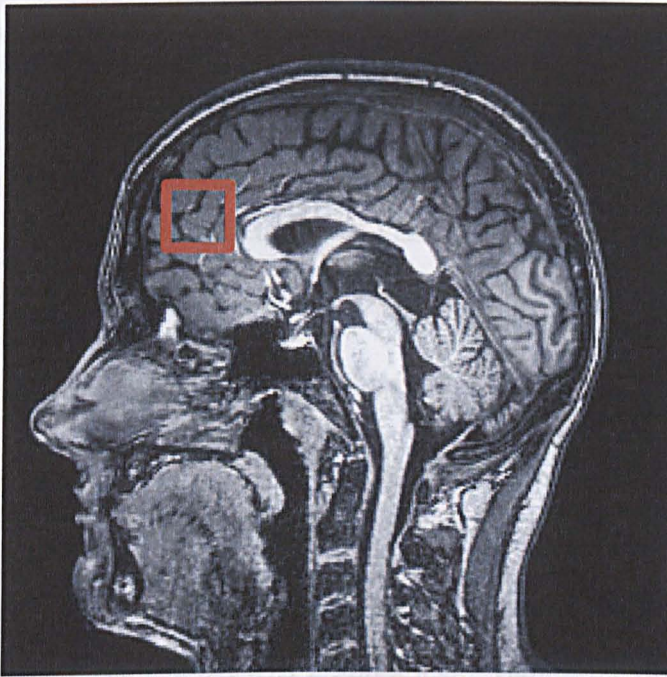
Figure 3.1: Voxel localization in the prefrontal cortex of healthy volunteers.

3.3 Results

Most of the data showed good fitting for the main metabolites and a narrow linewidth

equal to 0.02 ppm. The values for CRLB and CV a selection of the metabolites of

interest are shown in the table 3.3. The STEAM protocols usually performed more poorly

compared to the PRESS protocols even though the myo-Inositol quantifications obtained

a more reliable quantification in the case of STEAM. There was a significant difference

between all the PRESS sequences and the short TE STEAM with 128 averages but no

statistical improvements among the STEAM sequences. Not surprisingly the STEAM

TE=72ms did not perform well for any metabolites, most likely caused by the long TE

where part of the signal is lost. Conversely, the Glu was fitted and quantified better

with longer TE but the P80 revealed a more valuable quantification also for the Gln.

Table 3.1: Mean value of fisher correlation coefficients between Glutamate and Glutamine quantifications for all sequences in healthy volunteers.

Sequence	P115	P80	P40	P108	S14(128)	S14(256)	S72
Glu-Gln corr	0.019	0.036	-0.063	0.1	0.045	0.048	-

No evident difference was observed in the PRESS protocols when a statistic test was applied to the Glu and NAA CVs. From figure 3.3 it is possible to calculate the mean value among all sequences for the coefficients of variation for Glu equal to (mean±SD) 10±3, **S72** has been excluded because it is unreliable. It can also be seen that Gln has the minimum value, (mean±SD) 12±9, corresponding to **P80**. In fact, as shown in figure 3.2, the Gln CVs showed also a statistically significant difference among the different sequences (**P115-P80**: $p<0.004$; **P40-P80**: $p<0.03$; **P108-P80**: $p<0.01$). In general, **P80** has shown a robust detection and accurate reproducibility for a wide range of metabolites failing, in comparison to other sequences, for Ins and Asp. In addition Glu and Gln theoretical correlation coefficients were computed (see table 3.1); apart from the **P108** the correlations appeared to be quite low proving a sufficient distinction between the two metabolites. Interestingly, **P80** reported also a low correlation value (0.036).

(a) NAA (b) Ins (c) Glu (d) Asp (e) Gln (f) GPC+PCh
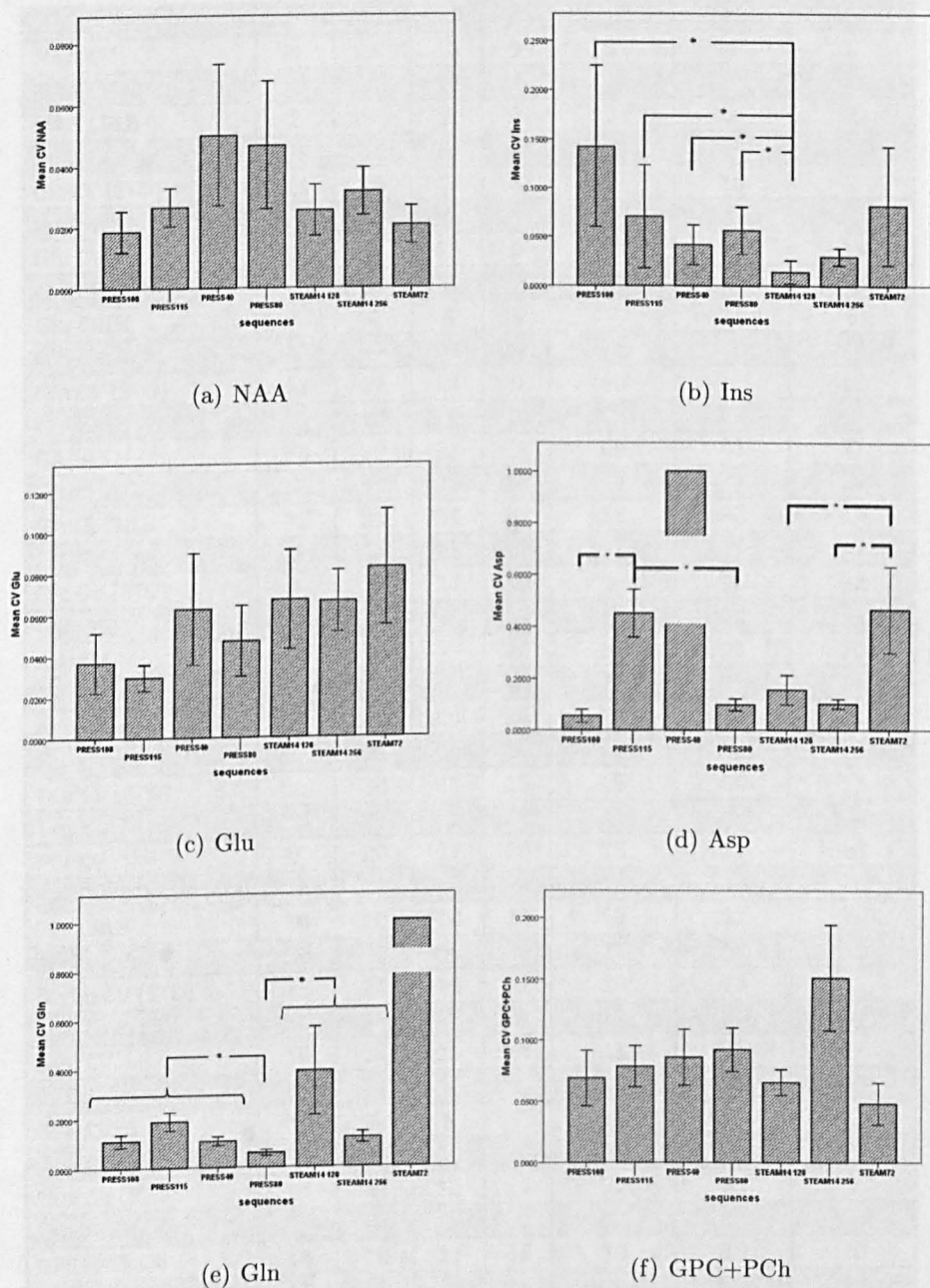
Figure 3.2: (Mean ± SD) Test-retest stability in healthy volunteers (prefrontal cortex) coefficients of variation (CV) for major metabolites and for all sequences under investigation. The significant differences with $p<0.05$ are indicated with an asterisk. The CVs are computed as the absolute value of $2 \times \frac{C_1-C_2}{C_1+C_2}$ where the C_1 and C_2 are concentration estimates from the respective measurements. See text for details.

Sequences	P108	P115	P40	P80	S14_128	S72	S14_256
NAA CV	4	5	10	9	5	4	6
NAA CV (STD)	3	5	17	16	4	3	4
NAA CRLB	2	1	2	2	2	2	2
Ins CV	28	14	8	11	3	16	6
Ins CV (STD)	13	18	7	8	2	10	2
Ins CRLB	15	6	5	6	4	6	3
Glu CV	7	6	13	9	13	17	13
Glu CV (STD)	7	5	20	13	11	13	9
Glu CRLB	5	4	6	5	7	11	6
Gln CV	22	37	21	12	78		24
Gln CV (STD)	11	27	14	9	80		13
Gln CRLB	14	20	19	14	122	788	17
GABA CV	63	29	31	28	68	41	32
GABA CV (STD)	60	17	25	30	44	31	27
GABA CRLB	75	21	34	25	38	33	29
Cre CV	6	17	15	12	19	15	27
Cre CV (STD)	4	9	17	10	8	4	22
Cre CRLB	9	10	8	10	11	10	11
Asp CV	11	90		20	31	93	20
Asp CV (STD)	11	69		18	26	75	11
Asp CRLB	13	168	936	14	23	43	21
Tau CV		35	27	16	22	113	23
Tau CV (STD)		30	28	15	18	84	18
Tau CRLB	390	26	21	24	14	244	14
PCr CV	7	20	17	20	16	19	28
PCr CV (STD)	5	15	12	25	15	15	22
PCr CRLB	10	10	10	10	12	12	9
Scyllo CV	30	34	19	36	16	39	29
Scyllo CV (STD)	26	24	15	32	10	23	31
Scyllo CRLB	30	28	18	27	18	26	20
GPC CV	16	14	16	14	11	9	27
GPC CV (STD)	11	14	11	9	10	7	19
GPC CRLB	8	5	8	7	15	7	11
Gua CV	19	35	10	16	64	53	23
Gua CV (STD)	14	39	12	15	77	83	7
Gua CRLB	18	23	9	10	111	122	12
GPC+PCh CV	14	16	17	18	13	10	30
GPC+PCh CV (STD)	10	13	17	13	5	8	25
GPC+PCh CRLB	11	7	10	9	14	7	12

Figure 3.3: Test-retest stability in healthy volunteers' spectra from prefrontal cortex. Mean±SD coefficients of variation (CV) and Cramer-Rao-Lower-Bounds (CRLB) are given for major metabolites and for all sequences under investigation. CV $(\%) = 2 \times 100 \times \frac{C_1 - C_2}{C_1 + C_2}$ where the C_1 and C_2 are concentration estimates of each measurements. See text for details.

3.4   Discussion

The present comparative study shows that Glu, Gln can be reliably measured on pre-frontal cortex and that can be achieved with no sophisticated editing technique. However, there is an important limitation of the values reported in this study to be considered: when different brain areas are investigated there could be a poor shimming performance leading to an increase in CRLBs and CVs. Also, even though it is not evident from our data, the sequences with longer TE would be quantified with a stronger T_2 decay which is not easily eliminable. Despite that, **P80** can be considered a good compromise if interests are focused on variations caused by disease rather than absolute values. Given the fact that different sequences are resulted specific only for some metabolites and not reliable for others, in the case of not too stringent experiment time restrictions, the use of two sequences could cover a wider range of detected compounds and give enhanced results. Furthermore, the increment of number of averages in **S14(256)** did not prove to have any benefit compared to the **S14(128)**, probably caused by the disadvantage of frequency shift occurring when longer acquisition time is exploited. Signal-to-noise ratio might get a further improvement by fragmenting the acquisition in dynamic mode and by acquiring 8 spectra of 16 averages each. Even though no realigning was performed (see appendix A) on those data, a gain in terms of SNR would have come from the B_0 drift correction. Furthermore, it is also of particular importance to put in a context the reported Glu and Gln theoretical correlation coefficients: those values need to be related to how correct the quantification reproduced the concentrations: underestimation of glutamine levels would produce low correlation coefficients which are not necessarily a

strong metabolite separation. Importantly, our CVs were also smaller than the CRLBs

values and that seems to be not in accordance with estimators' theory. In fact, CRLBs

are indeed the lower bound on the variance of estimators of a parameter and any un-

biased[1] estimator should not be smaller than CRLBs. It is possible to prove that the

variance used[2] is a biased[3] estimator thus proving the fluctuations of the CVs. Having

said that, no direct prediction of CVs can be deducted from the CRLBs.

As a rule of thumb we can generally accept that CRLB values $\leq 10\%$ predict CV

values smaller than 20% and hence the correspondent quantification is acceptable and

accurate. On the contrary, for CRLB values $\geq 10\%$ no conclusions can be drawn. How-

ever, the discrepancy found between CRLBs and CVs is likely to be also associated to

uncertainty due to subject repositioning. In fact, in this case there is a larger variability

which cannot be predicted by a mathematical model. Excluding that further uncertainty

might make CRLBs more associated to the real CVs.

---

[1]An estimator is said to be unbiased if the difference between this estimator's expected value and the true value of the parameter being estimated is equal to zero for all values of the parameter.

[2]Given independent and identically distributed random variables $\lambda_1, ..., \lambda_n$ having expectation value μ and variance σ^2. We have been using mean defined as $\overline{\lambda} = \frac{1}{n}\sum_{i=1}^{n}\lambda_i$ and variance defined as $S^2 = \frac{1}{n}\sum_{i=1}^{n}(\lambda_i - \overline{\lambda}^2)$

[3]The bias can be proved by:

$$(3.1) \qquad \mathrm{E}[S^2] = \mathrm{E}\left[\frac{1}{n}\sum_{i=1}^{n}(\lambda_i - \overline{\lambda})^2\right] = \mathrm{E}\left[\frac{1}{n}\sum_{i=1}^{n}\left((\lambda_i - \mu) - (\overline{\lambda} - \mu)\right)^2\right]$$

$$(3.2) \qquad = \mathrm{E}\left[\frac{1}{n}\sum_{i=1}^{n}(\lambda_i - \mu)^2 - 2(\overline{\lambda} - \mu)\frac{1}{n}\sum_{i=1}^{n}(\lambda_i - \mu) + (\overline{\lambda} - \mu)^2\right]$$

$$(3.3) \qquad = \mathrm{E}\left[\frac{1}{n}\sum_{i=1}^{n}(\lambda_i - \mu)^2 - (\overline{\lambda} - \mu)^2\right] = \sigma^2 - \mathrm{E}\left[(\overline{\lambda} - \mu)^2\right] < \sigma^2$$

It can be proved that an unbiased estimator variance is instead: $S^2 = \frac{1}{n-1}\sum_{i=1}^{n}(\lambda_i - \overline{\lambda}^2)$

3.5   Conclusions

The PRESS TE=80ms was considered a good compromise for detection of Glu and Gln as well as other major metabolites. A big limitation of the sequence is due to the fact that GABA was not reliably quantified so that an optimization needs to be done to determine a sequence capable of measuring GABA concentration. The **P80** reliability described in this chapter refers to healthy volunteers and to reasonably large voxel so that we may expect a reduced performance of the sequence in the case of patients and of smaller voxel size.

4

Oscillatory brain activity and metabolic profile in schizophrenia investigated by proton MRS and EEG

4.1 Introduction

Schizophrenia is a severe mental disorder that affects about 1% of the population in the world (*Chang et al.* [2007]). The aetiology of schizophrenia is not entirely understood, but the disease involves abnormal dopamine and Glu transmission and, in particular, several lines of evidence point to a crucial role of hypofunction of NMDA receptors and resulting prefrontal glutamatergic dysfunction and neurotoxicity (*Rüsch et al.* [2008]). Numerous studies about glutamatergic model of schizophrenia (*Olney et al.* [1999], *Farber et al.* [2002], *Olney and Farber* [1995]) established the so called glutamate hypothesis in schizophrenia.

According to the hypothesis of NMDA receptor hypofunction, this hypofunction causes decreased activity of inhibitory GABAergic interneurons (*Carlsson et al.* [2001], *Lewis and Moghaddam* [2006], *Homayoun and Moghaddam* [2007], *Coyle* [2006], *Coyle* [2004]), which leads in turn to the disinhibition of glutamatergic neurons projecting to the pre-

frontal cortex and consequently an increase in Glu release (*Moghaddam et al.* [1997],
Moghaddam and Adams [1998]).

In vivo 1H MRS has been widely used to study schizophrenia as it is able to look into
alterations of metabolites that may result from NMDA hypofunction. Indeed, over the
last two decades, a number of 1H MRS studies have been performed as a consequence
of this hypothesis in order to research possible alterations of Glu levels in schizophrenia.
Findings to date are highly controversial and do not allow to conclude whether differences
between studies are due to technical challenges in estimating Glu levels or to effects from
disease heterogeneity, duration or medication. The anterior cingulate is surely a region
where dysfunctions in schizophrenia have constantly been found and where several studies
focused attention on. Different field strengths have been used, but this review will focus
on those $\geq$ 3T to avoid confounds emerging from less reliable MRS reporting Glu/Gln
rather than their separate quantification. Table 4.1 summarises the main studies at field
strength $\geq$ 3T reporting Glu and Gln changes in schizophrenia.

No evidence of changes was found in Glutamate+Glutamine (Glx) (*Wood et al.* [2007])
in the right and left dorsal and rostral cingulated of 15 male schizophrenia patients when
compared with 14 controls. A 9% NAA reductions was detected.

Théberge and colleagues conducted several studies at 4 T field strength with voxel size
of 1.5 cm^3. In their first study (*Théberge et al.* [2002]) of 21 young never treated patients
with schizophrenia (illness duration approximately 1.7 years) and 21 healthy volunteers,
the patients presented an elevated Gln with normal Glu and NAA in both the left an-
terior cingulate and left anterior thalamus. This work, similarly to what a very first Glu

study had found (*Bartha et al.* [1997]), suggests an increased glutamatergic neurotrans-

mission[1] early in the illness, which is not attributable to either effects of medication or

chronicity. The same group then studied 21 patients with chronic schizophrenia (illness

duration approximately 15.6 years) and 21 controls (*Théberge et al.* [2003]). Glu and Gln

were decreased in the anterior cingulate, but the left thalamus Gln was increased. They

concluded that in the Anterior Cingulate Cortex (ACC) of chronic patients decreased

levels of Glu and Gln could be related to neurodegeneration or to the effects of chronic

medication. On the contrary, increased glutamatergic turnover persisted in the thalamus

while the glutamatergic system gets reduced earlier in the cingulate, suggesting disease

progression or antipsychotic medication effects. The same group carried out a longitudi-

nal study in 2007 (*Théberge et al.* [2007]) in which they focused attention on Glu, Gln and

gray matter volume in the left anterior cingulate and thalamus of 16 patients with first-

episode schizophrenia at baseline. After that, two different scan sessions took place: after

10 and 30 months of antipsychotic treatment. 16 healthy participants underwent MRI

on two occasions 30 months apart. The study reported higher Gln levels in the ACC and

thalamus of never-treated patients, consistent with their first study (12 out of 16 subjects

overlapped with the cohort of their 2002 study). After 30 months, the anterior cingulate

Gln level were consistently increased, which is in contrast with what they showed in their

2003 study on patients with longer duration of illness. The reduction in the thalamus Gln

level was significant after 30 months, but that decrease did not drop below the healthy

---

[1]The association of Gln changes to glutamatergic neurotransmission is due to the well known hy-
pothesis that in glutamatergic neurons, Glu acts as an excitatory neurotransmitter and is released into
the synaptic space in response to an action potential. Following the interaction with the post-synaptic
receptors, the Glu is taken up by the astroglia and converted to Gln.

control level; parietal and temporal lobe gray-matter loss was correlated with thalamic Gln loss. No significant changes were observed in Glu and Gln over 30 months in the healthy group. They speculated that elevated Gln in never-treated patients with a subsequent decrease in thalamic Gln and gray-matter loss in connected regions could indicate either neurodegeneration or a plastic response to reduced subcortical activity.

Furthermore, increased Glu and Gln levels were reported both in the dorsolateral prefrontal cortex and in hippocampus among subjects with chronic schizophrenia (*van Elst et al.* [2005b]). No significant correlation between duration illness duration and Glu concentrations was reported.

Recent studies have looked at the possibility of using Glu/Gln MRS measures as potential schizophrenia endophenotypic markers. A comparison between 20 adolescents having a parent with history of schizophrenia and a group of 22 adolescents with no parents with a history of illness (*Tibbo et al.* [2004]) was made to assess difference between high and low genetic risk of schizophrenia. They found significantly higher Glx in the right medial frontal lobe of the high-risk group and this finding was considered in favour of a neurodevelopmental hypotheses for schizophrenia.

In addition, among the psychological measures with endophenotypic relevance, the Continuous Performance Test (CPT) (*BECK et al.* [1956]) has received the most interest. Poor performance is often seen in people with schizophrenia on the CPT. In this test there is a rapid presentation of visual stimuli to the subject who in turn needs to identify target items among foils. In particular, CPT measures sustained attention and has been extensively studied as a cognitive endophenotype. The NMDA antagonist ketamine

impairs performance on CPT in healthy individuals (*Umbricht et al.* [2000]).

Purdon et al. reported a study on 15 adult siblings of individuals with schizophrenia (high genetic risk group) and 14 healthy volunteers (*Purdon et al.* [2008]). They found that higher levels of Glu and Glx resulted to be associated to the lower score from CPT even if not statistically significant (r = 0.32; p = 0.096).

Two studies from Rusch and Olbrich group have also shown a consistent increase in the glutamatergic pool. Left dorsolateral prefrontal cortex but not hippocampal Glu and Gln levels have been found increased in 29 patients compared to 31 healthy volunteers (*Rüsch et al.* [2008]). Executive functioning was also assessed by the Wisconsin Card Sorting Test (WCST) and its poor performance was associated with increased hippocampal Glu concentrations among subjects with schizophrenia, but not among healthy controls. Significantly higher Glu concentration in the prefrontal cortex and near-significantly higher Glu concentration in the hippocampus were detected in 9 patients with first episode schizophrenia when compared to 32 healthy controls (*Olbrich et al.* [2008]).

Lower Glu levels were observed on mesial prefrontal grey matter when looking at changes even caused by genetic factor rather than by disease only (*Lutkenhoff et al.* [2010]). 14 discordant twins for schizophrenia and 1 unaffected co-twin presented significant lower values in Glu compared to the healthy pairs. According to the authors' speculation, the fact that almost the same abnormalities were present in the twin pairs discordant for schizophrenia might lead to identify a trait marker of the schizophrenia risk. That risk marker could become state marker of schizophrenia when it is exacerbated. More recently the debate continued both by proving a reduction of Glu concentrations in

schizophrenia (*Tayoshi et al.* [2009]) and by showing that rather than single Gln and Glu

concentration, only their ratio exhibits a significant reduction (*Shirayama et al.* [2010]).

On the other hand, another large body of research is focusing attention on oscillatory

activity of the brain, and in particular on the theta activity which occurs in the frequen-

cy range of approximately 4-8 Hz. Even though the theta oscillations are particularly

prominent in the hippocampus of mammals, other sources of theta oscillations can be in

regions such as ento- and perirhinal cortex, the prefrontal, somatosensory and visual cor-

tex (*Raghavachari et al.* [2006], *Tsujimoto et al.* [2006]). Accordingly, theta oscillations

are involved in memory-related processes: significant increases in theta power during

encoding of information predict subsequent recall of that information (*Sederberg et al.*

[2003]); the theta component over midline frontal regions is enhanced in tasks involving

both working memory and focused attention (*Gundel and Wilson* [1992], *Gevins et al.*

[1997]).

Controls	Patients	Disease time	fit quality	Glu	Gln	Gln/Glu	location	field strength	Ref.
21	21	21±24	<75% †	no ±11%	↑ ±24%	-	L. ACC	4T	*Théberge et al.* [2002]
21	21	188±107	<75% †	↓ ±11	↓ ±24%	-	L. ACC	4T	*Théberge et al.* [2003]
16	16	<10	<75% †	no ±11	↑ ±24%	-	L. ACC	4T	*Théberge et al.* [2007]
16	16	<10	<75% †	no ±11	↑ ±24%	-	Thal.	4T	*Théberge et al.* [2007]
16 1	16 ·	<10	<75% †	no ±11	↓ ±24%	-	Thal.	4T	*Théberge et al.* [2007]
14	10	30.8±43.6	<30% † ‡	no ±4%	no±5%	↑	ACC	4T	*Bustillo et al.* [2010]
18	19	87.6±66	<25% † ‡	no ±-%	no±-%	↑	MPC	3T	*Shirayama et al.* [2010]
31	29	52.9±47.1	<20%	↑ ±-%	↑±-%	-	DLPC	3T	*Rüsch et al.* [2008]
25	30	123.6±104.4	-% † ‡	↓ ±-%	no±-%	-	ACC	3T	*Tayoshi et al.* [2009]
14	15	-±-	<25% ratio	no ±15%	-±-%	-	ACC	3T	*Purdon et al.* [2008]
32	21	63.8±9.4	-% † ‡	↑ ±9%	↑±8%	-	DLPC	3T	*van Elst et al.* [2005a]
32	21	63.8±9.4	-% † ‡	↑ ±9%	-±8%	-	Hipp	3T	*van Elst et al.* [2005a]

Table 4.1: Summary of studies at field strength > 3T reporting Glu and Gln changes in schizophrenia. Fit Quality indicates the quality control criteria used in the study. †: water reference corrected by segmentation; 1: patients after 30 months of medication; ‡: CSF correction applied:

Thereafter, the involvement of theta activity in cognitive and working memory-related processes suggests the possibility of its abnormal activity in schizophrenia where impairments of all these domains can occur. Indeed, abnormal evoked theta activity during working memory and cognitive control was revealed in a study with 10 patients and 10 controls (*Schmiedt et al.* [2005]): while in controls theta activity was particularly prominent over frontal electrodes in the high cognitive control condition, in patients with schizophrenia there was a difficulty to maintain a high cognitive control condition and also no increase in evoked theta activity was observed. The well recognized attention deficits present in schizophrenia has also been related to the induced theta reduction in a go/no-go task suggesting that low-frequency oscillations are not coordinated effectively in schizophrenia during various information processing tasks (*Bates et al.* [2009]). Thus, such finding might open a route to a more complex characterization of variations of the neurotransmitters' pools and help to understand those variations in light of the current hypothesis of NMDA hypofunction.

Recently, a positive relationship between hippocampal Glu and theta was established in healthy volunteers (*Gallinat et al.* [2006]). This evidence might suggest glutamatergic activity as modulator of oscillatory theta activity. Here, we used a dedicated MRS protocol to investigate whether alterations of limbic Glu levels occur in patients with early schizophrenia. Secondly, in parallel acquisition of EEG data were used to study the interrelation between Glu and theta activity in schizophrenia to investigate whether the interrelation seen between hippocampus Glu and theta activity is also visible in the Anterior Cingulate Cortex (ACC) and whether that might be altered by NMDA dys-

function. Our investigation focused also on the idea that the decreased NAA levels in schizophrenia are not attributable to neuron loss but can be interpreted as an early effect of glutamatergic imbalance. Hence, we also aimed to assess interdependencies between prefrontal NAA levels and the disease duration in early stage schizophrenic patients. In addition, we aimed to evaluate the further interrelation present between NAA levels and Event Related Potentials (ERP) such as P300 and N100 that are well known to be altered in schizophrenia (*Bramon et al.* [2004], *Gallinat et al.* [2002], *Horacek et al.* [2006], *O'Donnell et al.* [1995a,b, 2004]).

4.2 Materials and Methods

[2] The use of human participants in this experiment was approved by the Nottingham Local Research Ethics Committee and the R&D department and in accordance with the Declaration of Helsinki. All participants provided informed consent. Twenty-seven male participants with paranoid subtype of schizophrenia (one left-handed, mean age±SD 23.36±4.4 years) were recruited from patients within the Nottinghamshire Healthcare NHS Trust. Schizophrenia was diagnosed on the basis of a clinical interview, reference to case files, and a clinical consensus diagnostic meeting of research psychiatrists according to the criteria in the Diagnostic and Statistical Manual of Mental Disorders (DSM-IV; American Psychiatric Association, 2000). Patients with a serious neurological disorder, current state of intoxication with substances or current or past substance dependence,

---

[2]The study was performed in collaboration with prof. Liddle's team. The ethics application was written by Dr. Amritash Rai. The recruitment was made by Dr. Pavan Mallikarjun and Dr. Lena Palaniyappan. The EEG data were acquired and analyzed by Dr. Kathrin Doege

another current ICD-10 mental illness diagnosis, personality disorder, or serious visual or auditory impairments were excluded from the study. The maximum illness duration was 5 years. In order to assess the severity of symptoms and the degree of dysfunction, the Signs and Symptoms of Psychotic Illness interview (SSPI; *Liddle et al.* [2002]) was performed and the Global Assessment Functioning (GAF) score from DSM-IV was obtained. A mean total SSPI score of 12.9 (SD = 5.6) indicated that patients were partly remitted with only residual symptoms. The mean GAF score was 56.8 (SD = 12.6), which denotes mild symptoms or some social or occupational impairments, but generally good functioning. All patients were receiving treatment with atypical antipsychotic medication [nine olanzapine (5–20 mg per day), four risperidone (1.5-4 mg per day), three clozapine (300–375 mg per day), one aripiprazole (10 mg per day)].

Twenty-three age-matched healthy males (mean age±SD 28.8±5.4) were recruited as controls. Subjects with a history of psychiatric illness in first degree relatives, serious neurological disorder, or visual or auditory impairments were excluded from the study. The two groups were matched for parental occupational status, determined with the National Socio-Economic Classification (NS-EC). EEG was recorded in all subjects prior to the MRI session. Only 21 patients and 20 controls accepted to undergo to an MRI scan after EEG.

4.2.1   MRS acquisition and analysis

[3] A 3T Philips Achieva scanner equipped with a 8 channels SENSE coil was used and the protocol included sagittal MPRAGE and two single voxel spectra optimized for Glu detection: PRESS TE =80 ms (*Schubert et al.* [2004]) (TR=2000ms, 128 averages) localized on the anterior cingulate cortex (ACC) (voxel size = 30x15x15 mm^3) and on left hippocampus (voxel size = 35x15x15 mm^3), see figure 4.1. Second order pencil beam shimming method on a manually selected volume of interest and water suppression by excitation prior to each acquisition were applied as implemented on the Philips platform. Sagittal image reconstruction in both orthogonal planes was used to better localize the spectroscopy voxel. Metabolite concentrations were estimated using linear combination model (LCModel) (*Provencher* [1993, 2001]). A tailored basis-dataset was used and water signal served as internal standard for absolute quantification. The reliability of metabolite quantification was judged by the standard deviation of the fitting expressed as percentage of estimated concentration (CRLB). Our criterion for accuracy of spectral fitting was CRLB<20%. For the correction of the voxel's tissue composition, segmentation of MPRAGE images was performed using SPM and an in-house Matlab software was used to create spectroscopy VOI masks. More details about the software can be found in appendix B. The gray matter (GM), white matter (WM) and cerebrospinal fluid (CSF) contents of each MRS voxel were determined. Two different corrections were applied: water content correction (S_{water}) and CSF correction (S_{CSF}). The two corrections were based on two different VOIs, for water and for NAA, as it results from the chemical

---

[3]The MR data were entirely acquired by myself after being trained as competent MR operator.

shift displacement effect heavily occurring in the PRESS sequence. The displacement was computed according to the values of the three gradients and the voxel size in the three directions. The water content was computed from the water VOI according to the standard concentrations in the various tissues[4] ($C_{wc} \sim 0.82$ for gray matter, ~ 0.73 for white matter, > 0.98 for CSF). According to *McLean et al.* [2000] it is correct to assume that the metabolite concentrations in CSF are close to 0 in order to correct for partial volume effects due to CSF and to provide metabolite levels per volume of brain tissue. This correction has been computed on the basis of the NAA VOI for all metabolites and the white and grey matter fraction was used to scale the concentrations. However, all concentrations have been considered as measured in arbitrary units as no relaxation effect was corrected.

4.2.2 EEG acquisition and analysis

[5] The experiments were both conducted in quiet location in the Psychiatry Department of University of Nottingham by research fellows in the division of Psychiatry. After placement of the electrodes, participants were seated in front of a computer monitor.

Two tasks were used during the EEG recording: the auditory oddball task and the go/no go task.

The auditory oddball task has been very frequently used over the last two decades to assess information processing in schizophrenia and we employed an auditory odd-

---

[4]The values are expressed as fraction of the pure water concentration: 55mM.

[5]This section was not attended by myself and so few details will be given as provided by Dr. Kathrin Doege (*Doege et al.* [2009]).
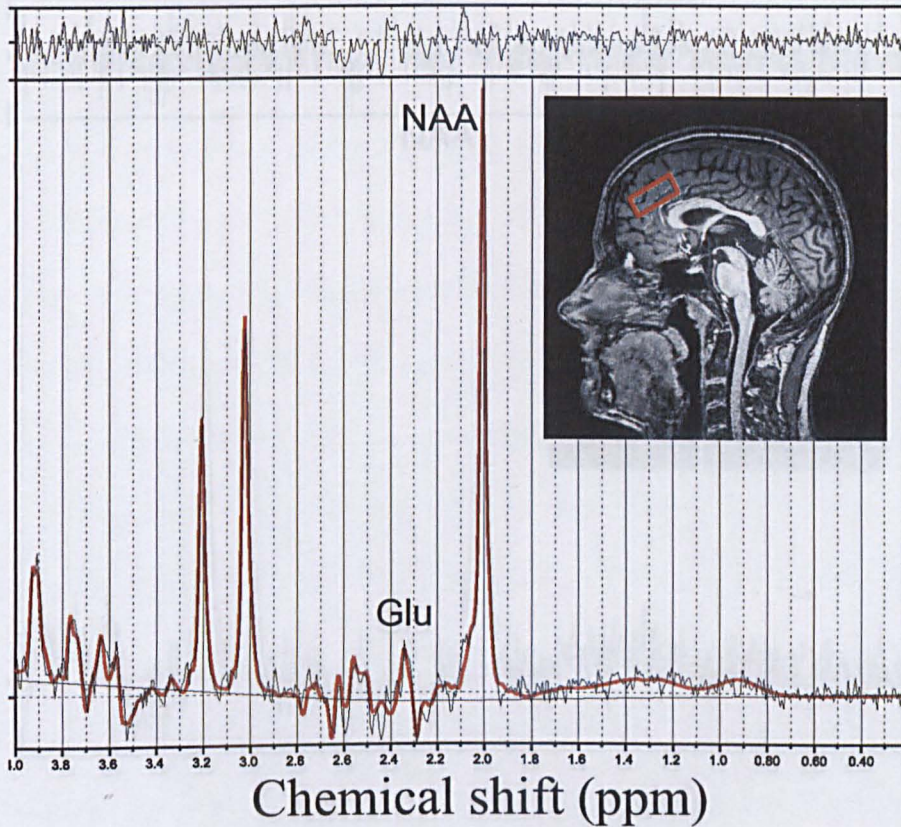
Figure 4.1: ^1H-MRS spectrum (PRESS: TR=2s, NSA=128, TE=80 ms, 2048 sampling points, voxel size $= 30 \times 15 \times 15 \ mm^3$) localized in the Anterior Cingulate Cortex (ACC). The major Glu and NAA peaks are displayed on the spectrum.

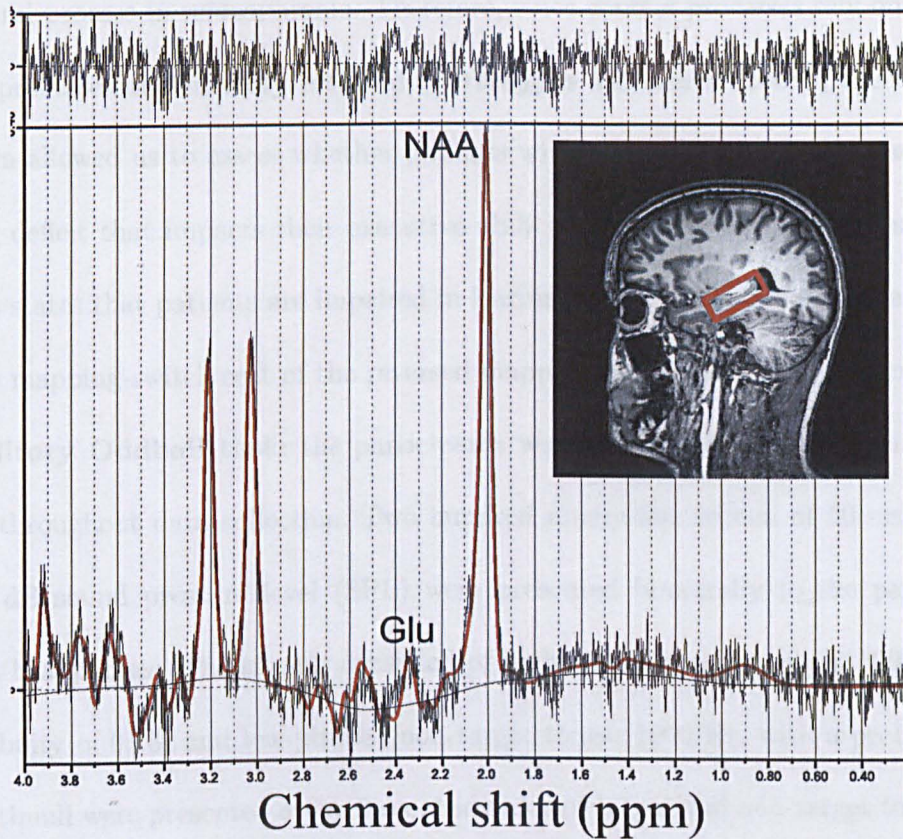**Figure 4.2:** ^1H-MRS spectrum (PRESS: TR=2s, NSA=128, TE=80 ms, 2048 sampling points, voxel size $= 35 \times 15 \times 15\ mm^3$) localized in the Hippocampus. The major Glu and NAA peaks are displayed on the spectrum.

ball task because it elicits activation of frontotemporal regions in healthy comparison subjects(*Opitz et al.* [2002]) and it requires top-down organization and integration of auditory information (*Opitz et al.* [2002]) and patients with schizophrenia exhibit impaired task-associated neural function (*van der Stelt et al.* [2004]). A deep interest were toward the control process in schizophrenia. Therefore, since control processes rely on both executive processes and memory retrieval (*Verbruggen and Logan* [2008]), the Go/NoGo paradigm allowed us to assess whether patients with schizophrenia show an associative learning deficit that impacts their executive ability to inhibit responses. A current hypothesis states that patients are impaired in learning the stimulus-stop associations and that the mapping-switch cost of the reversed mapping in the test phase is decreased.

Auditory Oddball task: the participants were instructed to fixate their gaze on a cross throughout data collection. Two hundred ninety-five stimuli of 50 ms duration and 80 dB sound pressure level (SPL) were presented binaurally to the participants through headphones. The stimuli consisted of highpitched target tones (1500 Hz, with a probability of 0.15) and low-pitched non-target tones (1000 Hz, with a probability of 0.85). Stimuli were presented every 2 sec, the order of target and non-target tones being randomized. Participants were required to respond to the targets with a button press on the keyboard with their right index finger as fast as possible. Prior to recording, the participants performed 30 practice trials.

Go/no-go task: the participants were instructed to fixate the computer monitor on which the stimuli were presented. Letter stimuli were presented to participants in white font against a black background. Participants were instructed to minimize blinking and

not to move during data acquisition periods, except for the finger movement required for the behavioural response marked on a computer keyboard. An unequal-probability go/no-go task was presented to the partecipants and they were instructed to press button with their right index finger as quickly and accurately as possible every time the white X (0.80 probability, 240 trials) appeared, and not to press it to the white K (0.20 probability, 60 trials). With the exception that two Ks were never presented sequentially, the order of both letters was random. Reaction time and accuracy were equally stressed. Stimuli were presented for 240 ms each, with a randomly varied stimulus onset asynchrony of 890, 1890, or 2890 ms. To ensure that instructions were understood, each participant performed a block of 10 practice trials twice before starting the proper experiment. Scalp potentials were recorded from 128 electrodes (Biosemi, Amsterdam, The Netherlands) distributed over the entire scalp according to the International Five Percent Electrode System for high resolution EEG (*Oostenveld and Praamstra* [2001]). Eye movements were recorded from a bipolar derivation consisting of one electrode placed to the right side of the right eye and another below the right eye. All other electrodes were referenced to the average electrical potential of the electrodes at the right and left mastoid processes. The EEG channels were amplified with a bandpass of 0.1 to 100 Hz, digitized on-line at a rate of 256 Hz, and recorded on computer hard disk. The cluster of analyzed electrodes included C21, C23, A1 and A19 which were all on the frontal midline. Evoked potentials were obtained for each participant by averaging the segmented data for targets and non-targets after subtracting pre-stimulus baseline activity within 200 ms before stimulus. N100 amplitude was measured by detecting peaks within 50-150 ms, P300 within 200-500

ms after stimulus.

Time-frequency analysis was performed by convolving the data with a complex Morlet wavelet w(t, f_0) having a Gaussian shape in time (σ_t) and frequency (σ_f) domain around the centre frequency f_0. A wavelet characterized by a constant ratio (f_0/σ_f)=3 was used. To analyze evoked activity, the segmented and baseline-corrected EEG data was averaged over target and non-target trials for each participant. Then, the wavelet transform was applied to the averaged data. For the theta frequency range, post stimulus peak values of wavelet coefficients within two different time windows corresponding to the N100 and the P300 time window: early evoked theta (0-150 ms) and late evoked theta (200-500 ms). To obtain induced activity, the wavelet transform was applied to the segmented, unaveraged EEG data, from which evoked activity had been removed by subtracting the average. Induced activity was determined as the percent change of wavelet coefficients in the theta band post stimulus relative to a prestimulus baseline (-300 ms to -200 ms) according to the work of *Pfurtscheller and da Silva* [1999]. In particular, the induced theta under consideration was only the one with correct withholdings to the occurrence of Ks.

4.2.3 Statistics

The MRS data were tested for normal distribution via Lilliefors test. An unpaired T-test was run on the data to assess significant differences; Pearson test was performed to test the significance of correlations. To this end the Matlab statistic toolbox was used.

4.3   Results

4.3.1   EEG results

The induced theta activity for go/no-go task was significantly reduced in patients vs controls (for electrode C21, mean±SD $theta_{patients}$=37.2±30.0 μV, $theta_{controls}$=79.4±34.0 μV, p<0.00015; for electrode C23, mean±SD, $theta_{patients}$=42.6±37.6 μV, $theta_{controls}$ = 91.3±32.9 μV, p<0.00015;)

The values for ERP, as expected, have been found reduced in patients versus control, (for P300 C21 p<0.019 and C23 p<0.014; for N100 C21 p<0.015 and C23 p<0.011). The mean values across patients and controls are displayed in figure 4.3.

4.3.2   MRS results

Most of the data showed a linewidth of 0.030 ppm and the fitting produced accurate quantification of all major metabolites (mean NAA CRLB<5% in ACC and <10% in hippocampus) including Glu (mean CRLB<12% in ACC and <18% in the hippocampus). Glu CRLBs exceeding our threshold value of 20% were excluded from statistics (for ACC only one control value was excluded whereas for the hippocampus 8 controls and 9 patients were excluded.). For Asp CRLBs the threshold values was 22% since few subjects had Asp CRLB value of 21%. The Aspartate values complying with such requirement were in total 9 for patients and 14 for controls. Only for the correlations, since one patient's EEG data were rejected, the computation was performed on 20 patients.

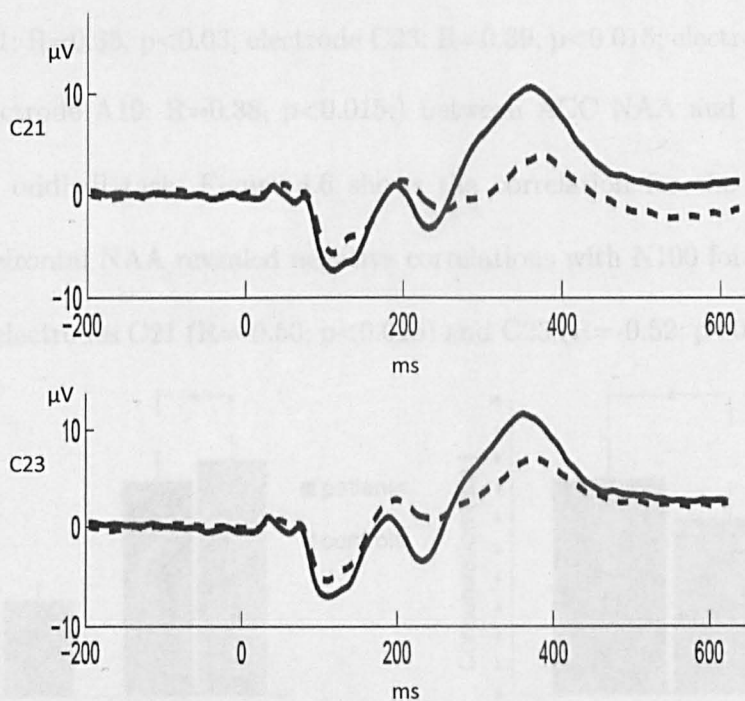**N-acetyl-aspartate**: NAA was significantly reduced in ACC in patients (mean

Figure 4.3: Courtesy of Dr. Kathrin Doege. Grand average of ERPs for controls (solid line) and patients (dashed line) for electrodes C21 and C23. The difference between patients and controls for N100 and P300 can be seen around 100 ms and 300 ms respectively (for P300 C21 p<0.019 and C23 p<0.014; for N100 C21 p<0.015 and C23 p<0.011).

$NAA_{patients} = 29.3 \pm 3.9$; mean $NAA_{controls} = 32.1 \pm 3.4$: 10% reduction, p<0.02), as shown

in figure 4.4(a). No hippocampus changes were detected. As shown in figure 4.5, disease

duration was also found to be strongly negatively correlated to the NAA levels in ACC

(R=-0.71, p<0.0007), whereas no correlation was seen in the hippocampus NAA levels.

Furthermore, a moderately positive correlation was observed on a subset of electrodes

(electrode A1: R=0.35, p<0.03; electrode C23: R=0.39, p<0.015; electrode C21: R=0.34,

p<0.032; electrode A19: R=0.38, p<0.015;) between ACC NAA and the amplitude of

P300 in the oddball task. Figure 4.6 shows the correlation for the A1 electrode. In

addition, prefrontal NAA revealed negative correlations with N100 for auditory oddball

task for the electrodes C21 (R=-0.50; p<0.025) and C23 (R=-0.52; p<0.020) (figure 4.7).

(a) NAA and Glu   (b) Aspartate
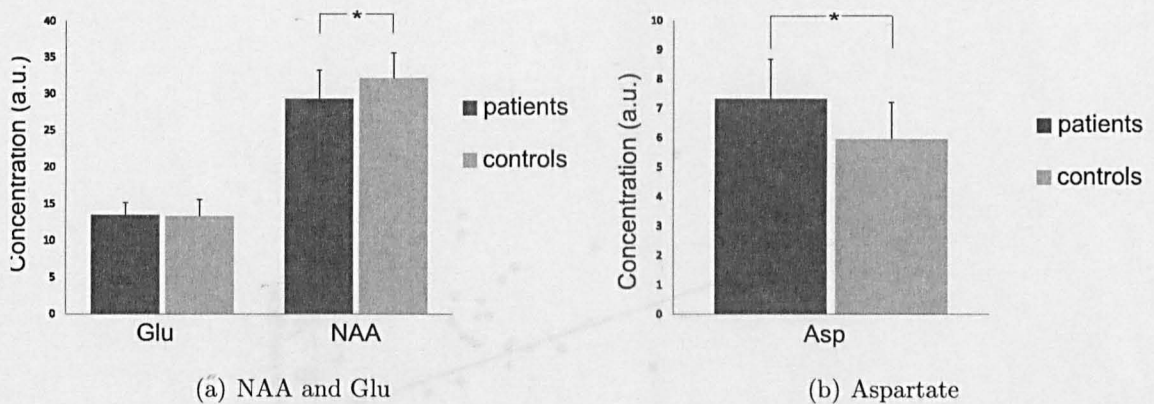
Figure 4.4: Anterior Cingulate Cortex NAA decrease (p<0.02)(a) and Aspartate increase
(b) (p<0.03) in schizophrenic patients compared to controls.

Glutamate: No change between patients and controls (figure 4.4(a)) was detected

in ACC Glu as shown in figure 4.4(a) (mean$\pm$SD $Glu_{patients} = 18.1 \pm 2.8$; mean$\pm$SD

$Glu_{controls} = 18.1 \pm 2.9$). In healthy volunteers, a strong positive correlation was found

between ACC Glu and induced theta (go/no go task) in both electrodes positioned on

Results 92

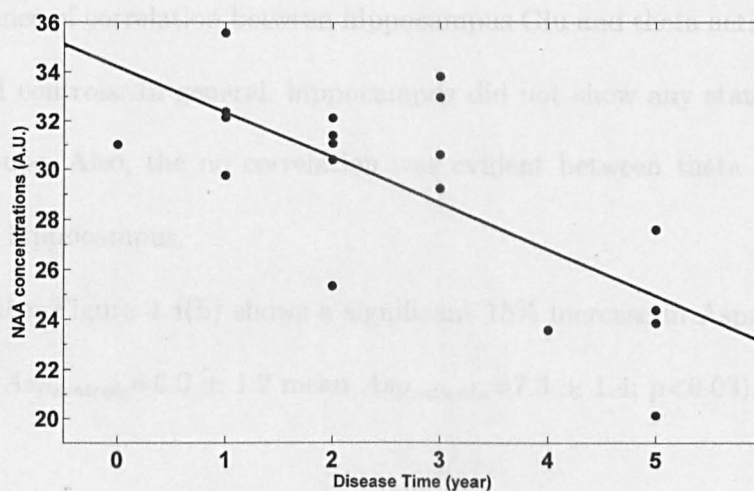the frontal cortex (C23 electrode: R=0.66 p<0.001; C21 electrode: R=0.59 p<0.01).

No evidence of correlation between hippocampus Glu and theta activity was found in patients and controls. In frontal hippocampus did not show any statistical differences between groups. Also, the no correlation was evident between theta activity and Glu levels in the hippocampus.

Aspartate Figure 4.4(b) shows a significant 18% increase in amplitude of patients vs controls (...)

Figure 4.5: Disease duration and Anterior Cingulate Cortex NAA in schizophrenic patients (R=-0.71, p<0.0007).
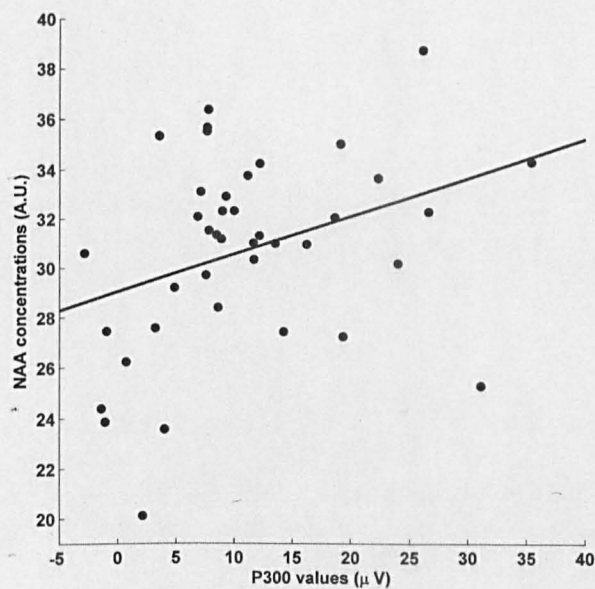

Figure 4.6: P300 amplitude and prefrontal NAA for patients+controls(R=0.35, p<0.03). The 4 electrodes under consideration showed a similar correlations. See text for details.

the frontal cortex (C23 electrode: R=0.65 p<0.001; C21 electrode: R=0.59 p<0.01).

No evidence of correlation between hippocampus Glu and theta activity was found in patients and controls. In general, hippocampus did not show any statistical differences between groups. Also, the no correlation was evident between theta activity and Glu levels in the hippocampus.

Aspartate: Figure 4.4(b) shows a significant 15% increase in Aspartate of patients vs controls ($Asp_{controls}$=6.0 ± 1.2 mean $Asp_{patients}$=7.3 ± 1.4; p<0.03).
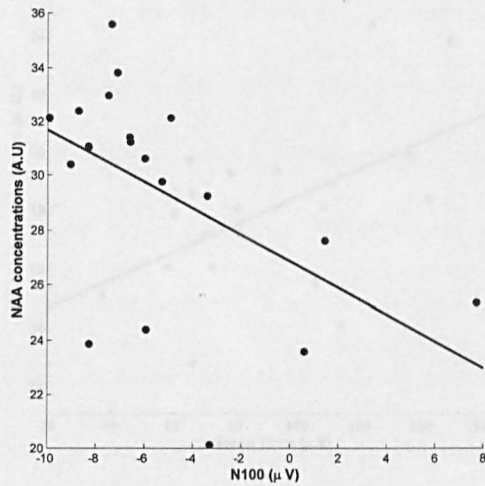
(a) Electrode C23 patients
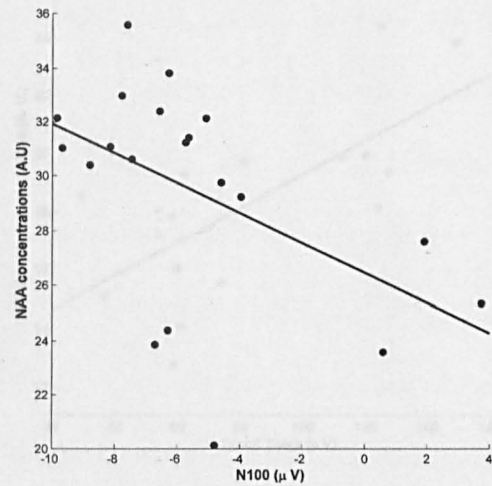
(b) Electrode C21 patients
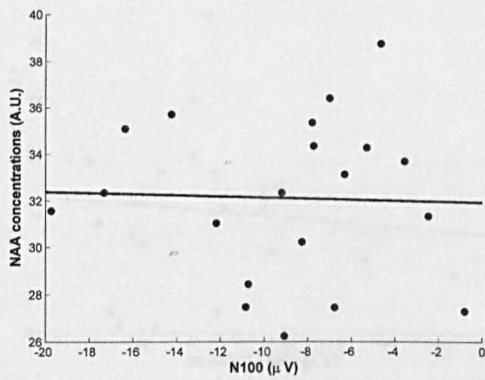
(c) Electrode C23 controls
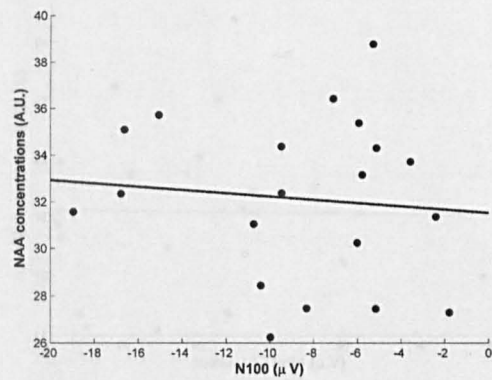
(d) Electrode C21 controls

Figure 4.7: Correlations between ACC NAA concentration and N100 for auditory oddball task in schizophrenic patients. The correlation in healthy controls is absent.

4.4 Discussion
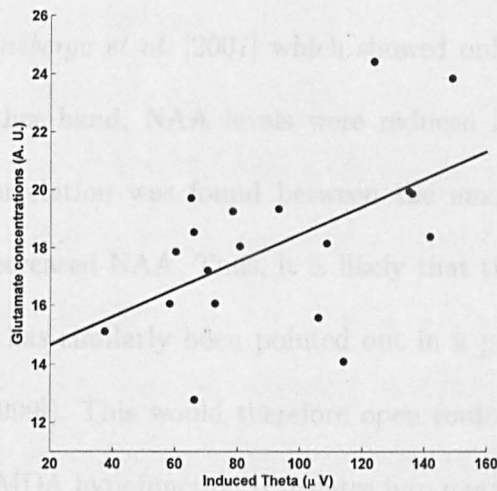
(a) Electrode C23 controls
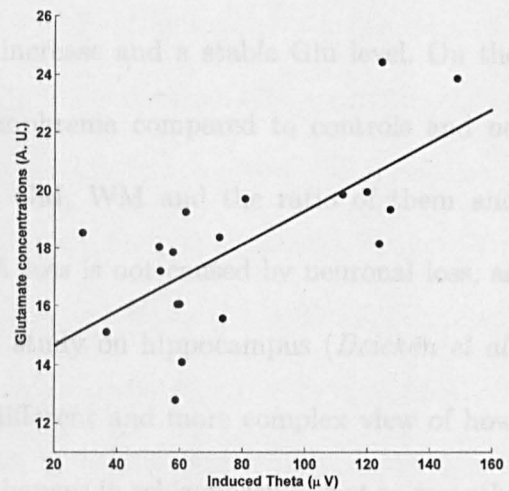
(b) Electrode C21 controls
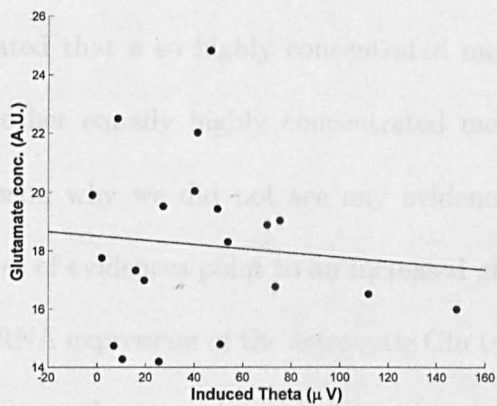
(c) Electrode C23 patients
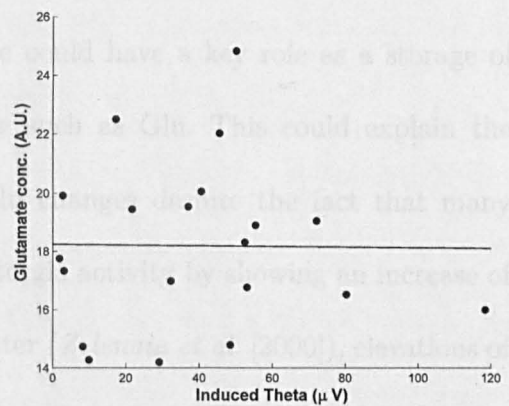
(d) Electrode C21 patients

Figure 4.8: Correlations between anterior Cigulate Cortex Glu levels and induced Theta activity for go/no-go task in controls. C23 electrode: R=0.65, p<0.001; C21 electrode: R=0.59, p<0.01. The correlation is lost in schizophrenic patients.

4.4   Discussion

Our findings show no reduction of the Glu levels in ACC and hippocampus of early schizophrenic subjects. This is in line with the studies of *Théberge et al.* [2002] and *Théberge et al.* [2007] which showed only Gln increase and a stable Glu level. On the other hand, NAA levels were reduced in schizophrenia compared to controls and no correlation was found between the amount of GM, WM and the ratio of them and decreased NAA. Thus, it is likely that the NAA loss is not caused by neuronal loss, as it has similarly been pointed out in a previous study on hippocampus (*Deicken et al.* [1999]). This would therefore open route to a different and more complex view of how NMDA hypofunction translates into metabolic changes in schizophrenia. Not so recently Clark et al. hypothesised the role of NAA as a Glu reservoir (*Clark et al.* [2006]): they stated that a so highly concentrated metabolite could have a key role as a storage of another equally highly concentrated metabolite such as Glu. This could explain the reason why we did not see any evidence of Glu changes despite the fact that many lines of evidences point to an increased glutamatergic activity by showing an increase of mRNA expression of the astrocytic Glu transporter (*Zelenaia et al.* [2000]), elevations of a neuronal enzyme (phosphate-activated glutaminase) catalyzing reactions of Glu to Gln conversion (*Gluck et al.* [2002]). It is conceivable that the increased and malfunctioned glutamatergic activity with altered Glu release in synaptic space will be accompanied by a high metabolic activity so that Glu levels are reintegrated by NAA reservoir to provide the necessary Glu. Hence, the observed NAA reduction in schizophrenia may reflect a more and more intense request of Glu over time. In fact, NAA levels in patients

show a strong and significant negative correlation with disease time but no correlation is present between subject age and NAA levels. The hypothesis of NAA as responsible of Glu stability in schizophrenia seems also to be supported by the the link with a well-defined biomarker: N100. In line with another work reporting reduction in the magnetic counterpart of N100 (N100m) (*Sörös et al.* [2006]), we observed a N100 reduction and also a correlation with NAA in patients. In fact the N100 is thought to reflect primary auditory functions as well as motivation, alertness and arousal (*Potts et al.* [1998]). Rather than a link between neuronal integrity and brain activity, as Soros and coworkers speculated, a link between neurochemical dysfunction and brain activity can be recognized: there are indeed evidences of associations of changes in N100 with NMDA receptor-mediated Glu neurotransmission such that NMDA receptor antagonist reduce N100 in humans and monkeys (*Murck et al.* [2005], *Maxwell et al.* [2006]). Hence an increase in Glu need for synaptic release in schizophrenia would generate such a deficit in NAA.

At least in the early stage of schizophrenia NAA could provide the amount of Glu required by neuron. Given that idea, we could speculate that in long disease duration NAA is no longer able to supply the sufficient Glu; evidences of a reduced Glu levels in chronic schizophrenia (*Théberge et al.* [2003], *Tayoshi et al.* [2009]) and in discordant co-twins (*Lutkenhoff et al.* [2010]) would support this hypothesis. A further evidence of this idea would be relying on the increase in Aspartate found in the present study: that indeed could be a final product of a series of reactions which are breaking down NAA to convert it to Glu. Likely these reactions would have a product accumulating over the time in the brain. To our knowledge, no other study on schizophrenia showed changes in

Aspartate, so that it would be extremely important to take this findings with caution. On the other hand, this hypothesis would start interpreting the Glu changes from a different perspective.

Interestingly, correlation of the ACC Glu levels with theta activity has been found, partially reproducing the results of a previous study (*Gallinat et al.* [2006]) that had associated theta activity with Glu levels in the hippocampus of healthy volunteers. No correlation was found when investigating the hippocampus NAA and in particular only the two frontal electrodes presented such a correlation.

Furthermore, an explanation of absence of correlation of theta activity and Glu levels for oddball task can rely on the fact that go/no-go task theta activity is mostly produced frontally (as it can be observed by Loreta analysis) while, by contrast in the oddball task, theta has also many posterior sources. Therefore, this would imply that the link is strongly local.

Remarkably, this interrelation between ACC Glu and induced theta activity was lost in patients with schizophrenia. Although our findings have to be considered preliminary, they provide first evidence that prefrontal glutamatergic activity modulates oscillatory theta activity and that this modulation is defunct in patients with schizophrenia. This dissociation may explain the cognitive deficits seen in schizophrenia despite unchanged Glu pools. An interpretation of this absence of correlation in schizophrenic patients is complex and would need more investigation. However, it is conceivable that, concordantly with the well known fact that the extracellular and vesicular Glu is only a fraction of the total cerebral Glu, the remaining part would take part into the cells' energy metabolism.

In addition, it is not clear the amount of Glu visible to spectroscopy both in a general case and in the particular case of schizophrenia. In fact, MRS studies have failed to find 20% of Glu which conversely was biochemically measured with different techniques such as high pressure liquid chromatography (*Pirttilä et al.* [1993], *Kauppinen et al.* [1994]). Thus, it is dubious to what the Glu variations might correspond and more specifically whether the vesicular and synaptic Glu might have a predominant part in the changes.

An interpretation might state that the majority of the Glu that is MRS visible is in fact associated with glucose metabolism precluding inference on neurotransmitter activity changes between patients and controls and its associations with theta activity. Nevertheless, a direct link between cingulate glucose metabolism and theta activity has been established in healthy volunteers using FDG-PET (*Pizzagalli et al.* [2003]). A similar profound link between MRS visible Glu and glucose is also evident in a study on epilepsy showing how Glu and glucose levels were closely correlated (*Pfund et al.* [2000]): that would strengthen the idea that ACC Glu pool levels predicting induced theta may reflect glucose metabolism rather than neurotransmission and then supporting the notion that MRS visible Glu mainly reflects the metabolic pool that is however linked with neuronal activity. Furthermore, hypometabolism in the frontal lobes is also considered a neurobiological correlate of schizophrenia (*Horacek et al.* [2006]); that indeed corroborates the hypothesis of a coupled interaction between metabolism and theta activity where both are reported to be decreased in schizophrenia. Few limitations needs to be stated. First of all, this study failed to obtain an accurate quantification of Gln thus reducing a part of information about the Glu released in the synaptic space. We were

indeed not able to test the hypothesis that NMDA hypofunction leads to an increase in Glu release. Furthermore, our patients were under medication and also the drug-taking was heterogeneous across all patients. That is to be considered and taken into account as an additional variability on the data since the effect of these drugs on the metabolic profile is still not clear. The last limitation is our sample size so that our results must be taken with caution against over-interpretation of the null effects.

4.5   Conclusion

Our study reported no variation in Glu levels and a disruption of the link between ACC Glu and induced theta activity which is present in healthy subject. The changes in Asp levels are to be considered still preliminary and to be further investigated. Regardless of Asp changes, a hypothesis of NAA as a reservoir of Glu might explain, at least in the early stage of schizophrenia, the reasons for a discrepancy between reduced metabolism in schizophrenia versus stable levels of Glu. In addition, we speculated that this relevant Glu backup originating from NAA is responsible for the lack of the Glu-theta link in patients. Our study failed to detect Gln so that no further investigation was possible to test whether this metabolites is also coupled to the oscillatory activity. Future investigations would then aim to search evidences of this link since Gln is surely more connected to neurotransmission pool. Importantly, patients from this study were intentionally chosen not acutely psychotic in order to study the early stage of the disease. On the other hand the psychotic state itself is an interesting correlate in schizophrenia, since this is likely to

alter the metabolic profile. Therefore, we added a preclinical study on animals allowing us to investigate a psychotic state artificially induced by ketamine NMDA antagonists.

5

In vivo neurotransmitter profiling to characterise the

effects of social isolation and ketamine-induced

NMDA antagonism: a rodent study at 7.0 Tesla

5.1 Introduction

Ketamine is an NMDA receptor antagonist that, in subanaesthetic administration, is known to exacerbate the positive, negative and cognitive symptoms in patients already affected by schizophrenia (*Lahti et al.* [1995a], *Lahti et al.* [1995b], *Rowland et al.* [2005a]). In healthy subjects it produces a wide variety of temporary behavioural symptoms and cognitive deficits similarly to those observed in schizophrenia (*Krystal et al.* [1994]). Such widely spread dysfunctions involving multiple networked regions of the brain are not observed with all psychotomimetic drugs (*Javitt and Zukin* [1991]), making ketamine and other drugs of this class excellent tools for reproducing a schizophrenic state in an experimental model. Even though it is plausible that the response to ketamine might not be identical in all aspects to actual schizophrenia's characteristics, there is agreement that

ketamine reproduces important aspects of major symptoms of schizophrenia. Also there is a potential benefit in creating a drug-induced state of NMDA receptor hypofunction to identify various physiological consequences of NMDA blockade in the brain. Despite that, studying ketamine in patients has significant ethical issues and this partially motivates its use on animal models instead. In fact, numerous studies have demonstrated the possibility to recreate some pathophysiological aspects of schizophrenia with animal models (*Dawe et al.* [2009], *Fone and Porkess* [2008]). Although it is extremely difficult to fully reproduce the complete ensemble of symptoms experienced in a schizophrenic condition, many models have successfully replicated several schizophrenia-like behaviours.

The model of juvenile social isolation is known to induce schizophrenia-like behaviour. In fact, it seems that this intervention has deleterious effects on neurodevelopment and also on adult behavior (*Fone and Porkess* [2008]). It is still unclear how these changes occur, but social isolation in rodents can be used to model environmental and emotional deprivation in humans. The main difficulty in modeling a neuropsychiatric condition such as schizophrenia in rats is the uncertainty in assessing in rodents the presence of complex symptoms typically assessable in humans. However, even though the rodents are not able to report any delusions or hallucinations and no behavioural test is able to fully evidence this complex disease, an array of tests can be utilised for a more substantial result. Rearing of rodents in isolation persistently alters the behaviour and then mimics, at least partially, the manifestations observed in schizophrenia. Evidence of differences are present as withdrawn social interaction, neophobia, reduced cognitive flexibility and dysfunctional sensorimotor gating (*Fone and Porkess* [2008]).

Prepulse inhibition of the acoustic startle reflex (PPI) are used to measure sensorimotor stage of cognitive development and it has been shown to be impaired in both isolation-reared rats (*Cilia et al.* [2001, 2005], *Geyer et al.* [1993]) and schizophrenic patients (*Kedzior and Martin-Iverson* [2007], *Ludewig et al.* [2003]). Structural neural correlates of isolation have been proved to be present as well: a study has also recently shown a volume reduction in medial prefrontal cortex (mPFC) (*Schubert et al.* [2009]). Also behavioural alterations were demonstrated to be accompanied by specific alterations in hippocampal α-tubulin isoforms and decreased MAP-2 expression which led the authors to conclude that those findings are indicative of an abnormal development of synaptic connections and reductions in neuronal cell number which in turn may contribute to the cognitive impairments resulting from isolation rearing in rats (*Bianchi et al.* [2006]).

Still few studies have looked at the neurochemical changes occurring in this animal model as well as with ketamine administration. Recently a study on the effects of ketamine on healthy volunteers has reported an elevation of Gln in the prefrontal cortex (*Rowland et al.* [2005b]). The study was performed on a 4 T scanner and *in vivo* spectra were acquired from the bilateral anterior cingulate of 10 healthy subjects while they received a subanesthetic dose of either placebo or ketamine. An increase was observed in Gln between ketamine and placebo whereas no change was detected in Glu. Similar findings were obtained by another group on animal model using a different NMDA antagonist, phencyclidine (PCP). Gln/Glu ratio showed an increase after PCP injection but the total concentration of these two metabolites remained constant (*Iltis et al.* [2009]).

Melendez et al. [2004] used microdialysis techniques to detect changes in the overall Glu release in the prefrontal cortex of isolation-reared rats. No significant changes were found about Glu release, but a specific decrease was present in the mGluR1 and mGluR5 receptor subunits in the dorsal PFC. The authors concluded that a reduced transmission is then conceivable and may result in cognitive deficits.

In rats, microdialysis has been also used to report that a subanaesthetic dose of ketamine leads to an excessive release of Glu in the prefrontal cortex, as depicted by elevated extracellular Glu in the region (*Lorrain et al.* [2003]). Lorrain et al. also concluded that the Glu elevation seen in the medial PFC is as a result of ketamine acting at a site outside the mPFC.

The aim of the present study was then to investigate at ultra high field strength both the effects of pure isolation and the effects of only ketamine on healthy animals and, ultimately, the effect of ketamine and rearing isolation on the metabolic profile. Special interest was given to the neurotransmitter pool, GABA, Glu and Gln, as well as their time course during the ketamine injection. Specifically, we aimed, according to the current hypothesis, to show a reduction of GABA and an increase in glutamatergic activity. We expected those changes to be greater in a psychotic state as it might be the state of isolated rats after ketamine injection. Also we wanted to examine the effects of isolations on the metabolic profile to see whether that reproduces differences seen in humans.

5.2   Materials and Methods

5.2.1   Animals

[1]The study made use of 16 male Lister Hooded rats. MRS data from the anterior cingulate cortex (ACC) were only obtained from 13 of the rodents (n=13), whereas data from the left hippocampus (LHC) were acquired from the remaining 3 rats. All experiments complied with Home Office regulations as detailed in the Animals (Scientific Procedures) Act 1986 and were approved by the local Ethical Review Committee. All efforts were made to minimize the number of animals used and their suffering.

The rats were equally and randomly divided into two groups: 'isolates' and 'non-isolates'. The isolates were reared in isolation from postnatal day (PND) 23-25. They had no physical interaction with their littermates, but only auditory and visual contact were allowed. The isolation period was 7 weeks. The control group (non-isolates) were housed in two groups of four from PND 23-25. Both sets of rats had free access to food and water. Temperature was maintained at around 21°C and humidity at around 60% for both groups. The isolates were maintained with minimum handling.

Prior to scanning rats were assessed in a battery of behavioural tests, each of which has translational salience to core behavioural deficits seen in schizophrenic patients. These behavioural tests not only have ensured that a robust neurodevelopmental change has been produced by the early-life environmental manipulation but also enabled subsequent

[1]The acquisition was done by Dr. M. Prior, ketamine injection and animal preparation performed by Dr. M. I. Schubert. Mr Khalid Shah, Bmedsci student, took part in the analysis of the data under my co-supervision.

cross-correlation analysis between behavioural, morphological and neurochemical changes to be determined in the same animal. More details can be found on *Schubert et al.* [2009].

The rats were anaesthetised using 1.75% isoflurane in a mixture of nitrous oxide and oxygen gas in a ratio of 2:1 and then each rat was subcutaneously injected with 25mg/kg ketamine and with same amount of saline. In order to balance any potential bias related to the sequence of injection, a cross-over model was designed: each animal was randomly assigned to a group and the order of injection of ketamine and saline was different for two groups. The group with administration of ketamine first was given saline second and viceversa (see figure 5.1).
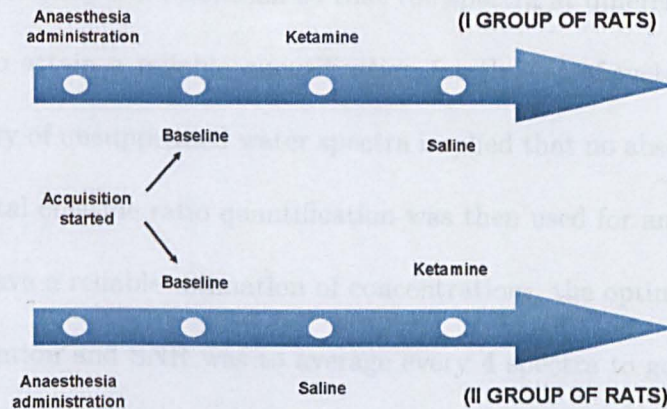
Figure 5.1: Cross-over saline/ketamine injection.

A 7 T animal scanner (Avance Biospec 70/30 USR, Bruker System) was used. Spectra were acquired from a 3x2x2 mm^3 voxel positioned in the prefrontal cortex/anterior cingulated cortex (ACC)(see figure 5.2(a)). The localization was achieved with a Point-Resolved Spin echo Sequence (PRESS) (TR=5000 ms, TE=8 ms, number of points=2048, SW=4006 Hz). From the acquisition starting point, 24 spectra with 32 averages each were

acquired: they were divided in 8 for the baseline, 12 for ketamine and 8 for saline.

The acquisition structure was conceived to give a reasonable time resolution and to allow a dynamic study of the process. Each spectrum was also acquired with VAPOR water suppression (see figure 5.2(b)).

5.2.2   Data processing

Before analyzing the data, the Bruker's filter needed to be compensated. Afterwards, a conversion to text file was performed to be able to import them into LCModel and jMRUI software packages. The small voxel and consequently high noise in the data precluded using the available temporal resolution so that the spectra at different acquisition times were averaged to attain a reliable quantification for the set of metabolites of interest. The unavailability of unsuppressed water spectra implied that no absolute quantification was possible. Total creatine ratio quantification was then used for analysis.

In order to have a reliable estimation of concentrations, the optimal compromise between time resolution and SNR was to average every 4 spectra to get 128 averages per time point. In order to reduce the line broadening due to the frequency shift among the spectra, a Matlab script based on a cross correlation method (see appendix A) automatically realigned the spectra before summing them. In case of ketamine injected first, the final output was hence structured as:

- BAS_1 Baseline (0-10 minutes)

- BAS_2 Baseline (10-20 minutes)

- KET_1 Ketamine (20-30 minutes)

- KET_2 Ketamine (30-40 minutes)

- KET_3 Ketamine (40-50 minutes)

- SAL_1 Saline (50-60 minutes)

- SAL_2 Saline (60-70 minutes)

whereas in case of saline injected first the structure was:

- BAS_1 Baseline (0-10 minutes)

- BAS_2 Baseline (10-20 minutes)

- SAL_1 Saline (20-30 minutes)

- SAL_2 Saline (30-40 minutes)

- KET_1 Ketamine (40-50 minutes)

- KET_2 Ketamine (50-60 minutes)

- KET_3 Ketamine (60-70 minutes)

where the total time is deduced from the TR×NSA. Also, by averaging the subgroups, an overall effect was investigated which included only 1 baseline, 1 ketamine and 1 saline time point. A growing interest on the changes of neurotransmitters' ratio motivated a statistical analysis of the effects on their balance.

All the quantifications were performed on LCModel software (*Provencher* [1993, 2001]) with an appropriate basis dataset. The cut-off CRLB for all metabolites with exception for GABA was 20%. All data complied with this requirement so that the total number of rats (n=13), with isolates (n=7) and non-isolates (n=6) was included for the metabolites comparison. For GABA, since the level of GABA detection was lower after ketamine, a less stringent cut-off was chosen for CRLB (28%). An entire dataset from one isolated rat was then excluded from the analysis because it did not meet the requirement.

5.2.3 Statistics

The concentrations were exported and statistically analysed in SPSS software package. All the analysis were then divided into:

1) Effects of isolation

2) Effects of ketamine

3) Combined effects of ketamine and isolation

An independent-samples t-test was applied to compare the baselines between group-housed and isolated rats (1).

A repeated measures ANOVA was applied to check statistical differences after injection, when analysing multiple time-resolved points after each injection ((2) and (3)).

Before applying any of the above tests, all variables were tested for normal distribution using the Shapiro-Wilk test.
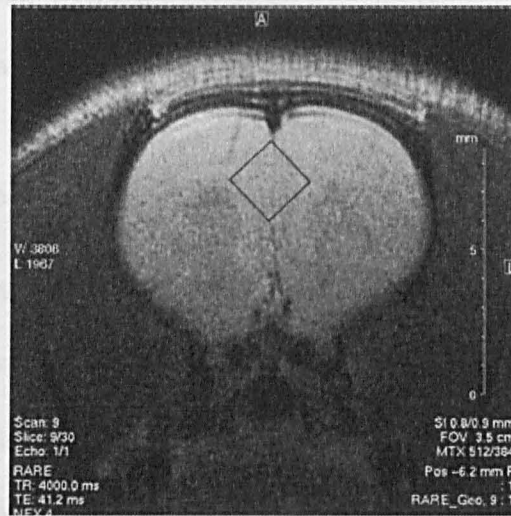
(a)
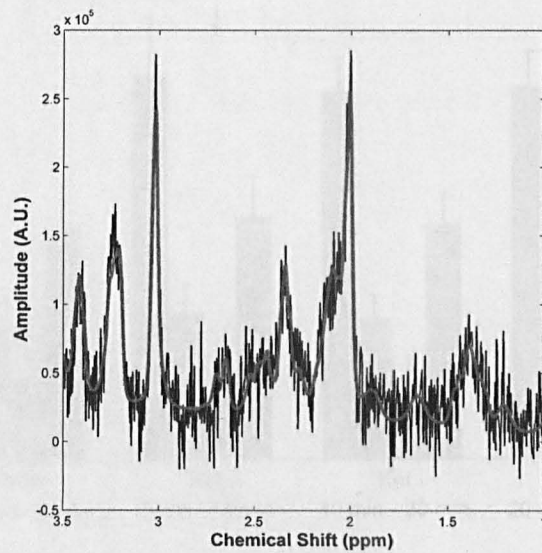
(b)

Figure 5.2: Voxel localization on rat Anterior Cingulate Cortex (ACC). (a); Correspondent spectrum TE=8 ms, NSA=128.

5.3 Results

No significant differences in the baseline values were observed in the entire visible metabolic pool between isolation-reared and group-housed rats.

5.3.1 Housing-independent analysis

Glu and NAA concentrations (see figure 5.3) were found unchanged in both housings during the injection time course. Gln proved to increase regardless of the housing (p=0.009) (see figure 5.3) at the last time point (KET_3); conversely GABA showed a decrease straight after the ketamine injection (KET_1) (see figure 5.3).

Figure 5.3: Time-resolved of metabolic variations after ketamine injection. Glu, Gln, GABA and NAA-total creatine ratio are shown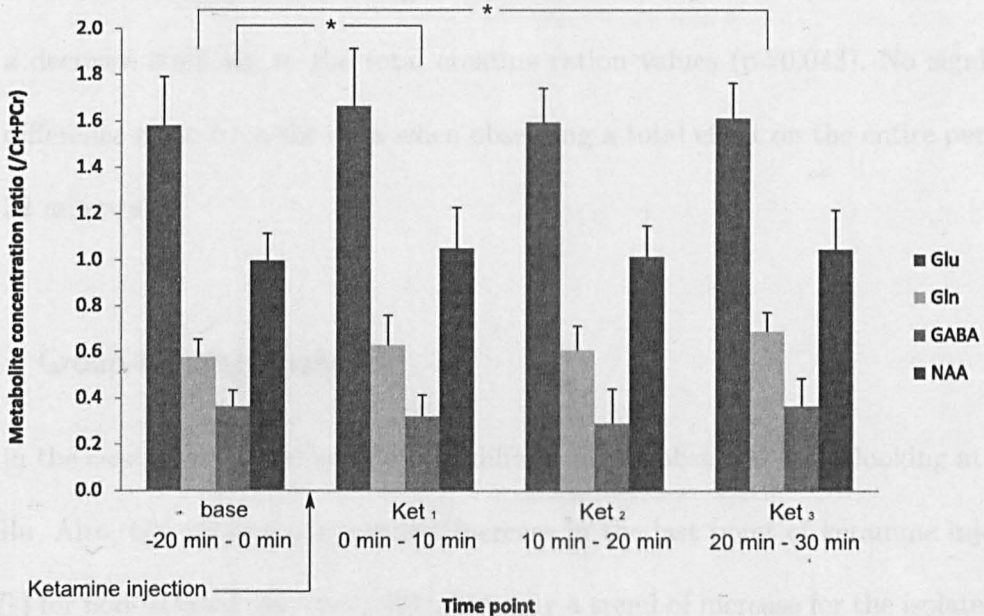. GABA decreased at the first point after ketamine injection (p<0.047); Gln is significantly increased at the last point after ketamine injection (p<0.009).

The metabolite ratios were also inspected to assess differences after ketamine injection:

- Gln/Glu displayed a significant increasing (p=0.014) from baseline to last time point (see figure 5.4).

- significant stepwise reduction in the GABA/Gln (see figure 5.4) values from baseline to first (p=0.014), second (p=0.014) and third time point (p=0.017), indicating that GABA levels fall as soon as the ketamine is administered and continue to go down for up to at least 30 minutes post injection.

- a similar tendency of decreasing is also evident in GABA/Glu, but the data show a decrease similarly to the total creatine ration values (p=0.043). No significant difference arose from the data when observing a total effect on the entire period of 32 minutes.

5.3.2 Group-housing analysis

Even in the case of separated analysis, no difference was observed when looking at NAA and Glu. Also, Gln showed a significant increase in the last point of ketamine injection (KET_3) for non-isolated rats (p=0.021), but only a trend of increase for the isolated rats which failed to be significant (p=0.108), see figure 5.5. GABA did not show a change after the ketamine injection as in housing-independent analysis. A trend of decrease in GABA for KET_1 (p=0.070) and KET_2 (p=0.078) was detected. In contrast, a significant drop was observed exclusively for isolated rats at the last time point (KET_3): in fact, an

Figure 5.4: Time-resolved ACC metabolic changes in isolated and group-housed rats in response to 25mg/kg ketamine injection. GABA/Glu is significantly decreased at the first ketamine point in time ($p < 0.043$). Gln/Glu shows a significant increase 32 minutes after ketamine injection ($p < 0.01$), GABA/Gln decreases significantly at the first ($p < 0.045$) and also second point ($p < 0.007$).

opposite tendency (not significant) of GABA increase was suggested in the group-housed rats. This was however significantly different from the first time point after the ketamine injection ($p < 0.032$), see figure 5.6. Analysis of GABA-Gln ratio revealed decreased values in rats reared in isolation for all three time points (KET_1: p=0.014; KET_2: p=0.014; KET_3: p=0.017; see figure 5.7).

Figure 5.5: Time-resolved ACC Gln concentrations in isolated and group-housed rats in response to 25mg/kg ketamine injection. A significant increase is observable in group-housed rats (p=0.021) but only a trend of increase is present for isolated rats (p=0.108).

Figure 5.6: Time-resolved ACC GABA in isolated and group-housed rats in response to 25mg/kg ketamine injection. GABA shows different trend for group-housed and isolated rats: respectively significant decrease ($p < 0.032$) from the baseline point and significant increase within ketamine injection points.
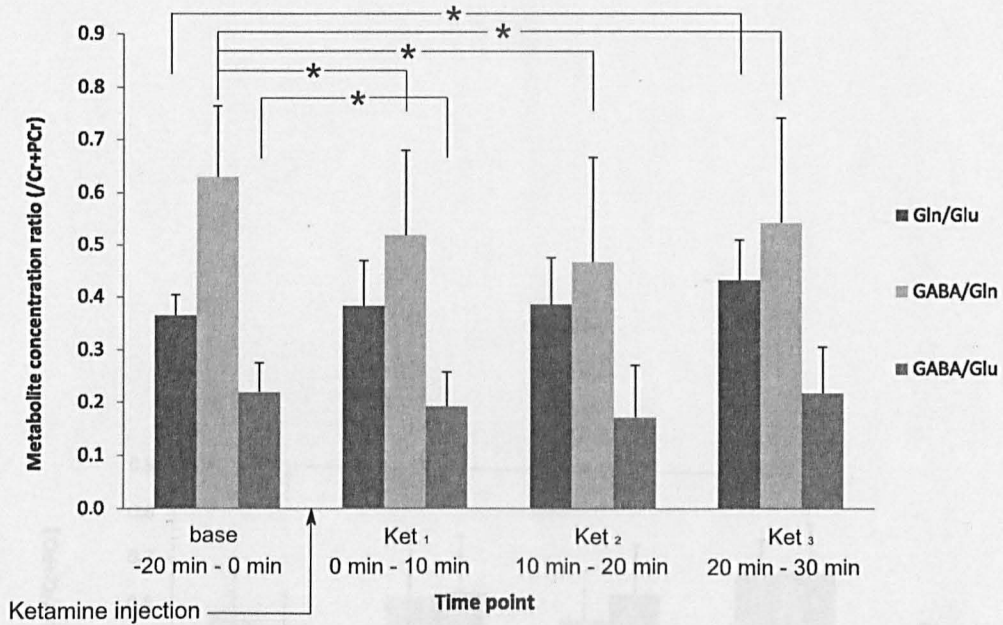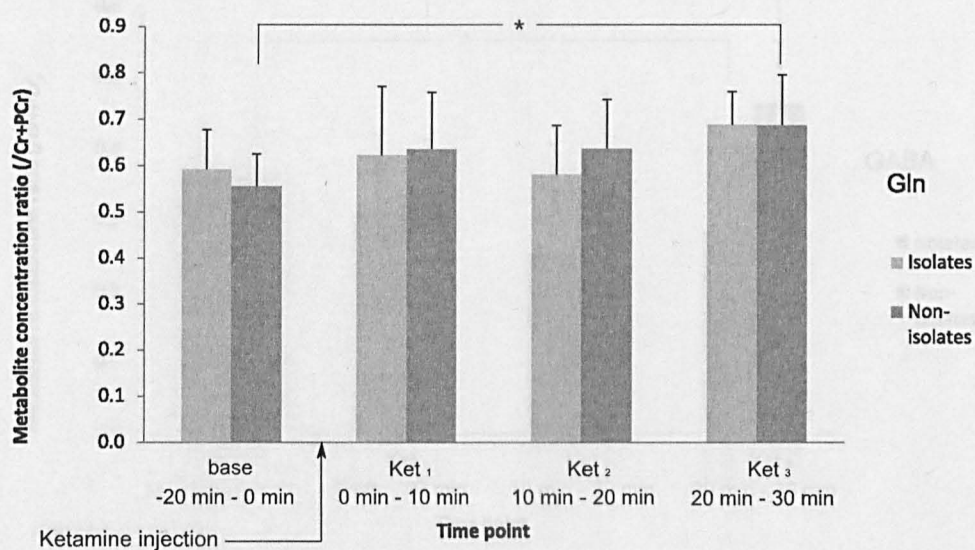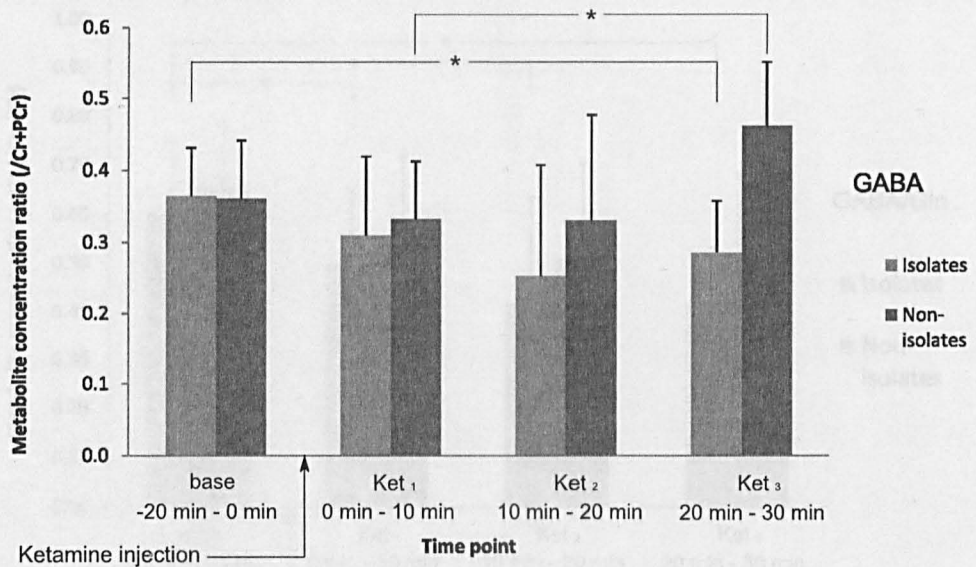
Figure 5.7: Time-resolved ACC GABA-Gln in isolated and group-housed rats in response to 25mg/kg ketamine injection. Significant drop in the ratio: KET_1, p=0.014; KET_2, p=0.014; KET_3, p=0.017.

5.4   Discussion

In summary, no difference was observed between the group-housed rats reared in a social isolation. After ketamine injection ACC NAA and Glu were stable in line with what has been found in the study on PCP by Iltis and coworkers (*Iltis et al.* [2009]), where Gln/Glu ratio, rather than their absolute concentrations, was reduced. Conversely, regardless of the group housing, after about 30 minutes from an injection of 25 mg/kg of ketamine a significant increase in Gln was observed. Consequently, even the Gln and Glu ratio was significantly increased, reproducing the main results of the just cited study. The stability of Glu can be interpreted in light of some important considerations about the Glu pools. Glu is indeed involved in both a metabolic and neurotransmission pool and MRS cannot distinguish between the two (*Pirttilä et al.* [1993], *Kauppinen et al.* [1994]). In fact, the neurotransmitter Glu is probably packed in vesicles and then likely invisible to NMR, whereas Glu in the presynaptic space is quickly removed after its release and converted back to Gln. Gln was thus speculated to reflect the glutamatergic synaptic activity more appropriately than Glu levels, and, indeed, it has been shown that Gln is a good index of the turnover of the synaptic Glu involved in neurotransmission (*Rothman et al.* [2003], *Kanamori et al.* [2002]). Given that, the increase in concentration of Gln might indicate that NMDA blockade leads to a larger amount of Glu release at the postsynaptic terminals of the glutamatergic pyramidal neurons.

Beside that, the elevated levels of Gln might be a further measurement of an increased activity which was also observed by studies looking at the BOLD fMRI signal (*Littlewood et al.* [2006a,b]). Such increase is also in line with studies that used MRI perfusion and

that reported an increase in hemodynamic response following PCP administration in animals (*Gozzi et al.* [2008]). Additionally, studies using positron emission tomography (PET) have shown a frontal lobe activation in rCBF and higher CMR_{glu} indicating a metabolic hyperfrontality (*Holcomb et al.* [2001], *Vollenweider et al.* [1997]). Evidences of a similar effect on humans come from Rowland et al. (*Rowland et al.* [2005a]) who proved an increase following ketamine administration.

Compared to the study of Iltis and colleagues (*Iltis et al.* [2009]), an interesting significant GABA decrease was measured in rats reared in isolation but not in group housed rats. The study from Iltis *et al.* had indeed shown a not significant reduction in GABA after PCP injection. To our knowledge, this is the first *in vivo* study characterizing the metabolic effect of ketamine on GABA. This also opens a new route of further investigation about the GABA's role in schizophrenia. A high-resolution magic spinning angle study on postmortem tissues at ultra high field strength (16 T) was able to detect a similar decrease in GABA concentration by comparing prefrontal white and grey matter of 10 schizophrenia and 10 control individuals (*Prabakaran et al.* [2004]). According to the NMDA hypofunction hypothesis, as a NMDA antagonist, ketamine would cause NMDA receptor blockade on GABAergic interneurons with a consequent decreased inhibitory activity from the GABAergic inhibitory interneurons and resulting in a downstream hyperglutamatergic state (*Moghaddam et al.* [1997], *Olney and Farber* [1995], *Olney et al.* [1999]). Our study failed to see a significant decrease in GABA exclusively for isolates at the first time point where the housing-independent analysis showed a significant drop for all rats. Most likely the reason relies upon the small sample size for the isolates. However,

a trend of decrease is observed and that would fit in the hypothesis of decreased inhibitory activity from the GABAergic system. In fact, we can speculate that the earlier effect of ketamine on the GABA could be interpreted as a cause of the observed Gln increase later on. A further evidence is attainable from the GABA and Gln ratio data where it is arguable that the second point in time expresses this progressive passage from reduced inhibitory activity to high glutamatergic activity. This effect is very profound in rats reared in isolation thus supporting the hypothesis that the isolation housing would lead the animals to be more susceptible to the ketamine effects and consequentially to NMDA blockade.

In line with that, the reason of the last time point GABA increase in group housed rats could be found in a process which tempts to restore the GABA level back to normal. GABA decrease resulted successfully restored in healthy animals, but such a process might be no longer effective when a not complete neuro-development takes place, thus leading to a longer and more persistent effect over time. These explanations remain speculations and caution is needed to avoid over-interpretations of the results. Further investigations need to be undertaken to address this effect.

5.5 Conclusions

A study on an animal model of schizophrenia was undertaken. The work involved also the injection of ketamine to study the psychotic state od the disease. Two interesting changes were observed in the study as an effect of ketamine administration: a Gln increase

showing an higher glutamatergic activity; a GABA decrease in isolates giving evidence of the more profound effect of ketamine on rats lacking a complete neuro-development.

Part III

GABA-optimised sequence and 2D fitting

procedure

6

Optimised PRESS sequence for GABA detection

6.1 Introduction

Gamma aminobutyric acid (GABA) is the most important inhibitory neurotransmitter in the central nervous system and a large number of psychiatric and neurological disorders such as anxiety disorders, epilepsy, schizophrenia and insomnia (*Wong et al.* [2003]) have been associated with GABAergic dysfunction. Proton MR spectroscopy (1H-MRS) is the only technique to non-invasively assess cerebral GABA levels and thus characterise disease related alterations and the effects of medical treatment. Quantification of intracerebral GABA is however challenging since resonances of GABA overlap with signals of other metabolites that are more highly concentrated than GABA with concentrations between 1.4 mM and 2 mM (*Govindaraju et al.* [2000]). Therefore, in vivo spectroscopic determination of GABA mainly relies on elaborated editing sequences that are not routinely available on clinical scanners.

The GABA has 3 main groups of protons, C2 protons at 3.0 ppm, C3 at 1.88 ppm and C4 at 2.28 ppm. Around 3.0 ppm, GABA is strongly overlapped by the methyl

group of creatine. Fortunately, the absence of J-coupling allows the use of a variety of spectroscopic techniques to suppress it. The first technique to detect GABA utilized semiselective refocusing pulses to inhibit J modulation of C4 GABA resonance (3.00 ppm) (*Rothman et al.* [1993]). After that, several methods have been implemented making use of multiple quantum filtering (*Keltner et al.* [1996, 1997], *Shen et al.* [1999, 2002]), two-dimensional spectroscopy (*Ke et al.* [2000], *Schulte and Boesiger* [2006a]) as well as numerically GABA optimized inversion pulse for homonuclear editing sequence (*Hetherington et al.* [1998]). Although techniques such as multiple quantum filtering or spectrally selective pulse provide an estimation of GABA concentration, they fail to detect the entire spectrum. Conversely, two-dimensional spectroscopy methods allow the simultaneous detection of the full spectrum and the single GABA.

In methods making use of two-dimensional spectroscopy, a full spectrum as well as single GABA can be detected. Schulte and Boesinger (*Schulte and Boesiger* [2006a]) calculated intra-subject and inter-subject GABA coefficients of variations (CV) respectively of 17% and 22%. Nevertheless, a longer scanning time makes it not ideal for clinical applications.

Among the J-editing methods, a technique embedded in Point Resolved Spectroscopy localization (MEGA-PRESS) (*Mescher et al.* [1998]) has evolved. MEGA-PRESS is relatively easy to implement compared to other editing techniques widely divulging its use for research purposes (*Licata et al.* [2009], *Edden et al.* [2009], *Floyer-Lea et al.* [2006], *Muthukumaraswamy et al.* [2009]). However, MEGA-PRESS is currently still not available on commercial scanners. A further drawback is the doubling of the acquisition time

compared to a PRESS for the same number of averages. A couple of studies (*Bogner et al.* [2010], *Evans et al.* [2010]) have also shown MEGA-PRESS CV for long term reproducibility. Specifically, Bogner and colleagues calculated GABA CV with voxel size of $25 \times 30 \times 30 \ mm^3$ and 128 averages: they found CV of GABA concentration relative to water of 15% and relative to Cre of 13.3%. By doubling the time of acquisition and the voxel size, Evans and coworkers computed the MEGA-PRESS CV for GABA obtaining 9.1% in the visual cortex and 12% in the sensorimotor regions.

Our goal then was to obtain a similar quality like MEGA-PRESS by testing whether clinically available sequence parameters might allow comparable result in the more restricted time of clinical procedure.

In order for a standard PRESS to meet the requirement of robustness needed we performed a validation by using simulations and *in vitro* tests. Furthermore, we assessed *in vivo* short and long-term reproducibility between subjects. In this chapter, the feasibility of obtaining reliable GABA estimation using a clinically available sequence was tested. To this end, a simulation based parameter optimisation was performed, followed by *in vitro* and *in vivo* validation.

6.2   Theory and Simulations

Simulations were performed to narrow the choice of sequence parameters for subsequent *in vitro* and *in vivo* experiments. Simulations were performed using Spinevolution software (*Veshtort and Griffin* [2006]) that was also used to create LCModel (*Provencher*

[1993, 2001]) basis dataset for the *in vitro* and *in vivo* analysis. For this study we focused on GABA C4 (2.28 ppm) and C3 (1.89 ppm) proton resonances: the C3 resonance is particularly interesting as it may be resolved from the NAA singlet if linewidths are reasonably narrow. Nevertheless, at short TEs, macromolecules and lipids may confound the fitting in this ppm range. As a consequence we chose longer TEs to mitigate this otherwise unavoidable problem. Numerical simulations hence covered different TE_1s ranging from 5 ms to 30 ms (with 2.5 ms step size) for long TEs ranging from 70 ms to 130 ms (with 5 ms step size). To emulate a realistic linewidth, 8Hz Gaussian data apodization was applied, and then the amplitude of the two peaks (C4 and C3) was colour-coded and displayed for the TE_1/TE matrix (figure 6.1). The two matrices were able to provide a first overview of the two amplitudes' pattern and allowed to easily recognize the maximum amplitude for both peaks.

Similar simulations were carried out to identify and minimize the amplitude of the N-acetylaspartate-Glutamate (NAAG) signal. In fact, NAAG C3 protons (1.88 ppm) have a multiplet resonating very close to the C3 GABA protons and hence it can affect GABA quantification. The NAAG glutamate moiety is not usually included into LCModel basis dataset and this might generate an unespected independency between GABA and NAAG concentrations (*Hofmann et al.* [2002]). Conversely, at higher field strengths, NAAG glutamate moiety was accounted for (*Tkác et al.* [2009]).

Opting for the shortest TE_1 possible in the PRESS sequence, to minimize the propagation of the multiple coherences, a cross checking of the GABA maximum amplitude of both protons and minimum contamination arising from NAAG C3 proton amplitude

was performed. Corresponding to TE=105 ms and TE_1=15 ms (GABA-PRESS) the amplitude of the GABA peak for both protons under consideration was maximum whereas the NAAG multiplet total amplitude was very close to the minimum. In addition, NAAG multiplet at 1.9 ppm is far more complex than GABA multiplet thus leading to not only a small difference of their respective peaks when a line broadening is applied, but also to substantial reduction of NAAG visible peak. Figure 6.2(b) shows how, in the case of GABA-PRESS, a significant difference arises in the C3 protons amplitudes between NAAG and GABA.

However, the simulations were considered only exploratory, since there was no T_2 decay applied. The second part of the study tried to assess the reproducibility of measurements and to determine possible bias.
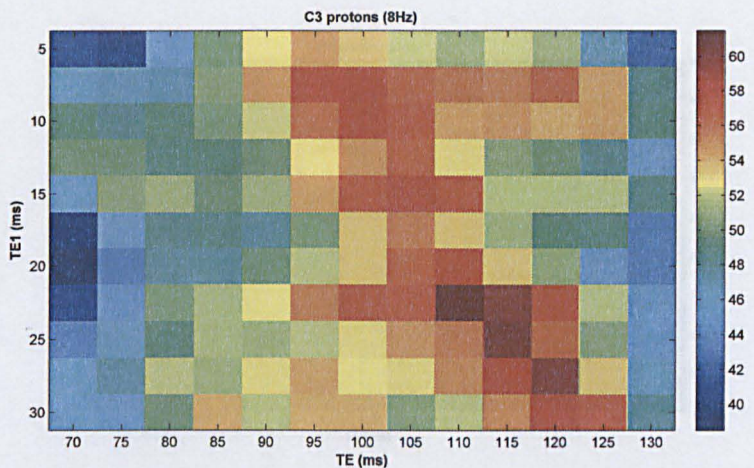
(a) C3 protons (8Hz)
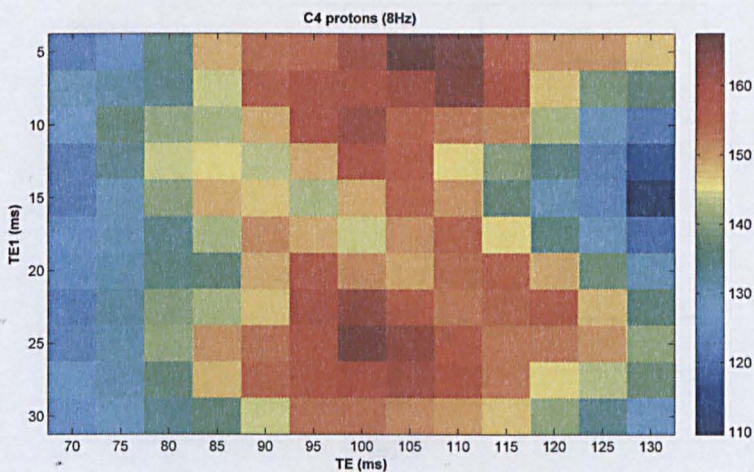
(b) C4 protons (8Hz)

Figure 6.1: Peak amplitude in arbitrary units for GABA C3 (1.89 ppm) and C4 (2.28 ppm) protons. 8Hz apodization was chosen to emulate realistic spectrum. The matrices were used to assess the maximum amplitude for both protons.

(a)

(b)

Figure 6.2: (a)Peak amplitude in arbitrary units for NAAG C3 (1.88 ppm) protons. 8Hz apodization was chosen to emulate realistic spectrum. The matrix was used to assess the minimum amplitude for the protons under consideration. (b) A simulation of peak difference between NAAG and GABA for GABA-PRESS.

6.3   Materials and methods

6.3.1   *In vitro* experiments

All phantoms were prepared by making use of compounds from Sigma Aldrich company and by diluting them in distilled water in plastic containers. After the dilution, where it was necessary, the pH was also adjusted back to 7.2 by adding to the solution NaOH or HCl.

The *in vitro* experiments made use of 2 phantoms prepared for this study: the first phantom containing only GABA (3.28 mM) and the second phantom emulating the *in vivo* concentrations and hence containing NAA, mIns, Glu, Gln, GABA and Lac, with the concentration values reported in table 6.1. Spectra (64 averages and TR=4000ms) with PRESS TE_1=15 ms and TE=105 ms, and PRESS with TEs of 40 ms and 80 ms were acquired from human-like phantom, whereas spectra (64 averages and TR=4000ms) with TEs ranging from 45 ms to 185 ms stepping by 20 ms were acquired from the phantom containing GABA. All the data were collected in blocks of 16 averages and, during the processing, they were automatically aligned and averaged. The fitting was performed in LCModel both for human-like phantom spectra and GABA's one. The fitting of pure GABA needed an operator input of shift due to the fact that the main metabolites (NAA, Glu) were not present in the spectra and LCModel could not determinate the right shift to be applied to the spectrum.

The GABA-NAA ratio values from the fitting were compared to the real GABA-NAA ratio values for each sequence (PRESS40, PRESS80, PRESS105). The choice of

GABA-NAA ratio was made to reduce the effect of calibration among sequences with different TEs. Furthermore, NAA values are the least affected by uncertainties in the quantification and then NAA is more appropriate as reference. The LCModel coefficients for NAA and GABA were corrected for relaxation before the comparison. The amplitudes' computation was performed on LCModel both for NAA and GABA. NAA T_2 value was estimated from its computed amplitudes at 40 ms, 80 ms and 105 ms on the mixed phantom. On the other hand, GABA T_2 value could not be estimated from the same data as the LCModel fitted amplitudes were not sufficiently reliable. The relaxation factor was indeed deducted from the data acquired on the GABA phantom. The first and the last TE values (TE=45 ms and 185 ms respectively) were excluded from the exponential fitting because they were visually identified as outliers and also because the CRLB was found >20%.

Table 6.1: Mixed phantom metabolite's concentrations used for the *in vitro* test.

Metabolite	Real Concentration (mM)
NAA	10
Glu	9
Gln	4
mIns	6
GABA	1.6
Lac	0.6

6.3.2 *In vivo* experiments

The *in vivo* experiments were approved by local Medical school's Ethics Committee and all volunteers taking part in the study gave written informed consent.

A 3T Philips Achieva scanner (software release 2.5.3) equipped with 8 channel phased array head coil was used. During all protocols, two of the three sequences used in the *in vitro* experiments were used: a PRESS TE=80ms and TE_1=10ms (PRESS80) and a PRESS TE=105ms and TE_1=15ms (GABA-PRESS); both of them were acquired with $25 \times 25 \times 25mm^3$ voxel size, NA=128, TR=3000ms. Second order pencil beam shimming method on a manually selected volume of interest and water suppression by excitation prior to every acquisition were applied as implemented on the Philips platform. Unsuppressed water spectra were also acquired prior each acquisition.

The protocol tested two different short term reproducibility (intrasession scan-rescan and scan-rescan with repositioning in between) and long term reproducibility.

A For the intrasession scan-rescan test 5 subjects were scanned to assess the short term coefficients of variations. 5 GABA-PRESS sequences were acquired on 2 different regions: 3 of them on the ACC and 2 on precuneus (see figure 6.3). Before assessing scan-rescan variability, these data acquisitions also aimed to determinate the influence of NAAG peaks on the GABA quantification. For clarity more details are provided in the next section, **NAAG inclusion test**.

B For the scan-rescan reproducibility test with repositioning 7 subjects were recruited. In two different sessions, separated by 10 minutes, 2 sequences GABA-PRESS and

PRESS80 were included into the protocol. In order to completely reproduce the variability between scans by including head repositioning, each subject was taken out the scanner between the sessions. A voxel was positioned on the ACC.

C To assess long term variability, 2 more subjects were scanned 3 times within a period of 3 weeks with a week apart between each scan.

D In order to assess robustness and sensitivity of the GABA measurement both within subjects and within regions 7 healthy volunteers (mean age $\pm$ SD $= 22 \pm 3$ years) were scanned by choosing two regions, ACC and precuneus as in (**A**).

Figure 6.3: Example of localization in the ACC and in the precuneus.

Spectra alignment and averaging was made by using j-MRUI whereas simulated spectra manipulations were embedded in an *ad hoc* Matlab script. All concentrations were

estimated by LCModel software. The basis datasets for the processing included the following metabolites: NAA, NAAG, Glu, Gln, GABA, Cho and PCh, Cre and PCr, Lac, Ins, Ala, Asp, Glc. For the cases **A** and **C** the CV was expressed as the ratio SD/mean. In addition, the percentile difference (PD) was computed in the case **B**. The PD was determined as the absolute variation in concentration between scan 1 and scan 2 divided by their average concentration for each metabolite. The CV values and PD were expressed as percentage of mean value.

NAAG inclusion test

As the simulations highlighted, there is a small inclusion of NAAG in the peak at 1.9 ppm, which can be misinterpreted as GABA. In order to establish whether this NAAG contribution is negligible, a preliminary *in vivo* test was required prior to the *in vivo* reproducibility. Simply incorporating the NAAG spectrum into the LCModel basis-dataset does not provide sufficient information about the two contributes originating from GABA and NAAG to the peak at 1.9 ppm because NAA usually obscures the NAAG singlet thus making the NAAG fitting unreliable. Consequently, the NAAG multiplet area resonating at 1.9 ppm remains uncertain and no negligibility limit can be assessed. For this reason, two different data processing approaches were taken into account by using two different basis-datasets:

1) Total NAAG;

2) Two separate basis spectra respectively for the NAAG singlet (1.9 ppm) and NAAG multiplets (Split NAAG).

Most of the times NAAG singlet dominates the entire fitting of the NAAG spectrum since it is more visible compared to the multiplets. On the other hand, as already stated, it is hard to distinguish NAA singlet from NAAG singlet. Our approach relied upon the idea that LCModel may manage the two components of NAAG separately and thus varying the multiplets independently from the possible identification of the singlet. That is beneficial to have an estimate of the upper limit of the 1.9 ppm NAAG multiplets contribution since they are not restricted by successful fitting of the NAAG singlet.

In order to compute the upper limits and to assess the negligibility of the NAAG misinterpretation, the concentration percentage differences have been evaluated. In particular, the Absolute Difference Ratio (ADR) and the Relative Difference Ratio (RDR) have been calculated according to the following formulas:

$$(6.1) \qquad ADR = 2 \cdot \frac{\mid Met_{SplitNAAG} - Met_{TotalNAAG} \mid}{\mid Met_{SplitNAAG} + Met_{TotalNAAG} \mid}$$

$$(6.2) \qquad RDR = \frac{\mid Met_{SplitNAAG} - Met_{TotalNAAG} \mid}{\mid NAAG_{mult} - NAAG_{singl} \mid}$$

6.4 Results

6.4.1 *In vitro* experiments

The *in vitro* experiment itself tested the sequence reliability in comparison to shorter echo time sequences by focusing on measuring known concentrations in phantoms. The spectra acquired on the mixed phantoms and two spectra acquired from the GABA phantom are shown in figure 6.4 and 6.5 respectively.

(a) Spectrum TE=40 ms

(b) Spectrum TE=80 ms

(c) Spectrum TE=105 ms
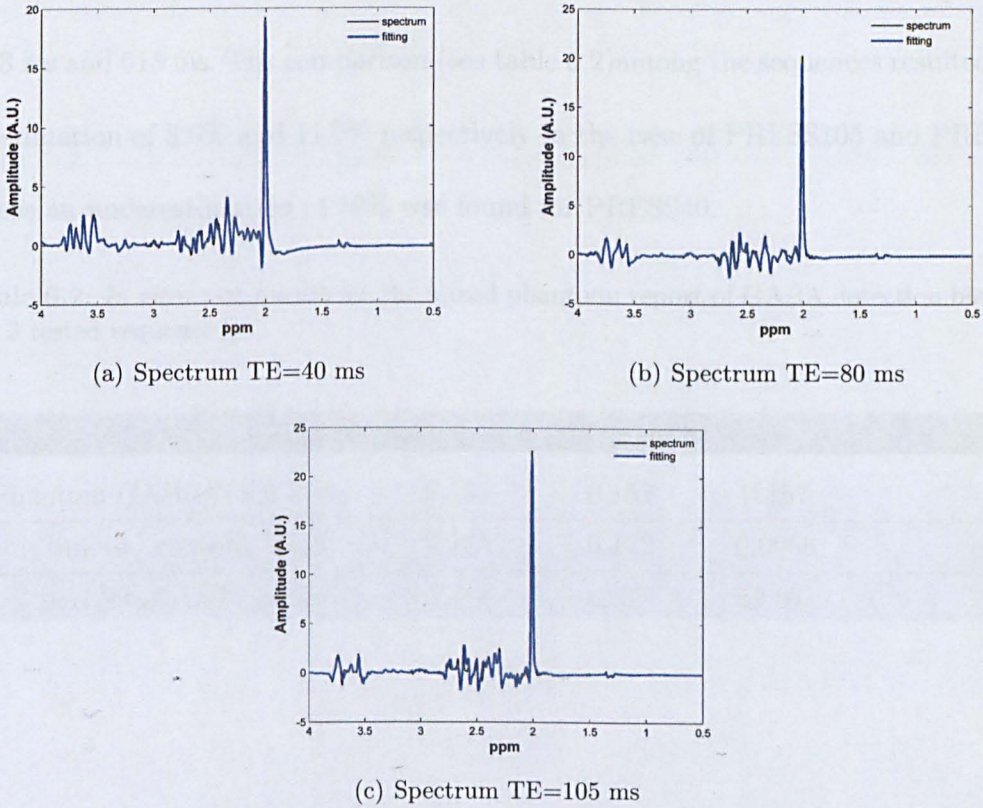
Figure 6.4: Three spectra acquired on a mixed phantom.

Among all the sequences tested, PRESS105 reported the minimum theoretical standard deviation (CRLB=2%). The GABA and NAA T_2 estimates were respectively equal

(a) Spectrum TE=85 ms

(b) Spectrum TE=105 ms
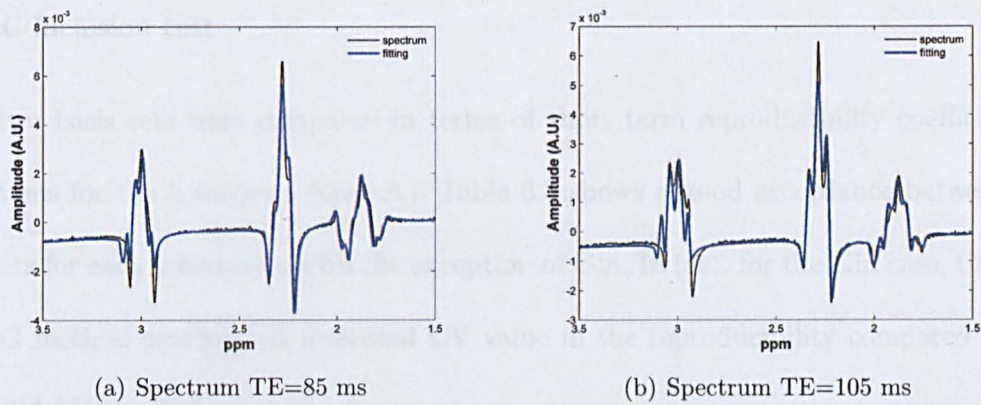
Figure 6.5: Two out of eight spectra acquired on a phantom containing pure GABA and used to compute T_2.

to 203 ms and 613 ms. The comparison (see table 6.2)among the sequences resulted in an overestimation of 3.6% and 11.9% respectively in the case of PRESS105 and PRESS80, whereas an underestimation of 59% was found for PRESS40.

Table 6.2: *In vitro* test results for the mixed phantom: report of GABA detection bias for the 3 tested sequences.

	PRESS105	PRESS80	PRESS40
Phantom GABA-NAA ratio	0.157	0.157	0.157
estimated concentration	0.155	0.172	0.0966
percentage difference	3.6%	11.9%	59.0%

6.4.2 *In vivo* experiments

1

---

[1]The results for the NAAG inclusion test are reported before the section of short reproducibility (case **A**) even though the subjects are the same.

NAAG inclusion test

The two basis sets were compared in terms of short term reproducibility coefficient of variations for the 5 subjects (case **A**). Table 6.3 shows a good accordance between the two sets for each metabolite with the exception of Gln. In fact, for the Gln case, the split NAAG method provides an increased CV value in the reproducibility compared to the total NAAG method.

Table 6.3: Short term reproducibility in terms of CVs for all 5 subjects relating to the two different basis-datasets. A good accordance is shown for all metabolites with the exception of Gln, which has a bigger CV value for the split NAAG method.

Subject	GABA (σ (%))	Glu (σ (%))	Gln (σ (%))	NAA (σ (%))
Total NAAG				
N° 1	13.3	2.2	16.6	0.9
N° 2	10.4	1.3	8.2	1.1
N° 3	16.3	1.3	27.5	1.0
N° 4	7.7	1.4	3.1	2.6
N° 5	8.8	1.6	7.1	1.1
Average	11.3(3.5)	1.6(0.3)	12.5(9.7)	1.4(0.7)
Split NAAG				
N° 1	11.5	2.3	19.8	0.9
N° 2	14.7	1.0	12.3	1.5
N° 3	12.4	2.1	54.1	0.8
N° 4	8.6	1.4	9.1	2.0
N° 5	12.8	2.4	12.2	1.3
Average	11.9(2.4)	1.9(0.6)	21.5(18.7)	1.3(0.5)

The table 6.4 indicates the two percentage changes in concentration depending on the basis-dataset used. The two values in the case of GABA are small: its variation in concentration is about 4% of the concentration itself and that is about 2% of the difference in quantification between the separate multiplet and singlet basis and the total NAAG

basis.

Table 6.4: Percentage differences between singlet and multiplet fitted concentrations for short term reproducibility

Reproducibility	GABA (σ (%))	Glu (σ (%))	Gln (σ (%))	NAA (σ (%))
ADR (eq. 6.1)	4.3(4.3)	0.5(0.6)	27.0(16.3)	0.9(0.8)
RDR (eq. 6.2)	2.6(2.3)	2.0(2.3)	14.8(1.5)	5.5(4.6)

The analysis of the theoretical correlation matrix computed from Fisher information matrix led to the same conclusions: by computing the correlations among the basis metabolites in the two different cases under consideration, see figure 6.6, the NAAG multiplet is very poorly negatively correlated to the GABA spectra. Therefore, that may be an additional evidence of the weak dependence between the GABA and NAAG protons generating the peak of interest at 1.9 ppm. This means that the NAAG contribution, and more importantly the error in the fit, can be considered negligible, despite the fact that some of NAAG protons resonate at the same frequencies of some GABA protons.

Reproducibility

Figure 6.7 shows an example for the fits for the entire spectrum and the single metabolites' components. No spectra have been excluded from the analysis.

A For the intrasession scan-rescan test to assess short term reproducibility, the results for each subject are shown in the table 6.3. For comparison, a table (see table 6.5) reporting the CVs and the CRLB for each subjects is displayed. The mean values

for the CVs are in general smaller than the corresponding CRLBs except for NAA. The mean values for the 4 metabolites are also reported in the table 6.6.

B For the scan-rescan reproducibility test with repositioning the CVs are reported in the second row of table 6.6. Furthermore, CV of **PRESS80** are shown in table 6.7. The GABA values exceed the 20% whereas the Gln values are below 10%.

C For long term reproducibility the results are shown in table 6.6. The CV for GABA was 11.9 %. The GABA-PRESS reached a Glu long term reproducibility CV value of 6.9% whereas Gln was unreliably measured.

D On a larger number of subjects the CRLB showed a good fitting in both prefrontal cortex and precuneus regions (table 6.8) in good agreement to CVs. Also, the obtained mean concentration values for GABA are (a.u. mean±SD) 1.76±0.15 in the precuneus and (a.u. mean±SD) 1.73±0.45 in the ACC.

Table 6.5: Short term reproducibility in terms of CVs and CRLBs for all 5 subjects for GABA PRESS TE=105 ms. The CVs and the CVs' average are the same as in table 6.3 and are reported again for comparison purposes.

	Subject	GABA (σ (%))	Glu (σ (%))	Gln (σ (%))	NAA (σ (%))
CV					
	N° 1	13.3	2.2	16.6	0.9
	N° 2	10.4	1.3	8.2	1.1
	N° 3	16.3	1.3	27.5	1.0
	N° 4	7.7	1.4	3.1	2.6
	N° 5	8.8	1.6	7.1	1.1
	Average	11.3(3.5)	1.6(0.3)	12.5(9.7)	1.4(0.7)
CRLB					
	N° 1	13.7(2.0)	3.0(0)	14.7(3.0)	1(0)
	N° 2	14.0(1.5)	3.0(0)	13.5(1.0)	1(0)
	N° 3	19.8(3.5)	3.0(0)	31.1(15.2)	1(0)
	N° 4	14.5(1.0)	3.0(0)	12.5(0.5)	1(0)
	N° 5	15.8(1.5)	3.5(0.5)	12.7(1.2)	1(0)
	Average	15.5(2.5)	3.0(0)	16.9(8.0)	1(0)

Table 6.6: Results for scanning reproducibility for GABA PRESS TE=105 ms. † Coefficients of variation are displayed ; ‡ indicates the percentage differences and that the short reproducibility has been performed with repositioning.

Reproducibility	GABA (σ (%))	Glu (σ (%))	Gln (σ (%))	NAA (σ (%))
Short[†]	11.3(3.5)	1.6(0.3)	12.5(9.7)	1.4(0.7)
Short with repo[‡]	11.3(10.9)	3.8(2.3)	-	2.9(1.5)
Long[†]	11.9(5.9)	6.9(3.0)	26.5(2.3)	2.3(0.5)
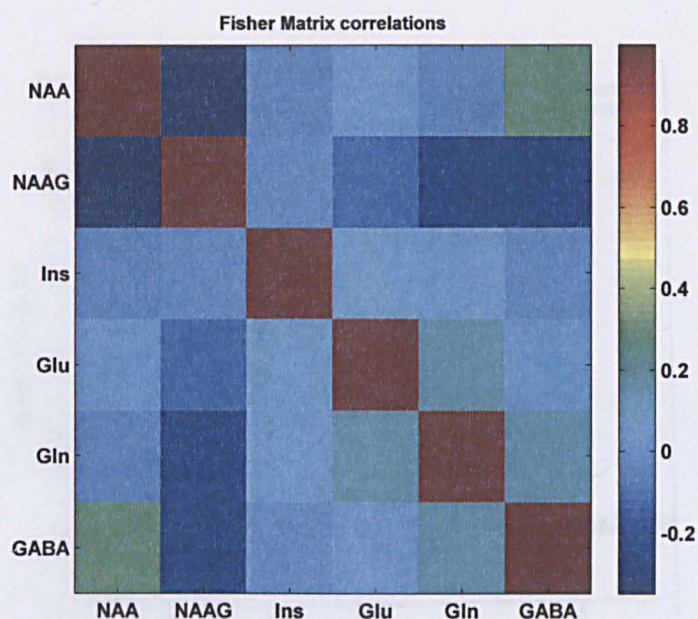
(a) Total NAAG basis
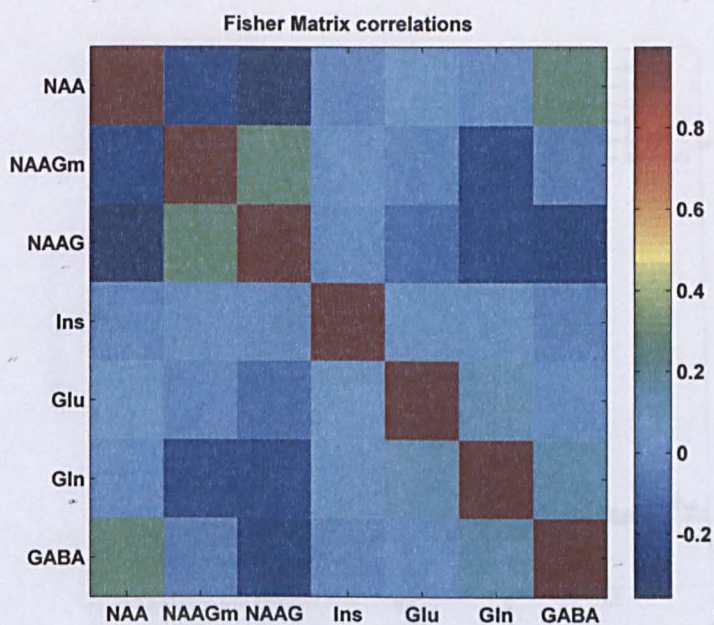
(b) Split NAAG basis

Figure 6.6: Fisher theorical correlation values for coupled metabolites for the two basis datasets used. GABA is poorly correlated with the NAAG multiplets.
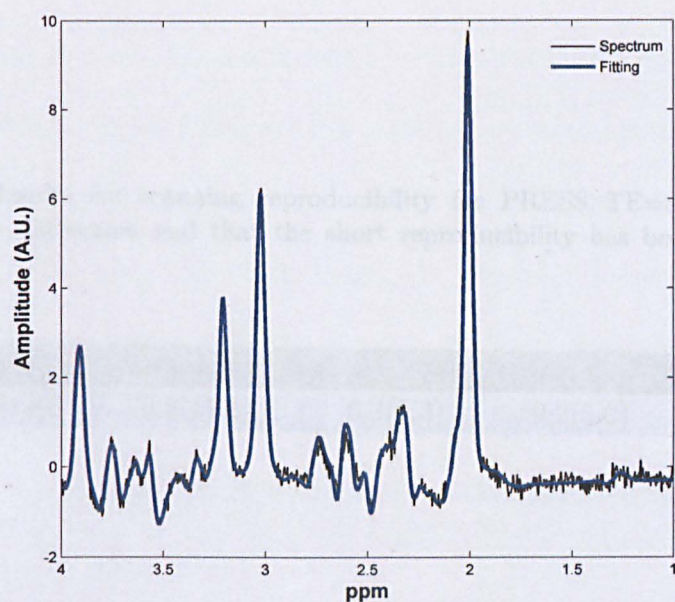
(a) LCModel fitting tor the entire spectrum
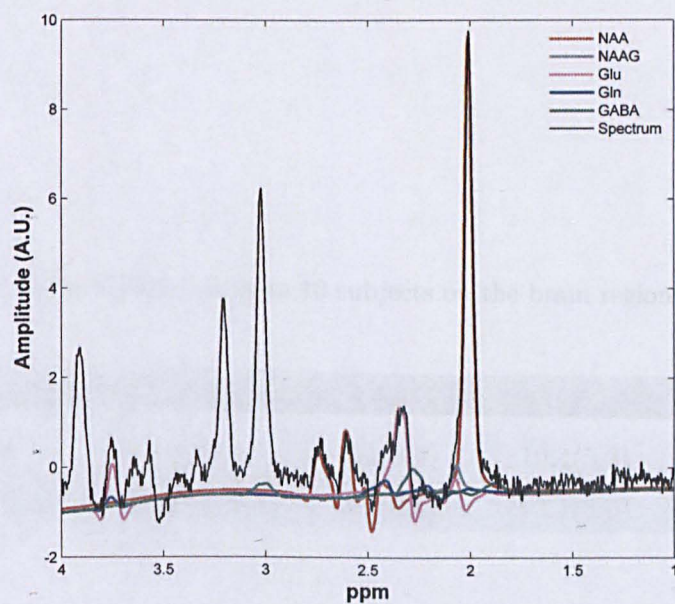
(b) Major metabolites fit

Figure 6.7: Example for the fits for the entire spectrum and the single metabolites' components.

Table 6.7: Results for scanning reproducibility for PRESS TE=80 ms. ‡ indicates
the percentage differences and that the short reproducibility has been performed with
repositioning.

Reproducibility	GABA (σ (%))	Glu (σ (%))	Gln (σ (%))	NAA (σ (%))
Short with repo‡	20.9(17.1)	5.3(2.3)	9.2(5.0)	2.8(1.7)

Table 6.8: Mean CRLB values on 10 subjects on the brain regions considered.

Brain area	GABA (σ (%))	Glu (σ (%))	Gln (σ (%))	NAA (σ (%))
Precuneus	15.3(2.6)	3.1(0.4)	19.4(5.3)	1.4(0.5)
Prefrontal cortex	14.9(3.2)	3.2(0.4)	13.1(3.0)	1.2(0.4)

6.5   Discussion

The *in vitro* results showed a good agreement between the known concentration and the estimated values. However, only the GABA-NAA ratio was compared among sequences rather than the absolute concentration, hence the results on the bias include the errors coming from the NAA estimate. Furthermore, the phantom does not contain creatine compounds thus making easier to fit the peaks at 3.0 ppm since they are not obscured by the Cre singlet. However, the *in vitro* test aimed indeed to prove an improved accuracy by using the GABA-optimised PRESS compared to two other sequences rather than to provide an absolute accuracy.

In light of the discussion in the chapter 3, the comparison between CVs and the CRLBs in the case of the short term reproducibility gives evidence of good agreement between them (case **A**). That is also better for the singlet (NAA) than for coupled metabolites.

The bias has been also tested for NAAG inclusion in the GABA fitting. The values for ADR and RDR give information about the error on the GABA estimate due to erroneously fitted NAAG. In fact, as expected, the estimated NAAG concentrations obtained using a split basis set are much higher than those present in literature (*Govindaraju et al.* [2000], *Edden et al.* [2007]). This means that an optimum fitting and consequently the NAAG real concentration in healthy volunteers would not exceed the value obtained with split basis set. Hence, the ADR reporting only 4% of variations by changing the basis sets could be considered as an upper limit of the error. In addition, focusing on RDR, only the 2% of the possible NAAG variability in concentration becomes variability in the

GABA concentration thus leading to the conclusion that the error on GABA is small even though NAAG is invisible to the fitting.

The same conclusion can be reached from a different perspective, by considering the theoretical correlation values coming from the Fisher matrix. The correlation between NAAG multiplet and GABA are low and show no strong dependence.

The three cases of reproducibility showed a similar mean value for GABA but a different variability: the repositioning and the different method of CV computation might likely cause the difference in the standard deviations. It is also quite visible that the GABA optimized sequence does not perform as well as **PRESS80** for Gln quantification. The study lacks of a statistical test to compute differences in CVs between the two sequences.

Importantly, the voxel size in our study was smaller (15.6 mL) compared to other reliability studies using MEGA PRESS where voxel sizes of 22.5 mL (*Bogner et al.* [2010]) and 27.0 mL (*Evans et al.* [2010]) were used. The sequence does not provide a sufficiently good fitting for Gln, but an robust value for the Glu is attainable: that is not surprising as the Gln and Glu do not show two separate peaks at a careful visual inspection. However, some limitation of the study needs to be stated: firstly, the brain regions tested are commonly areas where the shimming is known to be good and no test was performed on other brain areas; the voxel size was set large enough because a smaller voxel could not provide sufficient signal to detect GABA; given that, careful acquisition is needed to keep the spectrum linewidth under 13Hz and performing a good shimming across the large voxel. Interestingly, the NAAG does not affect the the GABA fitting but brings a

small error in the case that it is not well resolved and distinct from the NAA. On the other hand, the Gln concentration was affected by NAAG thus leading again to conclude that this TE is not specifically tailored for Gln. In addition, similarly to what can be stated about MEGA-PRESS, the sequence is optimized in healthy volunteers and was not tested for robustness on diseases where a decrease in GABA is expected and then its concentration might go below the actual detection level of the sequence; conversely, the values obtained with the corresponding standard deviations provide sufficient information about the number of subjects to be included in a study. Also, compared to MEGA-PRESS, the sequence is surely less affected by macromolecules contamination for two reasons: firstly, because of the longer echo time macromolecules' spectrum would be deeply reduced; secondly, the fitting procedure enables to keep into account them much more efficiently and robustly than spectra-difference-based methods which have to deal with more complex acquisition and hence with a less obvious spectra models. In fact, for MEGA-PRESS the GABA peak resulting from the difference between spectra with inversion pulse on and off is usually fitted by a gaussian function thus leading to erroneous inclusion of macromolecules and consequently biasing the results.

6.6 Conclusions

An optimised standard spectroscopy sequence was tested through simulations, *in vitro* and *in vivo* experiments. The method proved to be sufficiently reliable to be used in the clinical practice as a tool to assess variations in GABA concentrations. In the two brain

regions observed, the sequence is robust to be compared with the MEGA PRESS.

7

Implementation of software-based quantification for

two-dimensional MR spectroscopy

7.1 Introduction

The importance of resolving the entire spectrum of metabolites in a single experiment and the chance of attaining a reliable single measurement makes standard proton MR spectroscopy a not-fully efficient tool for clinical research. In fact, one-dimensional proton MR spectroscopy is usually useful for some metabolites generally by exploiting J-editing methods, multiple quantum filters: they may be extremely precise in detecting the metabolite target but not similarly efficient when enlarging the spectroscopic range of interest. On the other hand, the quantification methods currently used rely on spectral fitting techniques which approach the problem solution by modeling analytically spectra or performing spectra simulation. Unfortunately the use of more advanced acquisition methods introduces further complexity to be either modeled or simulated in the spectrum, and coping with that is not always feasible. Beside that, in a 1D spectrum the enormous complexity of the metabolites' models generates solutions which are

not constantly independent but which have a certain degree of interdependency or more specifically correlation. Conversely, in 2D spectroscopy it can be shown that adding a further degree of freedom would reduce the correlation within metabolite concentrations and would increase the robustness of their quantification (*Alexander Fuchs* [2009]).

In general 2D NMR spectroscopy is a powerful and versatile approach which is able to provide information regarding connectivity (*Aue WP* [1976]) and molecular distance (*Macura S* [1980]) and only recently the new and indirect dimensions encoded were indeed recognized improving unambiguous identification of resonances in *in vivo* spectra with signal overlap that may arise from line broadening (*Slotboom et al.* [1998]). In practice, the growing interest for the use of 2D NMR spectroscopy led to the optimisation of fitting techniques for those spectra. A Matlab software package was shown to be capable of discriminating successfully more metabolites by also reducing the correlations arising among them (*Schulte and Boesiger* [2006b]). This approach, similarly to LCModel, makes use of two particular fitting techniques such as linear combination of metabolite spectra in 2D and VARPRO ('variable protection'). Like LCModel it works in the frequency domain and requires of metabolite basis spectra. This keeps the number of parameters very low compared to methods using parameterized fits. However, this algorithm was not able to compute metabolites' T_2 estimates since the T_2 parameters were included in terms of regularization and then forced to be as close as possible to typical *in vivo* values. Moreover, the algorithm has no mechanism to compensate for distortion and produce absolute quantification by internal reference. The values indeed are reported to total Creatine ratio and no eddy current distortion correction is applied by using internal

reference.

Also the entire algorithm is mainly based on a well-known method of minimization, the so-called gradient descent method. Its convergence is considered to be slow since it is only linear and, even though the proximity of the minimum is quickly obtained, it does not guarantee to reach the global minimum. In fact, it is well known that the algorithm can "zigzag" down valleys, performing many iterations to converge. Other than that, an obvious consequence of the algorithm structure is a stronger dependency of the obtained solution on the starting point when comparing it to other minimization algorithms. This could then result in a slow convergence and in a need of an optimum guess of the seed points which is far from being trivial.

The present work aims to take a further step to improve the 2D fitting quantification and create a tool usable in clinical practice. The goal of this implementation is to make the software more independent from the optimal starting points, reducing the numbers of parameters which are constrained and obtaining water-referenced concentrations.

Based on these considerations, a C-based software package is aimed to be implemented for the processing of 2D spectroscopy data in a reasonable processing time.

7.2   Methods

The minimization algorithm distinguishes between liner and non linear parameters. The non linear parameters are searched within a non-linear least-squares algorithm. In particular a Levenberg-Marquardt approach is utilized: such algorithm is considered to have

a quadratic convergence which is defined as:

$$(7.1) \qquad ||x_{k+1} - x_{solution}|| = O(||x_k - x_{solution}||^2)$$

This faster convergence is also due to the elimination of the "zigzag" effects when close to the minimum. The linear parameters are in turn retrieved through methods such as Non Negative Least Square (NNLS). This permits a more robust quantification since no seed points of the linear parameters need to be guessed at the beginning of the fitting routine, and, in addition, the two classes of parameters remain separate. In general, the function to be optimized is:

$$(7.2) \qquad \min_{x \in \Omega} ||\mathbf{Y} - \mathbf{Y(x)}||$$

where $|| \cdot ||$ is the norm under consideration, $\mathbf{Y}$ is the signal to be quantified and $\mathbf{Y(x)}$ is the model function parameterized by the variables $\mathbf{x}$. By applying a variable separation between linear and non-linear equation 7.2 can be rewritten as:

$$(7.3) \qquad \min_{x \in \Omega} ||\mathbf{Y} - \mathbf{\Phi(a)\alpha}||$$

In this case, $\mathbf{\Phi(a)}$ is a matrix formed by basis vectors and depending on non linear variables, whereas $\mathbf{\alpha}$ are the linear parameters which indeed represent the concentrations. Similar as for LCModel, a set of either basis vectors or basis metabolites is used: compared

to analytical basis functions methods, in which the functions are modeled by Gaussians and Lorentzians, this method requires a lower number of parameters and it is more reliable when the real spectrum has several overlapped peaks. This is usually the case of *in vivo* spectra where a non analytical approach is far more robust. Typically the basis can be either acquired or simulated: the acquisition of metabolite spectra from phantoms is typically expensive and time consuming and, beside that, the differences in relaxation and in lineshape distortions between phantom and *in vivo* data can not be completely corrected thus reducing the quantification reliability especially in a J-PRESS experiment. On the contrary, simulations have none of those issues, but have to deal with effects such as chemical shift displacement.

In this work, simulated basis was chosen and, in particular, all metabolites were simulated by Spinevolution (*Veshtort and Griffin* [2006]) with ideal RF pulses and 1Hz linewidth to avoid delta functions which are not realistic. The basis metabolites included were: aspartate (Asp), creatine (Cre), phosphocreatine (PCr), gamma-aminobutyric acid (GABA), glutamine (Gln), glutamate (Glu), myo-inositol (m-Ins), lactate (Lac), N-acetyl-aspartate (NAA), glycerophosphorylcholine (GPC) and phosphorylcholine (PC). Having defined t_1 and t_2 as the proper FID evolution times and a fictitious time (namely the TE), each metabolite of basis is described by a complex matrix $\Upsilon_l(t_1, t_2)$ to which phase adjustment, line broadening, etc. are applied. In general, each basis can be written like:

$$(7.4) \qquad \Phi_l(t_1, t_2; \mathbf{a}_l) = \Upsilon_l(t_1, t_2) exp(j\phi_l) exp(-\beta_l t_2^2 - t_1/T_2^l + 2\pi j f_l t_2)$$

where ϕ_l is the phase adjustment, β_l the line broadening factor, T_2^l the transverse relaxation time and f_l the frequency shift. The total matrix $\boldsymbol{\Phi}(\mathbf{a})$ is then a multidimensional matrix built like:

$$(7.5) \qquad \boldsymbol{\Phi}(\mathbf{a}) = \left[\ \Phi_1(t_1, t_2; \mathbf{a}_1), \quad \Phi_2(t_1, t_2; \mathbf{a}_2), \quad \ldots \quad \Phi_l(t_1, t_2; \mathbf{a}_l) \ \right]$$

Prior to the fitting, the data are processed to account for reference shift, phasing and alignment. Spectra alignment is performed according to the explanation given in appendix A: in order to minimise the number of necessary parameters, an alignment among all the TEs was then required. A single shift parameter for each metabolite and for all TEs was chosen. A first and second order phase correction is performed by an automatic software based on entropy minimization algorithm (*Chen et al.* [2002]). In short, the function to be minimized is an entropy function like:

$$(7.6) \qquad \qquad S = -\sum_j h_j \ln h_j$$

where h_j is the first derivatives of the signal. For spectra showing low SNR, this automatic method would fail and a manual phase adjustment would be required. The reference between basis and actual spectrum is obtained by searching the NAA singlet in the range 1.9-2.1 ppm. In the case of tumour spectra a reference can be chosen using a different singlet if the NAA signal is not present.

7.2.1 Lineshape corrections

The effect of lineshape distortions in a spectrum could result in wrong prediction and estimation of concentrations. In general, those distortions are caused by variations in B_0: eddy currents and diffusion would generate magnetic field inhomogeneities with spatial and temporal dependence, (x, y, z, t). Consequently, two phenomena contribute to deteriorating the quality of the spectrum: firstly a frequency dependent phase shift during the signal readout leading to a phase distortion; secondly signal dephasing during echo formation and data acquisition reducing the SNR. In order to correct these effects, techniques of reference deconvolution are applied to preprocess the data. In particular, the QUECC (*Bartha et al.* [2000]) method was used. In detail, the deconvolution is performed in the time domain and makes use of the reference signal to perform the correction. The actual unsuppressed and suppressed water signals, $S_{water}(t)$ and $S_{metabo}(t)$, can be expressed as

$$(7.7) \qquad S_{water}(t) = d(t) \times S_{water}^{ideal} \qquad S_{metabo}(t) = d(t) \times S_{metabo}^{ideal}$$

where the signals labeled as ideal are those modeled i.e. with Lorentzian functions; the $d(t)$ is an unknown damping factor which generates visible distortions in experimental data. The damping factor can therefore be computed from the unsuppressed water signal and can be used for the correction of the actual signal according to

$$(7.8) \qquad S_{metabo}^{ideal} = \frac{S_{water}^{ideal}}{S_{water}(t)} \times S_{metabo}(t)$$

Dividing by $S_{water}(t)$ has the potential risk to divide by zero which would generate spikes especially at the end of the FID. To overcome this issue, the approach is also combined with a phase subtraction similarly to Klose's work (*Klose U* [1990]). Furthermore, since this approach was not considered to be consistently robust for removing lineshape distortions for all the spectra and since it did not always result in a complete correction, a distortion model was embedded into the fitting (*Soher and Maudsley* [2004]). The model states that phase distortions can be simulated by a time-dependent factor like:

$$(7.9) \qquad \Gamma(t) = e^{-j\vartheta(t)} \qquad with \qquad \vartheta(t) = \sum_n \xi_n e^{-t/T_n^\xi}$$

where $\Gamma(t)$ is the phase correction factor and $\vartheta(t)$ is the actual time-dependent phase. ξ_n and T_n^ξ are the amplitude and the decay factor respectively. Two values of T_n^ξ have been chosen 13 ms and 100 ms. An ideal implementation of this algorithm would involve a number of parameters equal to the number of TEs but this would lead to a very long processing time. In order to overcome this issue, a mono-dimensional fitting is performed prior to the two-dimensional fitting and therefore the effects of phase distortions are separately obtained for each single spectrum. Therefore, the parameter values ξ_n are utilized to modify the basis metabolites before starting the second fitting in the two-dimensional space.

7.2.2   Starting points

The choice of starting points is extremely important in order to obtain a reasonable minimum value and, even though guessing them is feasible for some parameters, it may be not trivial for others. Generally, the shifts and phases are correctly initialized with zero, whereas T_2^* [1] and T_2 initialization is achieved by random processes. Particularly, a Sobol quasi-random sequence (*Sobol I. M.* [1967]) is exploited to randomly extract T_2^* and T_2 from their characteristic range of values. Either for the T_2^* in the one-dimensional or for the T_2 in the two-dimensional fitting procedure, a set of 50 values centred on typical values is chosen. The fitting computes the function to minimize on 100-200 random sets of T_2 values (each set is made of T_2 values, one for each metabolite), and chooses those for which the function has a minimum.

The random approach aims to maximise the coverage of a multidimensional space of parameters avoiding at the same time clusters of points. The use of Sobol sequences ensures this property despite the use of a limited number of points. With this method it is possible to initialise the fitting with only 100 iterations. Figure 7.1 compares the uniformity of the coverage of the space of parameters for two random generator methods, uniform and quasi-random. It is evident that the Sobol quasi-random method produces a more uniform distribution of points.

---

[1] Here we define $T_2^* = \frac{1}{\sqrt{\beta_i}}$

7.2.3   Non Negative Least Squares (NNLS) approach

Linear parameters can be separated from the actual fitting routine by computing the Moore-Penrose pseudoinverse [2] The $\boldsymbol{\alpha}$ values of the equation 7.3 can then be retrieved by computing the pseudoinverse of $\boldsymbol{\Phi(a)}$, $\boldsymbol{\Phi(a)}^+$:

$$(7.11) \qquad\qquad \boldsymbol{\alpha} = \mathbf{Y}\boldsymbol{\Phi(a)}^+$$

However, since concentrations have to be positive, and the previous method does not guarantee the positivity of the parameters to be determined, the problem to be solved becomes a constrained problem like:

$$(7.12) \qquad\qquad \min_{a \in \Omega} ||\mathbf{Y} - \boldsymbol{\Phi(a)}\boldsymbol{\alpha}|| \quad with \quad \alpha_j \geq 0$$

This is a well-known Non Negative Least Squares problem. In order to solve such problem, we used an algorithm implemented for the first time by Lawson and Hanson (*Lawson and Hanson* [1995]). It has been proved that the algorithm must converge fully after a finite number of iterations and hence it can be considered optimal to be included into the function which has to be minimized. For completeness, the method's explanation is

---

[2]The pseudoinverse is defined and unique for all matrices whose entries are real or complex numbers. It can be computed using the singular value decomposition.

$$(7.10) \qquad AA^+A = A \quad A^+AA^+ = A^+ \quad (AA^+)^* = AA^+ \quad (A^+A)^* = A^+A$$

Here M* is the Hermitian transpose of a matrix M. For matrices whose elements are real numbers instead of complex numbers, $\mathbf{M}^* = M^T$.

reported in appendix C.

7.2.4   Overview of the algorithm

Schematically, the procedure can be subdivided into the following steps, also graphically represented in figure 7.2:

1) Pre-processing involving alignment, phase adjustment, reference deconvolution.

2) Starting one-dimensional fitting to estimate distortion parameters:

   A Initializing parameters such as shifts, phases and distortions' amplitudes at zero;

   B Running 100 or 200 function computations on random input of T_2^* values from a quasi-random procedure. Choice of the best T_2^* which provides the least value for the function 7.2.

   C Performing the function minimization based on the Levenberg-Marquardt algorithm.

3) Applying lineshape distortions to the basis datasets.

4) Starting two-dimensional fitting:

   A Initializing parameters such as shifts and phases at zero; T_2^* values are initialized at the mean values coming from the previous fitting.

   B Running 100 or 200 function computations on random input of T_2 values from a quasi-random procedure. Choice of the best T_2 which provide the least value for the function 7.2.

    C Performing the function minimization based on the Levenberg-Marquardt algorithm.

5) Water amplitude computation.

6) Results.
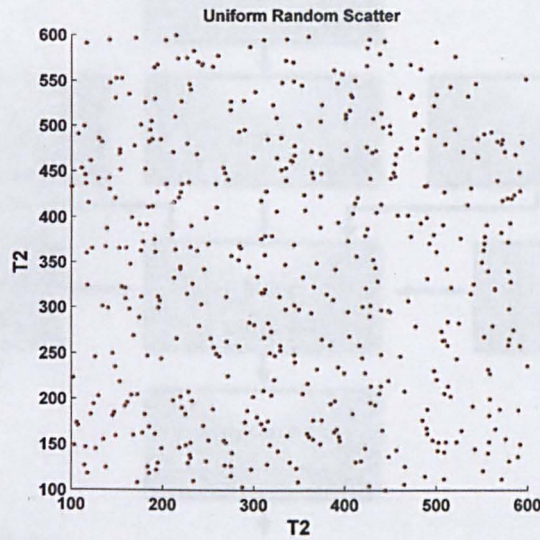
(a)
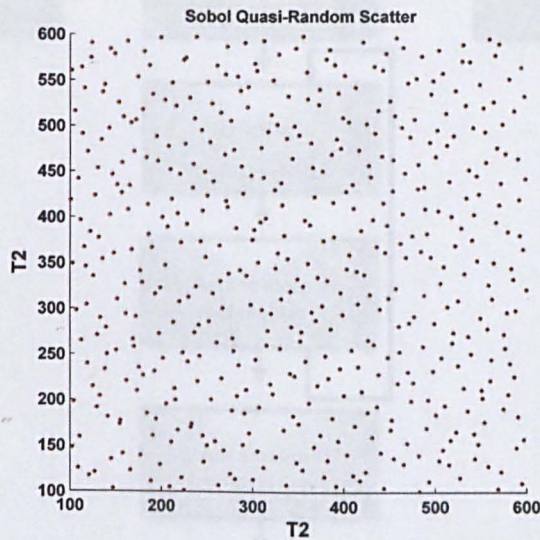
(b)

Figure 7.1: The uniform random sequence vs the Sobol quasi-random sequence used to initialize the T_2 values. The quasi-random method produces a better uniformity compared to the other method. This uniformity increases the chances of guessing the right starting values.

Figure 7.2: Schematic flow chart representing the steps of the 2D fitting procedure, more details are given in the text. The 2D fitting is repeated three times adding new metabolites on each loop.

7.3   Scanning sequences and materials

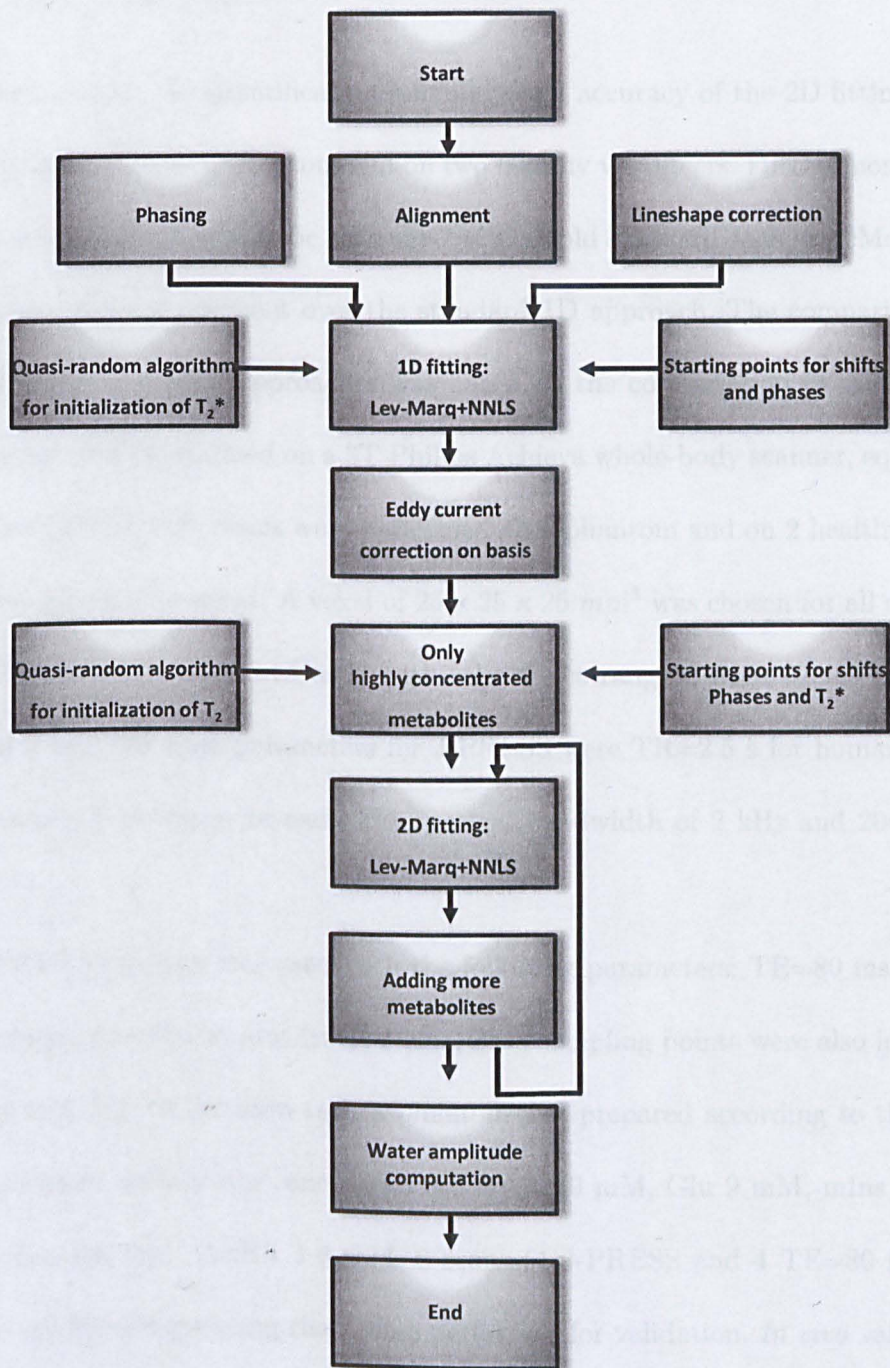In order to assess the quantification reliability and accuracy of the 2D fitting approach, we performed tests on a phantom and on two healthy volunteers. Furthermore, the quantification accuracy needed to be compared with a gold standard such as LcModel in order to test also the improvement over the standard 1D approach. The comparison and the quality control for both approaches was based on the computation of the CRLBs. All experiments were performed on a 3T Philips Achieva whole-body scanner, equipped with 8 channel SENSE coil. Scans were performed on a phantom and on 2 healthy volunteers who gave informed consent. A voxel of $25 \times 25 \times 25$ mm^3 was chosen for all acquisitions.

A J-PRESS sequence was used with echo times ranging from 32 ms to 212 ms in steps of 2 ms. The used parameters for J-PRESS were TR=2.5 s for humans and 4.0 s for phantom, 8 averages for each TE, spectral bandwidth of 2 kHz and 2048 sampling points.

A PRESS sequence was used with the following parameters: TE=80 ms, TR=2.5 s, 128 averages, spectral bandwidth of 2 kHz, 2048 sampling points were also included into the protocol. For the *in vitro* test, a phantom was prepared according to the following standard brain metabolites'concentrations: NAA 10 mM, Glu 9 mM, mIns 6 mM, Gln 4 mM, Lac 0.6 mM, GABA 1.6 mM. 8 scans (4 J-PRESS and 4 TE=80 ms PRESS) with no repositioning among them were performed for validation. *In vivo* validation was performed by analysing the data from 2 healthy volunteers. Both JPRESS and PRESS spectra were acquired for cross-validation with LCModel.

7.4 Results

The major fitted components of an *in vivo* spectrum are displayed in the figure 7.3.

The comparison between the estimates of the phantom concentrations in LCModel and in the two-dimensional fitting are shown in Table 7.1: the CRLBs and percentage standard deviations are reported as well. The results for the *in vivo* quantifications on the two healthy volunteers are described in table 7.2. Values for the percentage standard deviation smaller than 10% (except for Lac) have been reached with the 2D fitting procedure for *in vitro* test. The *in vivo* tests were able to show CRLBs lower than LCModel's but no further improvement was attained from the two-dimensional fitting compared to LCModel's fitting.

Table 7.1: Results for *in vitro* quantification: two and one-dimensional spectra are acquired on a phantom 4 times. Inter-scan variability (SD), CRLB and concentrations are displayed comparing the values for two-dimensional fitting vs LCModel.

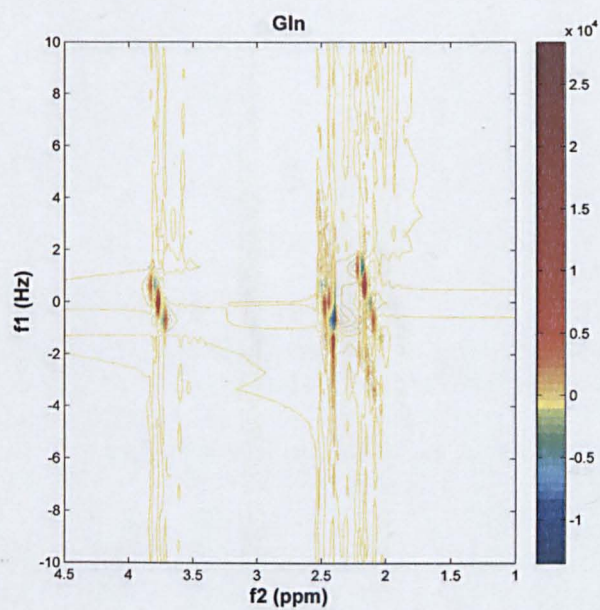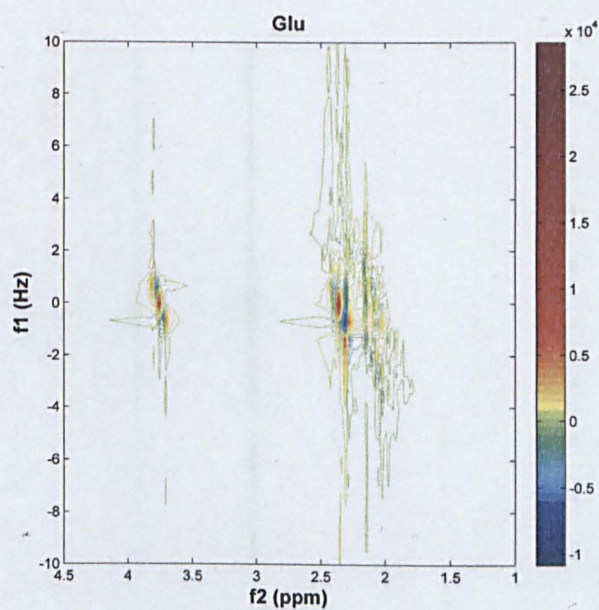| metabolite	Real Conc.	2D fitting			LCModel		
		Conc.	CRLB (%)	SD (%)	Conc.	CRLB	SD (%)
NAA	10 mM	10.5	0.7±0.2	0.9	10.5	1.1±0.2	1.1
Glu	9 mM	9.5	4.7±0.5	1.2	6.5	6.0±0.0	1.2
Gln	4 mM	3.4	6.8±1.7	7.3	3.0	10.0±0.9	9.3
mIns	6 mM	5.7	2.9±1.3	3.1	4.2	8.0±1.6	3.3
GABA	1.6 mM	1.8	10.2±1.4	9.1	1.5	14.0±1.6	11.4
Lac	0.6 mM	1.6	21.0±3.7	16.3	0.6	35.2±7.2	19.4
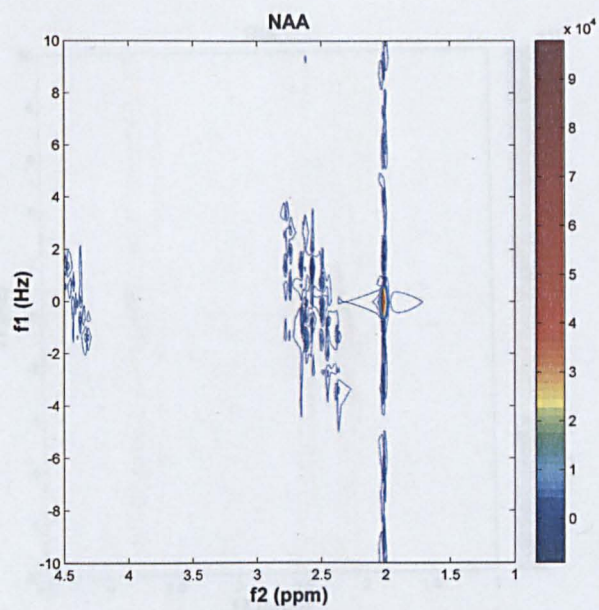
(a) NAA
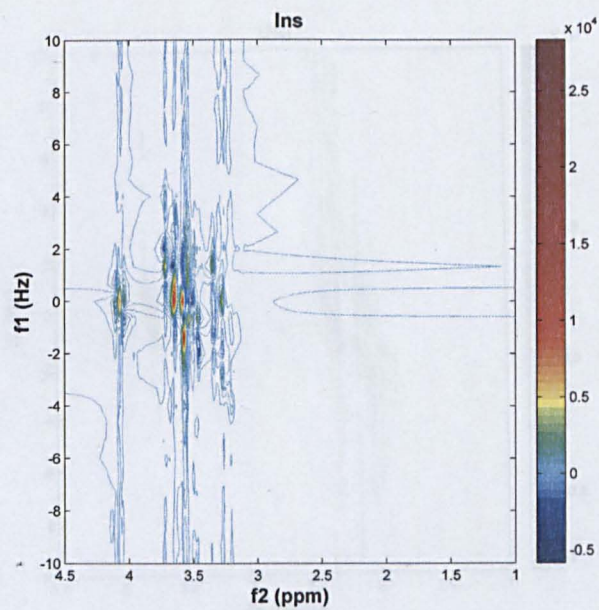
(b) Ins

Figure 7.3: Selected metabolite spectra as fitted to an healthy volunteer spectrum.
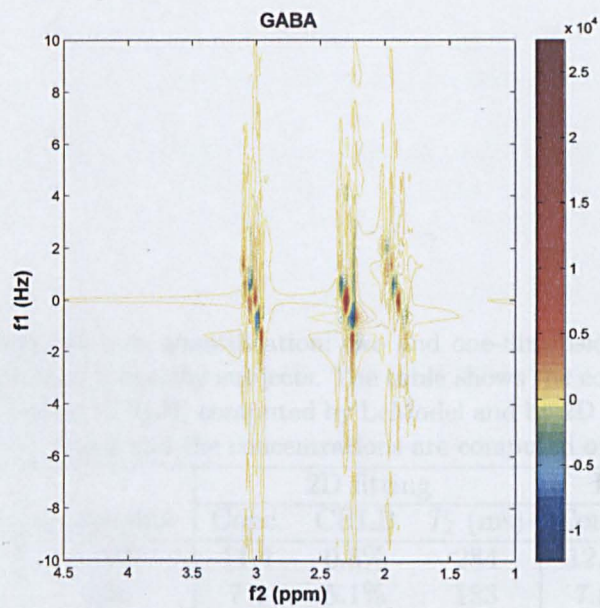
(a) Gln

(b) Glu

Figure 7.3: Selected metabolite spectra as fitted to an healthy volunteer spectrum.

(a) GABA
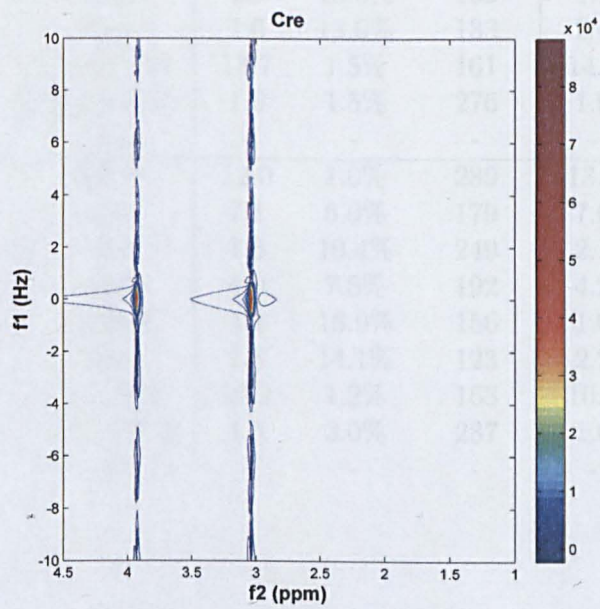
(b) Cre

Figure 7.3: Selected metabolite spectra as fitted to an healthy volunteer spectrum.

Table 7.2: Results for *in vivo* quantification: two and one-dimensional spectra acquired on the prefrontal cortex of 2 healthy subjects. The table shows the concentrations and the Cramer Rao Lower Bound (CRLB) computed by LcModel and by 2D fitting. Besides, T_2 in ms are displayed. † T_2 values and the concentrations are computed on the 3.03 ppm peak.

volunteer	metabolite	2D fitting			LcModel	
		Conc.	CRLB	T_2 (ms)	Conc.	CRLB
1	NAA	11.4	0.5%	284	12.9	2%
	Glu	7.4	5.1%	183	7.8	6%
	Gln	1.8	9.3%	226	2.0	12%
	mIns	3.9	7%	178	4.6	6%
	GABA	1.3	15.3%	132	1.1	24%
	Asp	1.6	13.0%	133	2.4	12%
	Cre+PCr†	13.7	1.5%	161	14.2	3%
	GPC+PCh	1.6	1.5%	276	1.9	3%
	Lac	-	-	-	-	-
2	NAA	12.0	1.0%	289	13.2	2%
	Glu	7.1	6.0%	179	7.6	6%
	Gln	1.8	10.4%	249	2.1	12%
	mIns	4.0	7.5%	192	4.2	6%
	GABA	1.1	16.9%	156	1.0	25%
	Asp	1.8	14.1%	123	2.2	12%
	Cre+PCr	10.2	1.2%	163	10.1	3%
	GPC+PCh	1.5	2.0%	287	1.6	3%
	Lac	-	-	-	-	-

7.5   Discussion

A good accuracy was reached with the 2D fitting procedure for *in vitro* and *in vivo* applications. Such accuracy was tested on a phantom and compared to LCModel's. The comparison was performed on the CRLB, inter-scan variability and concentrations (the last two only for *in vitro* data) for both quantifications. Absolute values of the inter scan variability on 4 measurements are very low, since no repositioning was made among each scan, but, interestingly, they were smaller in the 2D fitting compared to LCModel's. In addition, concentration estimates have been shown to reproduce more accurately real values present *in vitro*. These estimates do not have concentration units, but are provided in arbitrary unit. Nevertheless, the gain in accuracy is interpretable also as an effect of the duplex correction on the T_2, for metabolites and water, which is not implicitly applied in 1D. Reduced spectral overlap must be considered a further reason for that improvement. Looking at CRLBs, it is conceivable that ameliorated separation among peaks has an effect on their theoretical correlations which, in turn, have repercussions on CRLB. In the *in vivo* data most of the metabolites are found to have smaller theoretical standard deviations compared to LCModel: importantly, three coupled metabolites appeared to have an important improvement, especially for GABA, which has a value below 20%. On the other hand, Aspartate and Myo-Inositol have shown estimates slightly larger than the one-dimensional counterpart. Probably, the lack of terms that include macromolecules and lipids might confound the fitting and produce a worse quantification. Also, no improvement was observed in Lactate quantification and similarly to LCModel an unreliable fitting is obtained. The reasons for that depend not only on the absence of

terms including the baseline, but also on the strong effect that chemical shift displacement at 3T has on the Lactate spectrum, which is well described in literature (*Edden et al.* [2006]). The T_2 estimates for some of the metabolites are in agreement with what is available in literature at 3T: comparison can be done among singlets such as NAA, Cho and Cre (*Träber et al.* [2004], *Mlynárik et al.* [2001]) and for Glu (*Choi et al.* [2006]). Of particular importance is the Glu estimate when compared to the value of a further estimate at 3T (*Choi et al.* [2006]).

An important subroutine, NNLS, is used to separate linear and non-linear variables and to have constraints on the concentrations in order to have them positive.

In comparison, ProFit (*Schulte and Boesiger* [2006b]) builds functions which compute the concentrations and which depend on the non-linear variables. Such functions are then constrained to be positive by applying techniques such as Lagrange multipliers: in particular, the method tries to avoid values of the non-linear variables that make the concentrations negative. In other words, the minimization algorithm plays with two sets of constraints; those which are based on a range of values set in real-terms, and those which are based on range of values set in abstract-terms and created only to obtain positive concentrations. Therefore, the software might reduce the parameters' space too much and it might be the case that the found minimum is not the real minimum.

The NNLS algorithm overcomes this issue and constrains the concentrations as values rather than as functions. No further constraint is set for parameters different from the concentrations. The second subroutine, the quasi-random initialization, implements the need of having a feasible starting point for strongly non-linear parameters which are

practically difficult to initialize. This avoids to introduce regularizors into the fitting and guess typical values which are mainly known. The last subroutine, the 1D fitting prior to the main routine, is useful to have lineshape corrections among different TEs and to permit a reasonable starting point of linewidths. Furthermore, the basis-dataset is simulated with ideal pulses and no chemical shift displacement effect is introduced: some metabolites such as lactate do not have a good accordance through all TEs. An important and additional feature to be added is including lipids and macromolecules into the fitting similarly to what another software package does (Tarquin, *Wilson et al.* [2010]) by including B-spline functions modeling the baseline into NNLS algorithm to retrieve the linear factors. Typical running times are around 12 minutes due mainly to Monte Carlo-like search for minima. As the processing time has an enormous importance in the clinical practice, further improvements of the method here exposed would aim to decrease the processing time further to meet more stringing requirements.

Since the initialization algorithm is based on random processes, it might provide different starting points for each run. Its robustness and the stability remain to be investigated. In fact, Monte Carlo-like algorithms are extremely powerful for a global optimization but might have the just cited drawback. Consequently, this issue needs to be tested and appropriately addressed. A further consideration must be made about the lower values of the CRLBs compared to LCModel. Like Profit, these small values might be due to the absence of baseline rather than a optimum fitting. In fact, the baseline was found to be correlated to many metabolites thus increasing the values of the theoretical standard deviation (*Ratiney et al.* [2004, 2005]). It is also true that the correlations

among metabolites are reduced (*Alexander Fuchs* [2009]) and, as consequence of these two considerations, a clear interpretation is not possible. After having included a term taking into account the baseline, additional studies will be necessary to test whether the baseline has a so important influence on CRLBs for two-dimensional fitting.

7.6   Conclusions

A software package was implemented to accurately fit spectra acquired with J-PRESS sequence. The algorithm relies upon three main subroutines which make it different from another similar software package (*Schulte and Boesiger* [2006b]) and lead it to be robust enough to estimate T_2 without needing to constrain and force them to typical values.

portant... (faded text)

8

My PhD work has been mainly focused on the optimization and applications on schizophrenia and animal model of schizophrenia of Magnetic Resonance Spectroscopy *in vivo*. Three interesting and original findings have been reached in this work regarding its translational part. Increased Aspartate level in schizophrenia patients compared to controls thus showing that the hypothesized high glutamatergic activity is visible via a metabolite coupled to Glutamate and belonging to an important shuttle, the Aspartate-Malate shuttle. The correlation between Glutamate concentrations and induced theta activity present in healthy volunteers is dissociated in Schizophrenic patients. In addition, the study on animal model of schizophrenia showed a selective GABA decrease only in isolates rats. A relevant aspect to be studied in the future will be searching confirmations of increased aspartate either with a new aspartate optimized protocol or by moving to higher field. A short TE sequence on 7T platform would strengthen the reliability of the detected concentrations and would provide the important information coming from GABA. GABA in schizophrenia is indeed a still unexplored territory and it would be of extreme interest using the sequence optimized for GABA to be able to detect this im-

portant metabolite. Reliable Aspartate measurement would also help to study another important topic in schizophrenia such as D-Aspartate which is nowadays becoming very crucial topic in schizophrenia.

Grounded on the same concept as used for GABA optimized sequence, simulations would be performed to find out potential parameters which would permit to obtain a reliable quantification of Glutathione and Taurine.

The great potential of the 2D approach needs to be confirmed increasing the number of spectra such that accuracy and comparison with LcModel might be better tested. Also, features such as automatic alignment, spectra referencing, which now work as separate pieces of software, will need to be incorporated into the main 2D fitting code. Interestingly, we will adapt this software for quantification of diffusion weighted spectroscopy where the echo time variation in the fitting will be replaced by the b value.

Implementation of Matlab-based code for automatic spectra realignment

During acquisition, the increase in the temperature of the system leads to a natural drift of the main magnetic field B_0 and consequently of the frequency offset ω_0. There is an algorithm on the 3T Philips Achieva platform which is able, while acquiring the unsuppressed water, to stabilize this drift, but it is not always optimal and requires extra scanning time. Unless unsuppressed water is needed, that might be skipped. A consequence of the drift is a smearing out of the peak once the whole acquisition is averaged. Some of the studies described here used dynamic scanning for the acquisition and offline aligning was performed to reduce such line broadening effect.

The code is written in Matlab and requires only a user input of the target (i.e. NAA peak) to which all spectra will be aligned. In particular, the edges of one singlet. The aligning method relies upon the cross correlation theory of two different signals. The cross-correlation is similar in nature to the convolution of two functions. Whereas convolution involves reversing a signal, shifting it and then multiplying by another signal, correlation only implies shifting it and multiplying without reversing the signal. There-

fore, the cross-correlation is a measure of similarity and hence the proximity of alignment of two signals as a function of a time-lag. For two continuous signals, $\mathcal{S}(t)$ and $\mathcal{Z}(t)$ the cross correlation is defined as:

$$(A.1) \qquad \mathcal{G}(t) \overset{\text{def}}{=} \int_{-\infty}^{\infty} \mathcal{S}^*(\tau) \, \mathcal{Z}(t+\tau) \, d\tau$$

which in a discrete space becomes:

$$(A.2) \qquad \mathcal{G}(t) \overset{\text{def}}{=} \frac{1}{N-|m|} \sum_{n=0}^{N-1-|m|} \mathcal{S}^*(n) * \mathcal{Z}(n+|m|)$$

As the convolution, the cross correlation is extremely expensive in term of processing time and this is prohibitive when a large data set needs to processed. For this reason, a different approach is usually exploited. The propriety of Fourier Transform can be useful for such a goal. Defining $\widehat{\mathcal{X}}(f)$ the Fourier Transform of $\mathcal{X}(f)$ as follows

$$(A.3) \qquad \widehat{\mathcal{X}}(f) = \mathfrak{F}(\mathcal{X}(t)) = \int_{-\infty}^{+\infty} \mathcal{X}(t) \, e^{-2\pi i t f} \, dx,$$

it is easy to prove that the A.1 is a simple product in the reciprocal space:

$$(A.4) \qquad \widehat{\mathcal{G}}(f) = \mathfrak{F}(\mathcal{G}(t)) = \widehat{\mathcal{S}}(f) * \widehat{\mathcal{Z}}(f)$$

providing the cross correlation function by performing the inverse Fourier Transform:

$$(A.5) \qquad \mathcal{G}(t) = \mathfrak{F}^{-1}(\widehat{\mathcal{G}}(f)) = \mathfrak{F}^{-1}(\widehat{\mathcal{S}}(f) * \widehat{\mathcal{Z}}(f))$$

The algorithm then performs few steps in order to align the spectra. The real and imaginary part of the FID signal are imported as text files. Since the algorithm is based on cross correlation, it relies upon the shift in the number of points of two signals rather than their frequency shift. To this end, as you can see in figure A.1, three more steps are undertaken:

- The FIDs are zero filled in order to result in 32K sample points. This huge number is necessary to obtain a more precise and fine frequency shift in the following step.

- The 32K FID signal is Fourier transformed.

- Operator input of the two extremes of a singlet: n_{left} and n_{right}.

The number of shifting points is therefore computed by calculating the maximum of the cross correlation function of the target signal versus the signal to be aligned between n_{left} and n_{right}. This discrete output h_{shift} describing the discrepancy in number of points between the two signal is reported into the time domain by:

$$(A.6) \qquad \mathcal{S}_{shift}(t) = \mathcal{S}_0(t) * e^{-ith_{shift}}$$
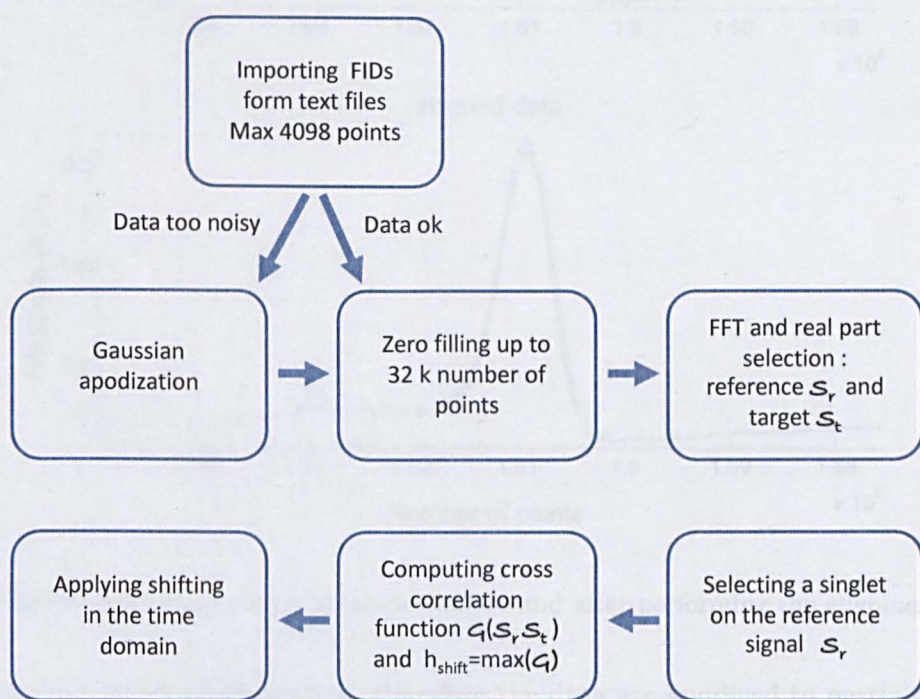
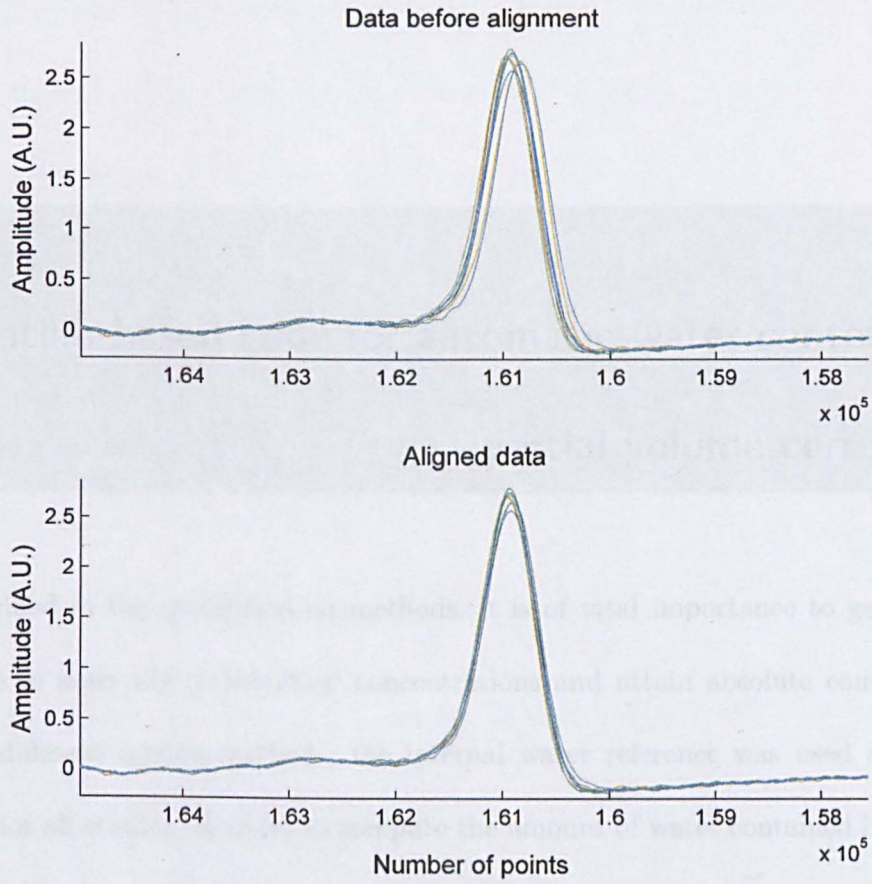**Figure A.1:** The flow chart reproduces the steps made by the algorithm.

Figure A.2: Example of 10 spectra before and after performing the alignment.

Noisy data are difficult to align, therefore the data are apodized to partially remove the noise and make the cross correlation computation more robust. An example of the software performance on 10 spectra is shown in figure A.2.

Matlab-based code for automatic water content and

partial volume corrections

As described in the quantification methods, it is of vital importance to get a reliable reference to scale the metabolites' concentrations and attain absolute concentrations. Among different scaling methods, the internal water reference was used as standard method for all studies. In order to compute the amount of water contained in the voxel, the spectroscopy voxel has to be positioned on the image. The following description explains how the code works and the outputs.

The software was coded in Matlab: DICOMs are taken as input files and binary mask in Analyze format are saved as output. A text file with the voxel vertices' coordinates in the image frame system is also saved. The image geometrical parameters and the spectroscopy voxel in the scanner coordinate system (see figure B.1) are then read from the DICOM header:

1) pixel size;

2) off centre values indicating the centre of the entire image stacks:

(a) Anterior-Posterior (AP) from the tag *Private 2005 1078*;

(b) Right-Left (RL) from the tag *Private 2005 1079*;

(c) Foot-Head (FH) from the tag *Private 2005 107a*;

3) The Euler angles of the unit vector $\underline{t}$, $\underline{v}$, $\underline{d}$ (see figures B.2 and B.3) in an image, imported from the *ImageOrientationPatient* tag;

4) The coordinates of the upper left pixel (see figure B.2) for each slice, imported from the *ImagePositionPatient* tag;

5) N: Number of Slices from the tag *NumberOfFrames*;

6) Width and Height, respectively number of rows and columns from the similarly named tags;

7) Main frequency value from the *TransmitterFrequency*.

Similarly, the voxel geometrical information was imported from the Dicom files. A feature to import the geometrical information from the *spar* file is available and in that case the AP and RL voxel coordinates need to be flipped as the coordinate system is inverted compared to the DICOM file. Therefore, the geometrical data are the following:

1) the voxel size *sizeap sizecc sizelr* respectively from the tags *Private 2005 1057*, *Private 2005 1058*, *Private 2005 1059*;

2) offcentre values *offap offcc offlr* indicating the voxel centre respectively from the tags *Private 2005 105a*, *Private 2005 105b*, *Private 2005 105c*;
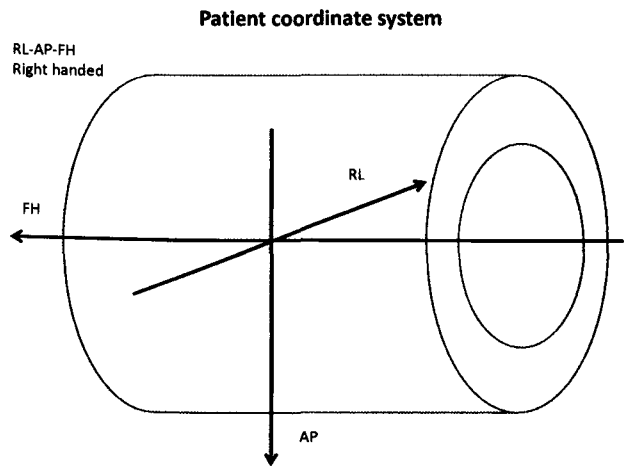
Patient coordinate system

Figure B.1: The right handed coordinate system in the magnet: the magnet isocentre is determined as intersection of the three orthogonal axis.
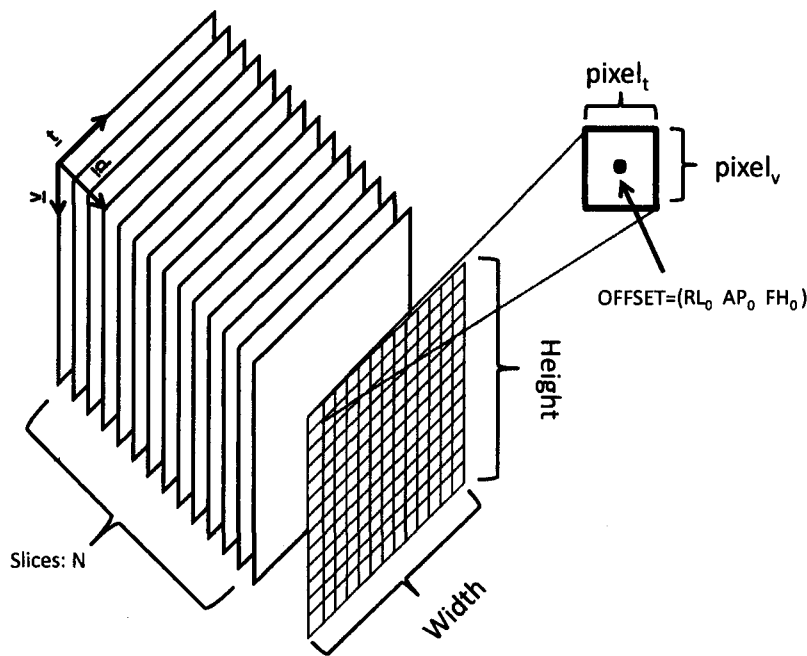
Figure B.2: Pixel size and offset value for each slice were utilized to compute the geometrical intersections between voxel and image planes.
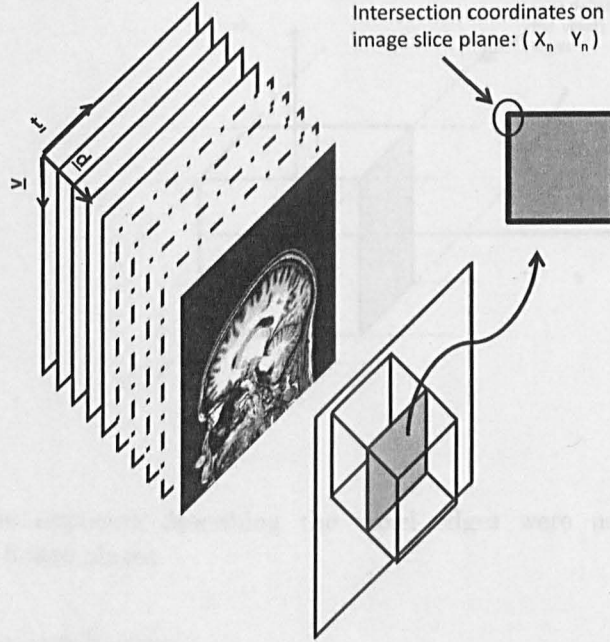
Figure B.3: The square edges were obtained from the intersection between voxel segments and image planes. The image versors were exploited to determinate image stack orientation.

3) the angulation values by which the voxel is rotated: *angleap anglecc anglelr* respectively from the tags *Private 2005 1054*, *Private 2005 1055*, *Private 2005 1056*.

The voxel is then built as a set of line equations defining the edges of the voxel, see figure B.4.

If we define the versors in the scanner coordinate system as follows:

$$(B.1) \qquad \widehat{x}_1 = \widehat{i} = \begin{bmatrix} 1 \\ 0 \\ 0 \end{bmatrix} \qquad \widehat{x}_2 = \widehat{j} = \begin{bmatrix} 0 \\ 1 \\ 0 \end{bmatrix} \qquad \widehat{x}_3 = \widehat{k} = \begin{bmatrix} 0 \\ 0 \\ 1 \end{bmatrix}$$
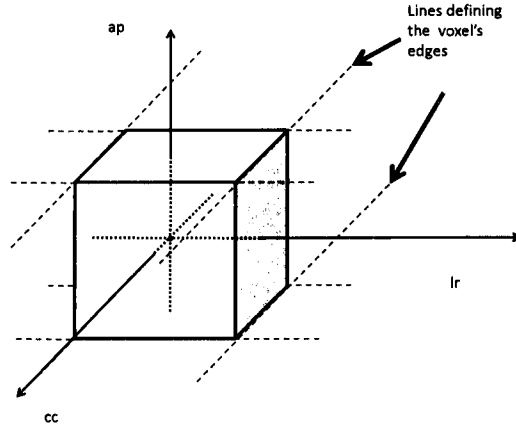
Figure B.4: The segments describing the voxel edges were used to compute the intersections with image planes.

and the position coordinates:

$$\text{(B.2)} \qquad \underline{\mathbf{s}} = \left[\ \pm sizeap/2 \quad \pm sizelr/2 \quad \pm sizecc/2 \ \right]$$

each line can be described through the coordinates of a point on the line $\underline{b}_l$, its direction $\widehat{x}_l$ and its extreme points $\underline{b}_l^- \ \underline{b}_l^+$:

$$\text{(B.3)} \qquad \underline{b}_l = \sum_{n=1}^{3} \underline{\mathbf{s}} \cdot \widehat{x}_m - \underline{\mathbf{s}} \cdot \widehat{x}_l \qquad \underline{b}_l^+ = \underline{b}_l + |\mathbf{s}_l| * \widehat{x}_l \qquad \underline{b}_l^- = \underline{b}_l - |\mathbf{s}_l| * \widehat{x}_l$$

In the same way the image planes were constructed by defining the versor perpendicular to the plane $\underline{d}$ and the coordinates of a point on each plane $B_n = (AP_0, \ RL_0, \ FH_0)_n$ with n=1,2,...N. Before performing the intersection between voxel and planes, the voxel needed to be rotated and translated to adjust the voxel position in a single reference

system, the one from the image. The rotation matrices were defined as:

$$(B.4) \qquad R_{ap} = \begin{bmatrix} 1 & 0 & 0 \\ 0 & \cos(angleap) & -\sin(angleap) \\ 0 & \sin(angleap) & \cos(angleap) \end{bmatrix}$$

$$(B.5) \qquad R_{lr} = \begin{bmatrix} \cos(anglelr) & 0 & \sin(anglelr) \\ 0 & 1 & 0 \\ -\sin(anglelr) & 0 & \cos(anglelr) \end{bmatrix}$$

$$(B.6) \qquad R_{cc} = \begin{bmatrix} \cos(anglecc) & -\sin(anglecc) & 0 \\ \sin(anglecc) & \cos(anglecc) & 0 \\ 0 & 0 & 1 \end{bmatrix}$$

where the total rotation matrix is the product of the previous matrices:

$$(B.7) \qquad R = R_{ap} R_{lr} R_{cc}$$

whereas the translation vector is given by:

$$(B.8) \qquad \vec{T} = \begin{bmatrix} \mathit{offlr} \\ \mathit{offap} \\ \mathit{offcc} \end{bmatrix}$$

The new voxel parameters $\underline{b}'_l, \widehat{x}'_l, \underline{b}_l'^-, \underline{b}_l'^+$ will then be

$$(B.9) \qquad \underline{b}'_l = R\underline{b}_l + \vec{T}; \quad \underline{b}_l'^- = R\underline{b}_l^- + \vec{T}; \quad \underline{b}_l'^+ = R\underline{b}_l^+ + \vec{T}; \quad \widehat{x}'_l = R\widehat{x}_l;$$

The intersections between the planes and the voxel segment lines are then computed. This implies the knowledge of the cross-section of the voxel for each slice and its respective coordinates. The method of the intersection is not very fast but the voxel ROI was primarily meant to be used in Jim software before being used in Analyze format. The creation of binary masks from the coordinates was performed by *poly2mask* Matlab function. Since the use of high field strength combined with PRESS localization determines a quite strong chemical shift displacement, the software computes also binary masks for different metabolites and consequently different chemical shift according to the formula 2.42. Given NAA as reference, the metabolites taken into account were Ins (1.606 ppm[1]), water (2.692 ppm), and Cho (1.171 pm). An example of the displacement computed is in figure B.5.

Corrections for water content and partial volume effect involved the use of bina-

---

[1]The ppm values are calculated by setting NAA singlet peak as zero.
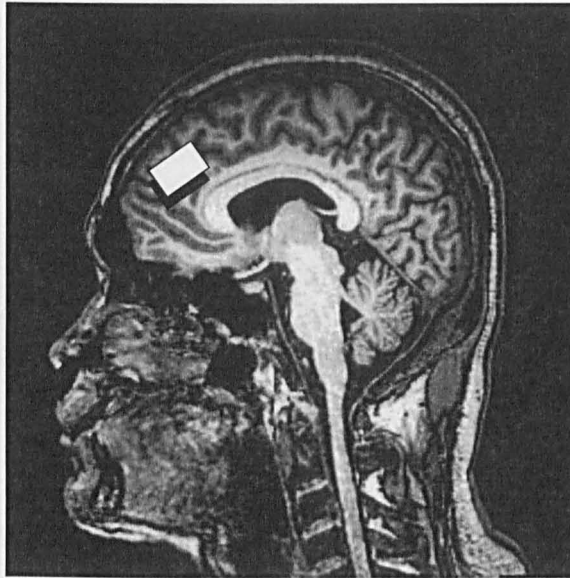
Figure B.5: An example of the localization and the voxel size used for the study regarding schizophrenia disease (see chapter 4). The white box represents NAA localization and the black one represents the water.

ry masks and the segmentation of an MPRAGE acquired to this end. In general the

correction factor for water content in molar units is deduced from the following formula:

$$(B.10) \qquad C_{water} = (WM \times 0.73 + GM \times 0.82 + \mathbf{CSF} \times 0.98) * 55M$$

where WM, GM and CSF are respectively the percentage in the voxel of white matter,

grey matter and cerebrospinal fluid. The voxel under consideration is the one correspond-

ing to water chemical shift. Conversely, partial volume effect is corrected by the NAA

chemical shift voxel and by determining the fraction of WM and GM in that voxel.

C

Non Negative Least Squares (NNLS) algorithm

The NNLS (*Lawson and Hanson* [1995]) algorithm looks for a vector α and its dual vector η that satisfy the Kuhn-Tucker conditions for Problem NNLS. The input data of the algorithm are the integers m and n, the m $\times$ n matrix Φ, and the m-vector $\mathbf{Y}$. The working space used consists of two n-vectors η and β and two subsets P and L of the index set 1, 2, . . . , n. The components of the current vector α with indices from the set L are zero. The components with indices from the set P can take nonzero values. In case this component is nonpositive, then the algorithm will either change its value to a positive one or set it to zero and move its index from P to L. On termination, the vector x contains the solution of Problem NNLS, whereas η contains the dual vector.

In detail, the flow will appear as follows:

1) Starting point: P=$\varnothing$, L=1, 2, . . . , n and α =0;

2) Compute the vector $\eta = \Phi^T (\mathbf{Y} - \Phi(\mathbf{a})\alpha)$ with the current value of α;

3) If L=$\varnothing$ or $\eta_j \leq 0 \; \forall \, j \in L$, then go to step 13;

4) Find an index $l \in L$ such that $\eta_l = \max_{j \in L}\{\eta_j\}$;

5) Move the index 1 from L to P;

6) Define the m × n matrix $\Phi_P = \begin{cases} \text{column j of } \Phi, & \text{if } j \in P \\\\ 0, & \text{if } j \in L \end{cases}$

7) Compute the β as a normal least squares problem:

$$(C.1) \qquad \min \|\mathbf{Y} - \mathbf{\Phi}_P\boldsymbol{\beta}\|$$

8) If $\beta_j > 0 \ \forall \ j \in P$, then set $\alpha=\beta$ and go to Step 2;

9) Find an index q ∈ P such that:

$$(C.2) \qquad \frac{\alpha_q}{\alpha_q - \beta_q} = \min_{j \in L}\left\{\frac{\alpha_j}{\alpha_j - \beta_j} \mid \beta_j \leq 0\right\}$$

10) Set

$$(C.3) \qquad \lambda = \frac{\alpha_q}{\alpha_q - \beta_q}$$

11) Redefine $\alpha = \alpha+\lambda(\beta - \alpha)$

12) Move all indices j ∈ P where $\alpha_j = 0$ from P to L. Go to the Step 8;

13) Terminate the process.

Bibliography

Alexander Fuchs, T. L. P. B., Anke Henning (2009), Ismrm abstract 2406: Comparison of metabolite correlation in 1d and 2d quantitative spectroscopy, in *17th Scientific Meeting and Exibition of ISMRM*.

Aue WP, E. R., Bartholdi E (1976), Two-dimensional spectroscopy. application to nuclear magnetic resonance., *J. Chem. Phys.*, *64*, 2229–2246.

Bartha, R., P. C. Williamson, D. J. Drost, A. Malla, T. J. Carr, L. Cortese, G. Canaran, R. J. Rylett, and R. W. Neufeld (1997), Measurement of glutamate and glutamine in the medial prefrontal cortex of never-treated schizophrenic patients and healthy controls by proton magnetic resonance spectroscopy., *Arch Gen Psychiatry*, *54*(10), 959–965.

Bartha, R., D. J. Drost, R. S. Menon, and P. C. Williamson (2000), Spectroscopic lineshape correction by QUECC: combined QUALITY deconvolution and eddy current correction, *Magn. Reson. Med.*, *44*(4), 641–5.

Bates, A. T., K. A. Kiehl, K. R. Laurens, and P. F. Liddle (2009), Low-frequency eeg oscillations associated with information processing in schizophrenia, *Schizophrenia Research*, *115*(2-3), 222 – 230, doi:DOI: 10.1016/j.schres.2009.09.036.

BECK, L. H., E. D. BRANSOME, A. F. MIRSKY, H. E. ROSVOLD, and I. SARASON (1956), A continuous performance test of brain damage., *J Consult Psychol*, *20*(5), 343–350.

Bernstein, M., K. King, and X. J. Zhou (2004), *Handbook of MRI Pulse Sequences*.

Bianchi, M., K. F. C. Fone, N. Azmi, C. A. Heidbreder, J. J. Hagan, and C. A. Marsden (2006), Isolation rearing induces recognition memory deficits accompanied by cytoskeletal alterations in rat hippocampus., *Eur J Neurosci*, *24*(10), 2894–2902, doi:10.1111/j.1460-9568.2006.05170.x.

Birken, D. L., and W. H. Oldendorf (1989), N-acetyl-l-aspartic acid: a literature review of a compound prominent in 1h-nmr spectroscopic studies of brain, *Neurosci. Biobehav. Rev.*, *13*, 23–31.

Blakely, R. D., and J. T. Coyle (1988), The neurobiology of n-acetylaspartylglutamate., *Int Rev Neurobiol*, *30*, 39–100.

Bogner, W., et al. (2010), In vivo quantification of intracerebral gaba by single-voxel (1)h-mrs-how reproducible are the results?, *Eur J Radiol*, *73*(3), 526–531, doi:10.1016/j.ejrad.2009.01.014.

Bramon, E., S. Rabe-Hesketh, P. Sham, R. M. Murray, and S. Frangou (2004), Meta-analysis of the p300 and p50 waveforms in schizophrenia., *Schizophr Res*, *70*(2-3), 315–329, doi:10.1016/j.schres.2004.01.004.

Bustillo, J. R., L. M. Rowland, P. Mullins, R. Jung, H. Chen, C. Qualls, R. Hammond, W. M. Brooks, and J. Lauriello (2010), 1h-mrs at 4 tesla in minimally treated early schizophrenia., *Mol Psychiatry*, *15*(6), 629–636, doi:10.1038/mp.2009.121.

Carlsson, A., N. Waters, S. Holm-Waters, J. Tedroff, M. Nilsson, and M. L. Carlsson (2001), Interactions between monoamines, glutamate, and gaba in schizophrenia: new evidence., *Annu Rev Pharmacol Toxicol*, *41*, 237–260, doi:10.1146/annurev.pharmtox.41.1.237.

Cavassila, Deval, Huegen, van Ormondt D, and Graveron-Demilly (2000), Cramer-rao bound expressions for parametric estimation of overlapping peaks: influence of prior knowledge, *J Magn Reson*, *143*(2), 311–320, doi:10.1006/jmre.1999.2002.

Cavassila, S., S. Deval, C. Huegen, D. van Ormondt, and D. Graveron-Demilly (2001), Cramér-rao bounds: an evaluation tool for quantitation., *NMR Biomed*, *14*(4), 278–283.

Chang, L., J. Friedman, T. Ernst, K. Zhong, N. D. Tsopelas, and K. Davis (2007), Brain metabolite abnormalities in the white matter of elderly schizophrenic subjects: implication for glial dysfunction., *Biol Psychiatry*, *62*(12), 1396–1404, doi:10.1016/j.biopsych.2007.05.025.

Chen, L., Z. Weng, L. Goh, and M. Garland (2002), An efficient algorithm for automatic phase correction of NMR spectra based on entropy minimization, *J. Magn. Reson.*, *158*, 164–68.

Choi, C., N. J. Coupland, P. P. Bhardwaj, S. Kalra, C. A. Casault, K. Reid, and P. S. Allen (2006), T2 measurement and quantification of glutamate in human brain in vivo., *Magn Reson Med*, *56*(5), 971–977, doi:10.1002/mrm.21055.

Cilia, J., C. Reavill, J. J. Hagan, and D. N. Jones (2001), Long-term evaluation of isolation-rearing induced prepulse inhibition deficits in rats., *Psychopharmacology (Berl)*, *156*(2-3), 327–337.

Cilia, J., P. D. Hatcher, C. Reavill, and D. N. C. Jones (2005), Long-term evaluation of isolation-rearing induced prepulse inhibition deficits in rats: an update., *Psychopharmacology (Berl)*, *180*(1), 57–62, doi:10.1007/s00213-004-2139-5.

Clark, J. F., A. Doepke, J. A. Filosa, R. L. Wardle, A. Lu, T. J. Meeker, and G. J. Pyne-Geithman (2006), N-acetylaspartate as a reservoir for glutamate., *Med Hypotheses*, *67*(3), 506–512, doi:10.1016/j.mehy.2006.02.047.

Coyle, J. T. (2004), The gaba-glutamate connection in schizophrenia: which is the proximate cause?, *Biochem Pharmacol*, *68*(8), 1507–1514, doi:10.1016/j.bcp.2004.07.034.

Coyle, J. T. (2006), Glutamate and schizophrenia: beyond the dopamine hypothesis., *Cell Mol Neurobiol*, *26*(4-6), 365–384, doi:10.1007/s10571-006-9062-8.

D'Adamo, A. F., and F. M. Yatsu (1966), Acetate metabolism in the nervous system. n-acetyl-l-aspartic acid and the biosynthesis of brain lipids., *J Neurochem*, *13*, 961Ü965.

D'Adamo, A. F., L. I. Gidez, and F. M. Yatsu (1968), Acetyl transport mechanisms. involvement of n-acetyl aspartic acid in de novo fatty acid biosynthesis in the developing rat brain., *Exp. Brain.*

Res., *5*, 267–273.

Dawe, G. S., E. H. Hwang, and C. H. Tan (2009), Pathophysiology and animal models of schizophrenia., *Ann Acad Med Singapore*, *38*(5), 425–426.

Deicken, R. F., M. Pegues, and D. Amend (1999), Reduced hippocampal n-acetylaspartate without volume loss in schizophrenia, *Schizophrenia Research*, *37*(3), 217 – 223, doi:DOI: 10.1016/S0920-9964(98)00173-X.

Doege, K., A. T. Bates, T. P. White, D. Das, M. P. Boks, and P. F. Liddle (2009), Reduced event-related low frequency eeg activity in schizophrenia during an auditory oddball task., *Psychophysiology*, *46*(3), 566–577, doi:10.1111/j.1469-8986.2009.00785.x.

Edden, R. A. E., M. Schär, A. E. Hillis, and P. B. Barker (2006), Optimized detection of lactate at high fields using inner volume saturation., *Magn Reson Med*, *56*(4), 912–917, doi:10.1002/mrm.21030.

Edden, R. A. E., M. G. Pomper, and P. B. Barker (2007), In vivo differentiation of n-acetyl aspartyl glutamate from n-acetyl aspartate at 3 tesla., *Magn Reson Med*, *57*(6), 977–982, doi:10.1002/mrm.21234.

Edden, R. A. E., S. D. Muthukumaraswamy, T. C. A. Freeman, and K. D. Singh (2009), Orientation discrimination performance is predicted by gaba concentration and gamma oscillation frequency in human primary visual cortex., *J Neurosci*, *29*(50), 15,721–15,726, doi:10.1523/JNEUROSCI.4426-09.2009.

Evans, C. J., D. J. McGonigle, and R. A. E. Edden (2010), Diurnal stability of gamma-aminobutyric acid concentration in visual and sensorimotor cortex., *J Magn Reson Imaging*, *31*(1), 204–209, doi: 10.1002/jmri.21996.

Farber, N. B., S. H. Kim, K. Dikranian, X. P. Jiang, and C. Heinkel (2002), Receptor mechanisms and circuitry underlying nmda antagonist neurotoxicity., *Mol Psychiatry*, *7*(1), 32–43, doi:10.1038/sj/mp/4000912.

Floyer-Lea, A., M. Wylezinska, T. Kincses, and P. M. Matthews (2006), Rapid modulation of gaba concentration in human sensorimotor cortex during motor learning., *J Neurophysiol, 95*(3), 1639–1644, doi:10.1152/jn.00346.2005.

Fone, K. C. F., and M. V. Porkess (2008), Behavioural and neurochemical effects of post-weaning social isolation in rodents-relevance to developmental neuropsychiatric disorders., *Neurosci Biobehav Rev, 32*(6), 1087–1102, doi:10.1016/j.neubiorev.2008.03.003.

Gallinat, J., C. Mulert, M. Bajbouj, W. M. Herrmann, J. Schunter, D. Senkowski, R. Moukhtieva, D. Kronfeldt, and G. Winterer (2002), Frontal and temporal dysfunction of auditory stimulus processing in schizophrenia., *Neuroimage, 17*(1), 110–127.

Gallinat, J., D. Kunz, D. Senkowski, T. Kienast, F. Seifert, F. Schubert, and A. Heinz (2006), Hippocampal glutamate concentration predicts cerebral theta oscillations during cognitive processing., *Psychopharmacology (Berl), 187*(1), 103–111, doi:10.1007/s00213-006-0397-0.

Gambarota, G., M. van der Graaf, D. Klomp, R. Mulkern, and A. Heerschap (2005), Echo-time independent signal modulations using press sequences: A new approach to spectral editing of strongly coupled ab spin systems, *Journal of Magnetic Resonance, 177*(2), 299 – 306, doi:DOI: 10.1016/j.jmr.2005.08.006.

Gevins, A., M. E. Smith, L. McEvoy, and D. Yu (1997), High-resolution eeg mapping of cortical activation related to working memory: effects of task difficulty, type of processing, and practice., *Cereb Cortex, 7*(4), 374–385.

Geyer, M. A., L. S. Wilkinson, T. Humby, and T. W. Robbins (1993), Isolation rearing of rats produces a deficit in prepulse inhibition of acoustic startle similar to that in schizophrenia., *Biol Psychiatry, 34*(6), 361–372.

Gluck, M. R., R. G. Thomas, K. L. Davis, and V. Haroutunian (2002), Implications for altered glutamate and gaba metabolism in the dorsolateral prefrontal cortex of aged schizophrenic patients, *Am J Psychiatry, 159*(7), 1165–1173, doi:10.1176/appi.ajp.159.7.1165.

Govindaraju, V., K. Young, and A. A. Maudsley (2000), Proton nmr chemical shifts and coupling constants for brain metabolites., *NMR Biomed*, *13*(3), 129–153.

Gozzi, A., A. Schwarz, V. Crestan, and A. Bifone (2008), Drug-anaesthetic interaction in phmri: the case of the psychotomimetic agent phencyclidine., *Magn Reson Imaging*, *26*(7), 999–1006, doi:10.1016/j.mri.2008.01.012.

Graaf, R. A. D., and D. L. Rothman (2001), In Vivo Detection and Quantification of Scalar Coupled 1H NMR Resonances, *Concepts in Magnetic Resonance*, *13(1)*, 32–76.

Gundel, A., and G. F. Wilson (1992), Topographical changes in the ongoing eeg related to the difficulty of mental tasks., *Brain Topogr*, *5*(1), 17–25.

Haase, A., J. Frahm, W. Hänicke, and D. Matthaei (1985), 1h nmr chemical shift selective (chess) imaging., *Phys Med Biol*, *30*(4), 341–344.

Hahn EL (1950), Spin echos, *Physics Review*, *80*, 580–594.

Hetherington, H. P., B. R. Newcomer, and J. W. Pan (1998), Measurements of human cerebral gaba at 4.1 t using numerically optimized editing pulses., *Magn Reson Med*, *39*(1), 6–10.

Hofmann, L., J. Slotboom, B. Jung, P. Maloca, C. Boesch, and R. Kreis (2002), Quantitative 1h-magnetic resonance spectroscopy of human brain: Influence of composition and parameterization of the basis set in linear combination model-fitting., *Magn Reson Med*, *48*(3), 440–453, doi:10.1002/mrm.10246.

Holcomb, H. H., A. C. Lahti, D. R. Medoff, M. Weiler, and C. A. Tamminga (2001), Sequential regional cerebral blood flow brain scans using pet with h2(15)o demonstrate ketamine actions in cns dynamically., *Neuropsychopharmacology*, *25*(2), 165–172, doi:10.1016/S0893-133X(01)00229-9.

Homayoun, H., and B. Moghaddam (2007), Nmda receptor hypofunction produces opposite effects on prefrontal cortex interneurons and pyramidal neurons., *J Neurosci*, *27*(43), 11,496–11,500, doi:10.1523/JNEUROSCI.2213-07.2007.

Horacek, J., C. Dockery, M. Kopecek, F. Spaniel, T. Novak, B. Tislerova, M. Klirova, T. Palenicek, and

C. Höschl (2006), Regional brain metabolism as the predictor of performance on the trail making test in schizophrenia. a 18fdg pet covariation study., *Neuro Endocrinol Lett*, *27*(5), 587–594.

Iltis, I., D. M. Koski, L. E. Eberly, C. D. Nelson, D. K. Deelchand, J. Valette, K. Ugurbil, K. O. Lim, and P.-G. Henry (2009), Neurochemical changes in the rat prefrontal cortex following acute phencyclidine treatment: an in vivo localized (1)h mrs study., *NMR Biomed*, *22*(7), 737–744, doi:10.1002/nbm.1385.

ISMRM abstract: 4283 (2009), Press spectroscopy of glutamate: Effects of voxel location and field strength, in *17th Scientific Meeting and Exibition of ISMRM*.

Javitt, D. C., and S. R. Zukin (1991), Recent advances in the phencyclidine model of schizophrenia., *Am J Psychiatry*, *148*(10), 1301–1308.

Kanamori, K., B. D. Ross, and R. W. Kondrat (2002), Glial uptake of neurotransmitter glutamate from the extracellular fluid studied in vivo by microdialysis and (13)c nmr., *J Neurochem*, *83*(3), 682–695.

Kauppinen, R. A., T. R. Pirttilä, S. O. Auriola, and S. R. Williams (1994), Compartmentation of cerebral glutamate in situ as detected by 1h/13c n.m.r., *Biochem J*, *298 (Pt 1)*, 121–127.

Ke, Y., B. M. Cohen, J. Y. Bang, M. Yang, and P. F. Renshaw (2000), Assessment of gaba concentration in human brain using two-dimensional proton magnetic resonance spectroscopy., *Psychiatry Res*, *100*(3), 169–178.

Kedzior, K. K., and M. T. Martin-Iverson (2007), Attention-dependent reduction in prepulse inhibition of the startle reflex in cannabis users and schizophrenia patients–a pilot study., *Eur J Pharmacol*, *560*(2-3), 176–182, doi:10.1016/j.ejphar.2007.01.032.

Keltner, J. R., L. L. Wald, J. D. Christensen, L. C. Maas, C. M. Moore, B. M. Cohen, and P. F. Renshaw (1996), A technique for detecting gaba in the human brain with press localization and optimized refocusing spectral editing radiofrequency pulses., *Magn Reson Med*, *36*(3), 458–461.

Keltner, J. R., L. L. Wald, B. D. Frederick, and P. F. Renshaw (1997), In vivo detection of gaba in human brain using a localized double-quantum filter technique., *Magn Reson Med*, *37*(3), 366–371.

Klose U (1990), In vivo proton spectroscopy in presence of eddy currents, *Magn. Reson. Med.*, *14*, 26–30.

Klunk, W. E., C. Xu, K. Panchalingam, R. J. McClure, and J. W. Pettegrew (1996), Quantitative 1h and 31p mrs of pca extracts of postmortem alzheimer's disease brain., *Neurobiol. Aging*, *17*, 349–57.

Kreis, R., M. Koster, M. Kamber, H. Hoppeler, and C. Boesch (1997), Peak assignment in localized 1h mr spectra of human muscle based on oral creatine supplementation., *Magn Reson Med*, *37*, 159–163.

Krystal, J. H., L. P. Karper, J. P. Seibyl, G. K. Freeman, R. Delaney, J. D. Bremner, G. R. Heninger, M. B. Bowers, and D. S. Charney (1994), Subanesthetic effects of the noncompetitive nmda antagonist, ketamine, in humans. psychotomimetic, perceptual, cognitive, and neuroendocrine responses., *Arch Gen Psychiatry*, *51*(3), 199–214.

Lahti, A. C., H. H. Holcomb, D. R. Medoff, and C. A. Tamminga (1995a), Ketamine activates psychosis and alters limbic blood flow in schizophrenia., *Neuroreport*, *6*(6), 869–872.

Lahti, A. C., B. Koffel, D. LaPorte, and C. A. Tamminga (1995b), Subanesthetic doses of ketamine stimulate psychosis in schizophrenia., *Neuropsychopharmacology*, *13*(1), 9–19, doi:10.1016/0893-133X(94)00131-I.

Lawson, C. L., and R. J. Hanson (1995), *Solving Least Squares Problems*, SIAM.

Levitt, M. H. (2001), *Spin dynamics: basics of nuclear magnetic resonance.*

Lewis, D. A., and B. Moghaddam (2006), Cognitive dysfunction in schizophrenia: convergence of gamma-aminobutyric acid and glutamate alterations., *Arch Neurol*, *63*(10), 1372–1376, doi:10.1001/archneur.63.10.1372.

Licata, S. C., J. E. Jensen, D. M. Penetar, A. P. Prescot, S. E. Lukas, and P. F. Renshaw (2009), A therapeutic dose of zolpidem reduces thalamic gaba in healthy volunteers: a proton mrs study at 4 t., *Psychopharmacology (Berl)*, *203*(4), 819–829, doi:10.1007/s00213-008-1431-1.

Liddle, P. F., E. T. Ngan, G. Duffield, K. Kho, and A. J. Warren (2002), Signs and Symptoms of Psychotic Illness (SSPI): a rating scale, *The British Journal of Psychiatry*, *180*(1), 45–50.

Littlewood, C. L., D. Cash, A. L. Dixon, S. L. Dix, C. T. White, M. J. O'Neill, M. Tricklebank, and S. C. R. Williams (2006a), Using the bold mr signal to differentiate the stereoisomers of ketamine in the rat., *Neuroimage*, *32*(4), 1733–1746, doi:10.1016/j.neuroimage.2006.05.022.

Littlewood, C. L., N. Jones, M. J. O'Neill, S. N. Mitchell, M. Tricklebank, and S. C. R. Williams (2006b), Mapping the central effects of ketamine in the rat using pharmacological mri., *Psychopharmacology (Berl)*, *186*(1), 64–81, doi:10.1007/s00213-006-0344-0.

Lorrain, D. S., C. S. Baccei, L. J. Bristow, J. J. Anderson, and M. A. Varney (2003), Effects of ketamine and n-methyl-d-aspartate on glutamate and dopamine release in the rat prefrontal cortex: modulation by a group ii selective metabotropic glutamate receptor agonist ly379268., *Neuroscience*, *117*(3), 697–706.

Ludewig, K., M. A. Geyer, and F. X. Vollenweider (2003), Deficits in prepulse inhibition and habituation in never-medicated, first-episode schizophrenia., *Biol Psychiatry*, *54*(2), 121–128.

Lutkenhoff, E. S., et al. (2010), Proton mrs in twin pairs discordant for schizophrenia., *Mol Psychiatry*, *15*(3), 308–318, doi:10.1038/mp.2008.87.

Macura S, E. R. (1980), Elucidation of cross relaxation in liquids by two-dimensional nmr spectroscopy., *Mol. Phys.*, *41*, 95–117.

Maxwell, C. R., R. S. Ehrlichman, Y. Liang, D. Trief, S. J. Kanes, J. Karp, and S. J. Siegel (2006), Ketamine produces lasting disruptions in encoding of sensory stimuli., *J Pharmacol Exp Ther*, *316*(1), 315–324, doi:10.1124/jpet.105.091199.

McLean, M. A., F. G. Woermann, G. J. Barker, and J. S. Duncan (2000), Quantitative analysis of short echo time [1]h-mrsi of cerebral gray and white matter, *Magnetic Resonance in Medicine*, *44*, 401–411.

Melendez, R. I., M. L. Gregory, M. T. Bardo, and P. W. Kalivas (2004), Impoverished rearing environment alters metabotropic glutamate receptor expression and function in the prefrontal cortex., *Neuropsychopharmacology*, *29*(11), 1980–1987, doi:10.1038/sj.npp.1300507.

Mescher, M., H. Merkle, J. Kirsch, M. Garwood, and R. Gruetter (1998), Simultaneous in vivo spectral editing and water suppression., *NMR Biomed, 11*(6), 266–272.

Michaelis, T., G. Helms, K. D. Merboldt, W. Hänicke, H. Bruhn, and J. Frahm (1993a), Identification of scyllo-inositol in proton nmr spectra of human brain in vivo., *NMR Biomed., 6*, 105–109.

Michaelis, T., K. D. Merboldt, H. Bruhn, W. Hänicke, and J. Frahm (1993b), Absolute concentrations of metabolites in the adult human brain in vivo: quantification of localized proton mr spectra, *Radiology, 187*, 219–227.

Mlynárik, V., S. Gruber, and E. Moser (2001), Proton t (1) and t (2) relaxation times of human brain metabolites at 3 tesla., *NMR Biomed, 14*(5), 325–331.

Moghaddam, B., and B. W. Adams (1998), Reversal of phencyclidine effects by a group ii metabotropic glutamate receptor agonist in rats., *Science, 281*(5381), 1349–1352.

Moghaddam, B., B. Adams, A. Verma, and D. Daly (1997), Activation of glutamatergic neurotransmission by ketamine: a novel step in the pathway from nmda receptor blockade to dopaminergic and cognitive disruptions associated with the prefrontal cortex., *J Neurosci, 17*(8), 2921–2927.

Mullins, P. G., H. Chen, J. Xu, A. Caprihan, and C. Gasparovic (2008), Comparative reliability of proton spectroscopy techniques designed to improve detection of j-coupled metabolites, *Magnetic Resonance in Medicine, 60*, 964–969.

Murck, H., M. Fava, J. Alpert, A. A. Nierenberg, D. Mischoulon, M. W. Otto, J. Zajecka, M. Mannel, and J. F. Rosenbaum (2005), Hypericum extract in patients with mdd and reversed vegetative signs: re-analysis from data of a double-blind, randomized trial of hypericum extract, fluoxetine, and placebo., *Int J Neuropsychopharmacol, 8*(2), 215–221, doi:10.1017/S1461145704004717.

Muthukumaraswamy, S. D., R. A. E. Edden, D. K. Jones, J. B. Swettenham, and K. D. Singh (2009), Resting gaba concentration predicts peak gamma frequency and fmri amplitude in response to visual stimulation in humans., *Proc Natl Acad Sci U S A, 106*(20), 8356–8361, doi:10.1073/pnas.0900728106.

Naressi, A., C. Couturier, J. M. Devos, M. Janssen, C. Mangeat, R. de Beer, and D. Graveron-Demilly (2001), Java-based graphical user interface for the mrui quantitation package., *MAGMA*, *12*(2-3), 141–152.

O'Donnell, B. F., S. F. Faux, R. W. McCarley, M. O. Kimble, D. F. Salisbury, P. G. Nestor, R. Kikinis, F. A. Jolesz, and M. E. Shenton (1995a), Increased rate of p300 latency prolongation with age in schizophrenia. electrophysiological evidence for a neurodegenerative process., *Arch Gen Psychiatry*, *52*(7), 544–549.

O'Donnell, B. F., M. E. Shenton, R. W. McCarley, S. F. Faux, R. Kikinis, P. G. Nestor, and F. A. Jolesz (1995b), Conjoint left asymmetry of auditory p300 voltage and mri volume of posterior superior temporal gyrus in schizophrenia: a quantitative evaluation., *Electroencephalogr Clin Neurophysiol Suppl*, *44*, 387–394.

O'Donnell, B. F., J. L. Vohs, W. P. Hetrick, C. A. Carroll, and A. Shekhar (2004), Auditory event-related potential abnormalities in bipolar disorder and schizophrenia., *Int J Psychophysiol*, *53*(1), 45–55, doi:10.1016/j.ijpsycho.2004.02.001.

Ogg, R. J., R. B. Kingsley, and J. S. Taylor (1994), Wet, a t1- and b1-insensitive water-suppression method for in vivo localized 1h nmr spectroscopy, *Journal of Magnetic Resonance, Series B*, *104*(1), 1 – 10, doi:DOI: 10.1006/jmrb.1994.1048.

Olbrich, H. M., G. Valerius, N. Rüsch, M. Buchert, T. Thiel, J. Hennig, D. Ebert, and L. T. V. Elst (2008), Frontolimbic glutamate alterations in first episode schizophrenia: evidence from a magnetic resonance spectroscopy study., *World J Biol Psychiatry*, *9*(1), 59–63, doi:10.1080/15622970701227811.

Olney, J. W., and N. B. Farber (1995), Glutamate receptor dysfunction and schizophrenia., *Arch Gen Psychiatry*, *52*(12), 998–1007.

Olney, J. W., J. W. Newcomer, and N. B. Farber (1999), Nmda receptor hypofunction model of schizophrenia., *J Psychiatr Res*, *33*(6), 523–533.

Oostenveld, R., and P. Praamstra (2001), The five percent electrode system for high-resolution eeg and

erp measurements., *Clin Neurophysiol, 112*(4), 713–719.

Opitz, B., T. Rinne, A. Mecklinger, D. Y. von Cramon, and E. Schröger (2002), Differential contribution of frontal and temporal cortices to auditory change detection: fmri and erp results., *Neuroimage, 15*(1), 167–174, doi:10.1006/nimg.2001.0970.

Pfund, Z., D. C. Chugani, C. Juhász, O. Muzik, H. T. Chugani, I. B. Wilds, N. Seraji-Bozorgzad, and G. J. Moore (2000), Evidence for coupling between glucose metabolism and glutamate cycling using fdg pet and 1h magnetic resonance spectroscopy in patients with epilepsy., *J Cereb Blood Flow Metab, 20*(5), 871–878, doi:10.1097/00004647-200005000-00014.

Pfurtscheller, G., and F. H. L. da Silva (1999), Event-related eeg/meg synchronization and desynchronization: basic principles., *Clin Neurophysiol, 110*(11), 1842–1857.

Pirttilä, T. R., J. M. Hakumäki, and R. A. Kauppinen (1993), 1h nuclear magnetic resonance spectroscopy study of cerebral glutamate in an ex vivo brain preparation of guinea pig., *J Neurochem, 60*(4), 1274–1282.

Pizzagalli, D., T. Oakes, and R. Davidson (2003), Coupling of theta activity and glucose metabolism in the human rostral anterior cingulate cortex: An eegpet study of normal and depressed subjects, *Psychophysiology, 40*, 939–949(11).

Potts, G. F., Y. Hirayasu, B. F. O'Donnell, M. E. Shenton, and R. W. McCarley (1998), High-density recording and topographic analysis of the auditory oddball event-related potential in patients with schizophrenia., *Biol Psychiatry, 44*(10), 982–989.

Prabakaran, S., et al. (2004), Mitochondrial dysfunction in schizophrenia: evidence for compromised brain metabolism and oxidative stress., *Mol Psychiatry, 9*(7), 684–97, 643, doi:10.1038/sj.mp.4001511.

Provencher, S. W. (1993), Estimation of metabolite concentrations from localized in vivo proton nmr spectra., *Magn Reson Med, 30*(6), 672–679.

Provencher, S. W. (2001), Automatic quantitation of localized in vivo 1h spectra with lcmodel., *NMR*

Biomed, 14(4), 260–264.

Purdon, S. E., A. Valiakalayil, C. C. Hanstock, P. Seres, and P. Tibbo (2008), Elevated 3t proton mrs glutamate levels associated with poor continuous performance test (cpt-0x) scores and genetic risk for schizophrenia., *Schizophr Res, 99*(1-3), 218–224, doi:10.1016/j.schres.2007.11.028.

R. A. De Graaf (2007), *In Vivo NMR Spectroscopy. Principles and Techniques.*, John Wiley & Sons Ltd.

Raghavachari, S., J. E. Lisman, M. Tully, J. R. Madsen, E. B. Bromfield, and M. J. Kahana (2006), Theta oscillations in human cortex during a working-memory task: evidence for local generators., *J Neurophysiol, 95*(3), 1630–1638, doi:10.1152/jn.00409.2005.

Ratiney, H., Y. Coenradie, S. Cavassila, D. van Ormondt, and D. Graveron-Demilly (2004), Time-domain quantitation of 1h short echo-time signals: background accommodation., *MAGMA, 16*(6), 284–296, doi:10.1007/s10334-004-0037-9.

Ratiney, H., M. Sdika, Y. Coenradie, S. Cavassila, D. van Ormondt, and D. Graveron-Demilly (2005), Time-domain semi-parametric estimation based on a metabolite basis set., *NMR Biomed, 18*(1), 1–13, doi:10.1002/nbm.895.

Rothman, D. L., O. A. Petroff, K. L. Behar, and R. H. Mattson (1993), Localized 1h nmr measurements of gamma-aminobutyric acid in human brain in vivo., *Proc Natl Acad Sci U S A, 90*(12), 5662–5666.

Rothman, D. L., K. L. Behar, F. Hyder, and R. G. Shulman (2003), In vivo nmr studies of the glutamate neurotransmitter flux and neuroenergetics: implications for brain function., *Annu Rev Physiol, 65*, 401–427, doi:10.1146/annurev.physiol.65.092101.142131.

Rowland, L. M., R. S. Astur, R. E. Jung, J. R. Bustillo, J. Lauriello, and R. A. Yeo (2005a), Selective cognitive impairments associated with nmda receptor blockade in humans., *Neuropsychopharmacology, 30*(3), 633–639, doi:10.1038/sj.npp.1300642.

Rowland, L. M., et al. (2005b), Effects of ketamine on anterior cingulate glutamate metabolism in healthy humans: a 4-t proton mrs study., *Am J Psychiatry, 162*(2), 394–396, doi:10.1176/appi.ajp.162.2.394.

Rüsch, N., L. T. van Elst, G. Valerius, M. Büchert, T. Thiel, D. Ebert, J. Hennig, and H.-M. Olbrich (2008), Neurochemical and structural correlates of executive dysfunction in schizophrenia., *Schizophr Res*, *99*(1-3), 155–163, doi:10.1016/j.schres.2007.05.024.

Rudkin, T. M., and D. L. Arnold (1999), Proton magnetic resonance spectroscopy for the diagnosis and management of cerebral disorders, *Arch. Neurol.*, *56*, 919–926.

Schmiedt, C., A. Brand, H. Hildebrandt, and C. Basar-Eroglu (2005), Event-related theta oscillations during working memory tasks in patients with schizophrenia and healthy controls., *Brain Res Cogn Brain Res*, *25*(3), 936–947, doi:10.1016/j.cogbrainres.2005.09.015.

Schubert, M., R. E. Edge, P. Lario, M. A. Cook, N. C. J. Strynadka, G. A. Mackie, and L. P. McIntosh (2004), Structural characterization of the rnase e s1 domain and identification of its oligonucleotide-binding and dimerization interfaces., *J Mol Biol*, *341*(1), 37–54, doi:10.1016/j.jmb.2004.05.061.

Schubert, M. I., M. V. Porkess, N. Dashdorj, K. C. F. Fone, and D. P. Auer (2009), Effects of social isolation rearing on the limbic brain: a combined behavioral and magnetic resonance imaging volumetry study in rats., *Neuroscience*, *159*(1), 21–30, doi:10.1016/j.neuroscience.2008.12.019.

Schulte, R. F., and P. Boesiger (2006a), Profit: two-dimensional prior-knowledge fitting of j-resolved spectra., *NMR Biomed*, *19*(2), 255–263, doi:10.1002/nbm.1026.

Schulte, R. F., and P. Boesiger (2006b), Profit: two-dimensional prior-knowledge fitting of j-resolved spectra., *NMR Biomed*, *19*(2), 255–263, doi:10.1002/nbm.1026.

Sederberg, P. B., M. J. Kahana, M. W. Howard, E. J. Donner, and J. R. Madsen (2003), Theta and gamma oscillations during encoding predict subsequent recall., *J Neurosci*, *23*(34), 10,809–10,814.

Shen, J., D. C. Shungu, and D. L. Rothman (1999), In vivo chemical shift imaging of gamma-aminobutyric acid in the human brain., *Magn Reson Med*, *41*(1), 35–42.

Shen, J., D. L. Rothman, and P. Brown (2002), In vivo gaba editing using a novel doubly selective multiple quantum filter., *Magn Reson Med*, *47*(3), 447–454.

Shirayama, Y., T. Obata, D. Matsuzawa, H. Nonaka, Y. Kanazawa, E. Yoshitome, H. Ikehira, K. Hashimoto, and M. Iyo (2010), Specific metabolites in the medial prefrontal cortex are associated with the neurocognitive deficits in schizophrenia: a preliminary study., *Neuroimage*, *49*(3), 2783–2790, doi:10.1016/j.neuroimage.2009.10.031.

Siegel, G. J. (1989), *Basic neurochemistry: molecular, cellular, and medical apects,*, Raven Press, New York.

Slotboom, J., C. Boesch, and R. Kreis (1998), Versatile frequency domain fitting using time domain models and prior knowledge., *Magn Reson Med*, *39*(6), 899–911.

Snyder J, W. A., Thompson RB (2009), Ismrm abstract 2394: Optimized detection of glutamate and glutamine at 1.5 t 3.t and 4.7 t, in *17th Scientific Meeting and Exibition of ISMRM*.

Sobol I. M. (1967), Distribution of points in a cube and approximate evaluation of integrals, *U.S.S.R Comput. Maths. Math. Phys.*, *7*, 86–112.

Soher, B. J., and A. A. Maudsley (2004), Evaluation of variable line-shape models and prior information in automated 1h spectroscopic imaging analysis., *Magn Reson Med*, *52*(6), 1246–1254, doi:10.1002/mrm.20295.

Sörös, P., N. Michael, M. Tollkötter, and B. Pfleiderer (2006), The neurochemical basis of human cortical auditory processing: combining proton magnetic resonance spectroscopy and magnetoencephalography., *BMC Biol*, *4*, 25, doi:10.1186/1741-7007-4-25.

Tayoshi, S., et al. (2009), Metabolite changes and gender differences in schizophrenia using 3-tesla proton magnetic resonance spectroscopy (1h-mrs)., *Schizophr Res*, *108*(1-3), 69–77, doi:10.1016/j.schres.2008.11.014.

Théberge, J., Y. Al-Semaan, P. C. Williamson, R. S. Menon, R. W. J. Neufeld, N. Rajakumar, B. Schaefer, M. Densmore, and D. J. Drost (2003), Glutamate and glutamine in the anterior cingulate and thalamus of medicated patients with chronic schizophrenia and healthy comparison subjects measured with 4.0-t proton mrs., *Am J Psychiatry*, *160*(12), 2231–2233.

Théberge, J., et al. (2002), Glutamate and glutamine measured with 4.0 t proton mrs in never-treated patients with schizophrenia and healthy volunteers., *Am J Psychiatry*, *159*(11), 1944–1946.

Théberge, J., et al. (2007), Longitudinal grey-matter and glutamatergic losses in first-episode schizophrenia., *Br J Psychiatry*, *191*, 325–334, doi:10.1192/bjp.bp.106.033670.

Tibbo, P., C. Hanstock, A. Valiakalayil, and P. Allen (2004), 3-t proton mrs investigation of glutamate and glutamine in adolescents at high genetic risk for schizophrenia., *Am J Psychiatry*, *161*(6), 1116–1118.

Tkác, I., Z. Starcuk, I. Y. Choi, and R. Gruetter (1999), In vivo 1h nmr spectroscopy of rat brain at 1 ms echo time., *Magn Reson Med*, *41*(4), 649–656.

Tkác, I., G. Oz, G. Adriany, K. U?urbil, and R. Gruetter (2009), In vivo 1h nmr spectroscopy of the human brain at high magnetic fields: metabolite quantification at 4t vs. 7t., *Magn Reson Med*, *62*(4), 868–879, doi:10.1002/mrm.22086.

Träber, F., W. Block, R. Lamerichs, J. Gieseke, and H. H. Schild (2004), 1h metabolite relaxation times at 3.0 tesla: Measurements of t1 and t2 values in normal brain and determination of regional differences in transverse relaxation., *J Magn Reson Imaging*, *19*(5), 537–545, doi:10.1002/jmri.20053.

Tsujimoto, T., H. Shimazu, and Y. Isomura (2006), Direct recording of theta oscillations in primate prefrontal and anterior cingulate cortices., *J Neurophysiol*, *95*(5), 2987–3000, doi:10.1152/jn.00730.2005.

Umbricht, D., L. Schmid, R. Koller, F. X. Vollenweider, D. Hell, and D. C. Javitt (2000), Ketamine-induced deficits in auditory and visual context-dependent processing in healthy volunteers: implications for models of cognitive deficits in schizophrenia., *Arch Gen Psychiatry*, *57*(12), 1139–1147.

Urenjak, J., S. R. Williams, D. G. Gadian, and M. Noble (1992), Specific expression of n-acetylaspartate in neurons, oligodedrocyte-type-2 astrocyte progenitors, and immature oligodedrocyte *in vitro*, *J Neurochem*, *59*, 55–61.

van der Stelt, O., J. Frye, J. A. Lieberman, and A. Belger (2004), Impaired p3 generation reflects high-level and progressive neurocognitive dysfunction in schizophrenia., *Arch Gen Psychiatry*, *61*(3), 237–248, doi:10.1001/archpsyc.61.3.237.

van Elst, L. T., G. Valerius, M. Büchert, T. Thiel, N. Rüsch, E. Bubl, J. Hennig, D. Ebert, and H. M. Olbrich (2005a), Increased prefrontal and hippocampal glutamate concentration in schizophrenia: evidence from a magnetic resonance spectroscopy study., *Biol Psychiatry*, *58*(9), 724–730, doi:10.1016/j.biopsych.2005.04.041.

van Elst, L. T., G. Valerius, M. Büchert, T. Thiel, N. Rüsch, E. Bubl, J. Hennig, D. Ebert, and H. M. Olbrich (2005b), Increased prefrontal and hippocampal glutamate concentration in schizophrenia: Evidence from a magnetic resonance spectroscopy study, *Biological Psychiatry*, *58*(9), 724 – 730, doi:DOI: 10.1016/j.biopsych.2005.04.041.

Vanhamme, van den Boogaart A, and V. H. S (1997), Improved method for accurate and efficient quantification of mrs data with use of prior knowledge, *J Magn Reson*, *129*(1), 35–43.

Verbruggen, F., and G. D. Logan (2008), Automatic and controlled response inhibition: associative learning in the go/no-go and stop-signal paradigms., *J Exp Psychol Gen*, *137*(4), 649–672, doi:10.1037/a0013170.

Veshtort, M., and R. G. Griffin (2006), Spinevolution: a powerful tool for the simulation of solid and liquid state nmr experiments., *J Magn Reson*, *178*(2), 248–282, doi:10.1016/j.jmr.2005.07.018.

Vollenweider, F. X., K. L. Leenders, C. Scharfetter, A. Antonini, P. Maguire, J. Missimer, and J. Angst (1997), Metabolic hyperfrontality and psychopathology in the ketamine model of psychosis using positron emission tomography (pet) and [18f]fluorodeoxyglucose (fdg)., *Eur Neuropsychopharmacol*, *7*(1), 9–24.

Wilson, M., G. Reynolds, R. A. Kauppinen, T. N. Arvanitis, and A. C. Peet (2010), A constrained least-squares approach to the automated quantitation of in vivo (1)h magnetic resonance spectroscopy data., *Magn Reson Med*, doi:10.1002/mrm.22579.

Wong, C. G. T., T. Bottiglieri, and O. C. Snead (2003), Gaba, gamma-hydroxybutyric acid, and neurological disease, *Annals of Neurology*, *54*, S3–S12.

Wood, S. J., M. Yücel, R. M. Wellard, B. J. Harrison, K. Clarke, A. Fornito, D. Velakoulis, and C. Pantelis (2007), Evidence for neuronal dysfunction in the anterior cingulate of patients with schizophrenia: a proton magnetic resonance spectroscopy study at 3 t., *Schizophr Res*, *94* (1-3), 328–331, doi:10.1016/j.schres.2007.05.008.

Yablonskiy, D. A., J. J. Neil, M. E. Raichle, and J. J. Ackerman (1998), Homonuclear j coupling effects in volume localized nmr spectroscopy: pitfalls and solutions., *Magn Reson Med*, *39* (2), 169–178.

Yang, S., J. Hu, Z. Kou, and Y. Yang (2008), Spectral simplification for resolved glutamate and glutamine measurement using a standard steam sequence with optimized timing parameters at 3, 4, 4.7, 7, and 9.4t., *Magn. Reson. Med.*, *59* (2), 236–244, doi:10.1002/mrm.21463.

Zelenaia, O., B. D. Schlag, G. E. Gochenauer, R. Ganel, W. Song, J. S. Beesley, J. B. Grinspan, J. D. Rothstein, and M. B. Robinson (2000), Epidermal Growth Factor Receptor Agonists Increase Expression of Glutamate Transporter GLT-1 in Astrocytes through Pathways Dependent on Phosphatidylinositol 3-Kinase and Transcription Factor NF-ÎžB, *Molecular Pharmacology*, *57* (4), 667–678.

Zijl, P. C. V., and P. B. Barker (1997), Magnetic resonance spectroscopy and spectroscopic imaging for the study of brain metabolism, *Ann N Y Acad Sci*, *820*, 75–96.